# Design of a Composite Combat Helmet Liner for Prevention of Blast-Induced Traumatic Brain Injury

by

Andrew Vechart

B.S., Mechanical Engineering and Physics
University of Wisconsin - Milwaukee, 2009

Submitted to the School of Engineering
in Partial Fulfillment of the Requirements for the Degree of
Master of Science in Computation for Design and Optimization

at

Massachusetts Institute of Technology
February 2011



Author .....

Computation for Design and Optimization Program
January 14, 2011

Certified by.....

Laurence R. Young
Apollo Professor of Astronautics
Professor of Health Sciences and Technology
Thesis Supervisor

Accepted by.....

Nicolas Hadjiconstantinou
Associate Professor of Mechanical Engineering
Director, Computation for Design and Optimization Program

# Design of a Composite Combat Helmet Liner for Prevention of Blast-Inducted Traumatic Brain Injury

by

Andrew Vechart

Submitted to the School of Engineering
in Partial Fulfillment of the Requirements for the Degree of
Master of Science in Computation for Design and Optimization

## Abstract

Air blast-induced traumatic brain injuries (TBIs) represent a significant percentage of military personnel injuries observed in Operation Enduring Freedom (OEF) and Operation Iraqi Freedom (OIF). Prevalence of blast-induced TBIs is attributed to several factors, including improved body armor, improved diagnostic techniques, greater awareness, and the increased threat of attack by improvised explosive devices (IEDs). Though the mechanisms of blast-induced TBIs are not fully understood, this is a serious problem that needs to be addressed.

The overall goal of the work presented in this report is to explore a possible improvement to the Advanced Combat Helmet (ACH) liner increasing the protection against blast-induced TBIs. The essential new element is the inclusion of moveable or deformable materials sandwiched within foam to dissipate the blast energy, reduce the peak transmitted pressure, and stretch the blast waveform before it reaches the brain. Filler materials explored in this work include glass beads, aerogel, glycerin, and water.

To contribute to this goal, the description and validation of a model of the dynamic response of a (modified) helmet and head surrogate to an air blast event is presented in this report. An initial prototype for a liner incorporating the filler material technology is designed and manufactured. The response characteristics of this prototype are then assessed experimentally by collecting pressure data during air blast loading provided by an explosive drive shock tube. Experimental work is carried out at Purdue University. A nonlinear finite element model is then developed using the commercial code ABAQUS® to describe the response observed experimentally. Consistency between results obtained numerically and results obtained experimentally indicates the model accurately describes the physics of a blast event impinging on a helmet and head. Several suggestions are then provided for how the model may be used to optimize the design of a helmet liner providing the maximum protection against air-blasts.

Thesis Supervisor: Laurence R. Young
Apollo Program Professor of Astronautics
Professor of Health Sciences and Technology

# Acknowledgements

I would like to begin by thanking my advisor Prof. Laurence Young for the chance to work on this project. I truly appreciate not only the guidance he provided but also the freedom and flexibility he allowed to approach the research problem from different perspectives. For providing generous funding for this project, I would like to acknowledge the Office of Naval Research (# N00014-08-1-0261), the Center for Integration of Medicine and Innovative Technology (# W81XWH-07-2-0011), and Deshpande Center at MIT (MIT OSP # 689934).

I would like to thank Prof. Steven Son and his graduate student, Ben Schimizze, at Purdue University for their experimental efforts providing critical data for this project. Thank you to Prof. Raul Radovitzky for lending his expertise to this project. For guidance and discussion about material modeling, I thank Prof. Lorna Gibson in the Department of Materials Science and Engineering at MIT. For her extensive efforts to characterize the high strain rate compression response of foam, Dr. Simona Socrate deserves much recognition and thanks. I would like to extend my gratitude as well to Prof. Andrew Whittle and Dr. Jack Germaine in the Department of Civil and Environmental Engineering at MIT for their advice and assistance in testing and modeling the stress-strain response of glass beads. Finally, for the technical expertise with ABAQUS® he provided in the early stages of this project, I would like to thank Dr. Antoine Jérusalem.

I thank George Christou for his efforts laying the groundwork for the simulations performed for this project. A special thanks goes to my colleague, Rahul Goel, with whom I worked for the majority of the time I was involved with the project. Many 'fruitful' discussions between he and I led to important and effective work towards progress on this project. I thank Laura Koller for her guidance and support, making my experience in the CDO program very enjoyable. I also thank Liz Zotos for all of the support she provided during my time in the MVL. I also want to thank Michal Kracik for his help on some of the images included in this report. Thanks also to all of my colleagues in the MVL. I was glad to be a part of arguably the best lab on campus.

A big thank you goes out to my wife, Katie, for all of her love, support, and understanding throughout my graduate career. Thanks also to all of our family and friends in Wisconsin and Minnesota for their support of our adventure to the East Coast.

Finally, I thank all of the men and women serving in our armed forces to protect the security and freedom of the United States. I hope this technology will one day make their jobs much safer.

# Table of Contents

# List of Figures

# List of Tables

# List of Abbreviations

| | |
|---|---|
| " - | inches |
| ACH - | Advanced Combat Helmet |
| ALE - | Arbitrary Lagrangian - Eulerian |
| ASTM - | American Society for Testing and Materials |
| atm - | atmospheres |
| C3D4 - | Four node linear tetrahedral element |
| C3D8 - | Eight node linear brick element |
| cc - | cubic centimeter |
| CEL - | Coupled Eulerian - Lagrangian |
| cm - | centimeter |
| ConWep - | Conventional Weapons Effects |
| DAI - | Diffuse Axonal Injury |
| DVBIC - | Defense and Veterans Brain Injury Center |
| EEG - | Electroencephalogram |
| EPS - | Expanded Polystyene |
| FEM - | Finite Element Method |
| g - | gram |
| ICP - | Intracranial Pressure |
| IED - | Improvised Explosive Device |
| in - | inches |
| kHz - | kiloHertz |
| kPa - | kiloPascals |
| LCC - | Limiting Compression Curve |
| mm - | millimeter |
| MPa - | megaPascals |
| ms - | milliseconds |
| OEF - | Operation Enduring Freedom |
| OIF - | Operation Iraqi Freedom |
| Pa - | Pascals |
| PASGT - | Personal Armor System Ground Troops' |
| PMMA - | Poly(methyl methacrylate) |
| psig - | Pounds Per Sqaure Inch - Gage |
| SHPB - | Split Hopkinson Pressure Bar |
| TBI - | Traumatic Brain Injury |
| TNT - | Trinitrotoluene |
| V - | Volts |
| VFT - | Volume Fraction Tool |
| wrt - | with respect to |

# Chapter 1 Introduction

The work discussed in this report was performed during the third year of a now four year contract with the Office of Naval Research focusing on improving blast protection for combat troops. This chapter presents some of the motivation for the research along with the objectives and methods employed. A description of the organization of the rest of the report is included as well.

## 1.1 Motivation

Traumatic Brain Injuries (TBIs) resulting from explosions represent a significant percentage of military personnel injuries. According to the Defense and Veterans Brain Injury Center (DVBIC), more than 150,000 U.S. Military personnel have been medically diagnosed with a traumatic brain injury (TBI) since 2001. Severity of TBIs ranges from so-called mild injuries, such as concussions, all the way to head penetration injuries (1). In a study by Wojcik et. al., 46.7% of TBIs in subjects from Operation Enduring Freedom (OEF) in Afghanistan and 63.9% of TBIs in subjects from Operation Iraqi Freedom (OIF) in Iraq were attributable to exposure to explosions (2).

There are several reasons TBIs have become more prevalent in OEF and OIF. In contrast to the pattern in previous conflicts, improved body armor permits personnel to survive TBI-causing experiences that were previously fatal. Furthermore, understanding and recognition of TBIs has improved in the medical community, leading to a higher rate of diagnosis. In addition, increased use of Improvised Explosive Devices (IEDs) has increased the probability of exposure of personnel to TBI-causing explosions (3). Regardless of the reason, blast-induced TBIs are a prominent problem that need to be addressed.

This project addresses the immediate need for improved protection against primary blast-related TBI resulting from the shock wave generated by an explosion. A new combat helmet liner is being developed that adds blast protection to the capabilities of the standard issue helmet, supplementing the current protection afforded against impact type injuries. The essential new element is the inclusion of moveable or deformable materials sandwich within the foam to dissipate the blast energy, reduce the peak transmitted pressure, and lengthen the blast waveform before it reaches the brain. Candidates for filler materials considered in this report are glass beads, aerogel, water, and glycerin. The work for this thesis emphasizes development and validation of a numerical model of the air-blast scenario loading a head surrogate model coupled with a helmet-liner model.

## 1.2 Objectives and Methods

The overarching purpose of the blast protection project is to provide an improved helmet capable of providing better blast protection from TBIs that the current helmet can. As a contribution to that goal, this work aims to develop and validate a numerical model that will provide insight into the physics of blast phenomena interacting with a helmet and head as well as design support for liner optimization. To this end, both experimental and numerical work is performed on the current Advanced Combat Helmet (ACH) as well as the ACH with a modified liner.

Previous work on this project has focused on blast loading of sandwich structures, investigating capabilities of different filler materials compared to a standard ACH pad in a more basic and enlightening setting. This work has shown promising results, and this project extends the idea to more realistic geometries. As a first step, a design for an initial prototype of an actual liner is conceived from the same foam material used in sandwich structure testing, namely VN600 from provided by Der-Tex Corporation (Saco, ME). Several samples of this prototype are then constructed via a simple hand lay-up technique. Experimental work on these liners inserted into the current ACH shell is carried out at Purdue University. The modified helmets are loaded via an explosive drive shock tube. Five pressure transducers are placed inside the head surrogate during these experiments to record the pressure history during the blast event. The main features investigated from these pressure histories are the peak pressure, rise time, and time duration of the blast.

Armed with these experimental results, a numerical model is then developed to describe the physics of these blast events. Material characterization is important to the accuracy of these simulations. Most material parameters are taken from available literature. Material models are not readily available for VN600 foam or for glass beads. Therefore, a split-Hopkinson pressure bar is used to assess the high strain rate behavior of the foam, and a material model was developed by Dr. Simona Socrate at MIT. For glass beads, consolidation tests are performed in the Civil Engineering department at MIT to obtain a compressive stress-strain relationship. These results are then fit to a material model for use in simulations.

The numerical model is developed in the commercially available nonlinear finite element code ABAQUS® v6.10. Most of the modeling is done using ABAQUS®/CAE, while initial conditions are largely written to the input file via a script implementing an analytical blast field solution. The blast model is initialized with a static step taken with ABAQUS®/Standard, and the blast event is simulated with

ABAQUS®/Explicit. Results from the dynamic simulations are then compared with experimental results to assess the strengths, weaknesses, and overall validity of the numerical model.

## 1.3 Thesis Organization

This thesis is broken up into five major sections: background and literature survey, discussion of previous work on this project at MIT, material characterization, experimental work and results, and numerical modeling and results.

Chapter 2 includes background information and a description of other work related to this project. The chapter is further divided into a discussion of proposed blast injury mechanisms, characteristics of blast waves in air, interaction of blast waves with structures, and blast mitigation strategies. Section 2.2 particularly discusses in detail the analytical blast field solution that is used to initialize the blast wave in the numerical model.

In Chapter 3 is a discussion of the evolution of the filled helmet liner project at MIT. First, the original sports helmet research and findings are discussed. Then, a description of the blast protection research leading up to this project is discussed to lay the ground work for much of what is found here.

In Chapter 4, a discussion of material characterizations used for numerical modeling is presented. This section includes a discussion of the experimental work performed to develop material models for VN600 foam and for glass beads.

In Chapter 5, all aspects of the blast experiments are discussed. Topics include a description of the prototype liner used for experimental and numerical work, a description of the test setup and data recording technique, and presentation and discussion of the results obtained.

The numerical model, including geometry, mesh, boundary conditions, initial conditions, and simulation parameters, is discussed in Chapter 6. Also presented here are the results obtained as well as a detailed discussion of their consistency with the experimental results.

Finally, Chapter 7 presents the conclusions gleaned from this work as well as suggestions for future work on the project.

# Chapter 2 Background and Related Work

This project is multi-disciplinary in nature, involving topics from structural and solid mechanics, fluid dynamics, shock physics, material science, medicine, and computational science. In a closely related thesis (4), a thorough literature survey was presented on the causes and diagnosis of TBIs. Causes of TBI are briefly reviewed here, along with a broad presentation of blast mitigation strategies as well as computational work performed related to shock loading and propagation.

## 2.1 Blast Injury Mechanisms

The effect of blast on humans has been a topic of research for several years. During World War I, two British Army physicians, Dr. Fred Mott and Dr. Gordon Holmes, studied soldiers who had survived exposure to blast (it was out of these efforts that the phrase "shell shock" came into use) (5)(6)(7)(8). Due to very limited medicinal diagnosis capabilities (by their own admission), they had difficulty distinguishing between emotional and physical trauma due to blast. Indeed looking back it is likely many TBIs were misdiagnosed as "psychic trauma" by their methods (9). In 1968, Bowen, et. al. (10) compiled and analyzed several years worth of data from studies of animals exposed to blast waves. The results were interpreted to predict humans' survivability to varying blast wave intensities as shown in Figure 2-1.

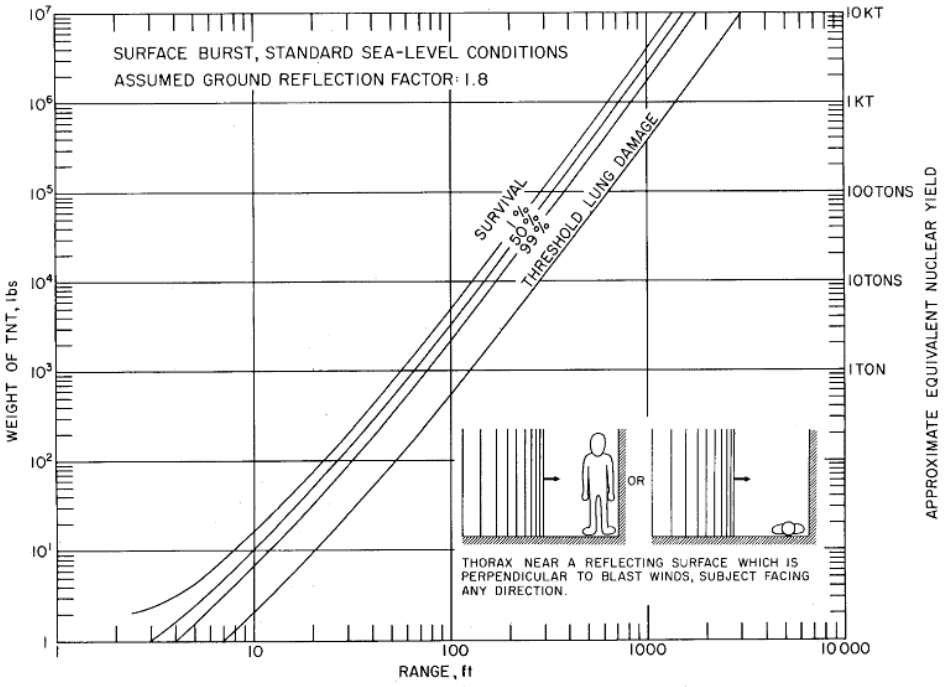


**Figure 2-1 - "Predicted survival curves for man exposed to surface bursts of TNT where the thorax is near a flat rigid surface reflecting the blast wave at normal incidence." (10)**

As reflected in the figure, Bowen et. at. focused on thoracic trauma because of, "the effects on the lungs being particularly important in determining morbidity or mortality" (10). His work is a good illustration of the category of blast injuries of interest in this project.

There are three general characterizations of blast-induced injury. Primary blast injuries result from air pressure fluctuations in the atmosphere causing stress and shear waves to pass through the body. Secondary injuries are caused by debris accelerated by the blast impacting a person, and tertiary injuries result when a person is accelerated into an object or wall as a result of the blast (3)(9). Both secondary and tertiary injuries can be recast as impact-type injuries, studied by a relatively large community including motorcycle and sports helmets manufacturers. In contrast, primary injuries are unique to blast exposure, and indeed these are the type of injuries of interest in this project. Most literature available on primary blast-induced injury originates from war-related injuries, though some cases are known involving civilian incidents involving, for example, fireworks (9).

The work of Bowen mentioned above may have direct implications for primary blast-induced TBI. Courtney and Courtney reviewed a large body of work suggesting TBIs may be caused by propagation of blast waves to the brain via a thoracic mechanism (11). Cernak hypothesizes that one of the possible reasons for alteration of brain function following blast exposure is transfer of kinetic energy from the blast overpressure through the great vessels in the abdomen and thorax to the central nervous system (12). In work supporting this hypothesis involving animal models, blast waves focused on the thorax have shown such cerebral effects as suppression of electroencephalograpic (EEG) activity and hippocampal and hypothalamic neuron damage (11). Though the thoracic mechanism is a valid hypothesized cause of TBI, this project does not aim to curtail these effects.

Before looking at other mechanisms, it is instructive to understand what constitutes a TBI, particularly primary effects blast-induced TBI. Of course head penetration injuries qualify as TBIs, but these would be secondary or tertiary effects blast-induced. Taber et. al. provided an illustrative graphic (Figure 2-2) as well as informative description of the three most common types of TBI, diffuse axonal injuries (DAI), contusion, and subdural hemorrhage (9). DAIs are common following closed-head injuries and result from shearing, stretching, and/or angular forces pulling on axons and small vessels (9). Contusions result when the brain moves relative to and impacts the skull (9)(13)(14). One type of contusion injury, called the coup-contrecoup injury, is illustrated well in Figure 2-3 (13). For a frontal impact, the skull "slaps" the coup region, causing contusions. Lesions in the contrecoup region occur when the brain bounces off the inside of the skull. Furthermore, during different times negative

pressures are seen in both regions, leading to the possibility of development of "cavitation bubbles", the growth and collapse of which may lead to brain damage (13). Subdural hemorrhages result from the brain moving sufficiently far relative to the skull to tear tributary surface veins bridging the gap between the brain surface and the dural venous sinus (9).

As Chafi et. al. pointed out, blast waves can certainly cause acceleration/deceleration forces on the head, leading to contusions of the frontal and temporal lobes (14). Furthermore, these forces may impart shearing and rotational forces on the axons, for example due to tissues of different densities being accelerated at different rates, potentially leading to DAIs (14). Similarly, the high frequency shock loading can induce brain tissue stress and strains, also potentially leading to DAIs or subdural hemorrhages (14). To investigate these issues more closely, Chafi et. al. developed a three-dimensional non-linear finite element model employing an Arbitrary Lagrangian-Eulerian (ALE) method to aid with fluid-structure interaction (FSI) effects using the explicit FEM software LS-DYNA® (14). They found their model is able to accurately predict intracranial pressure (ICP) as well as stresses and strains within the brain.

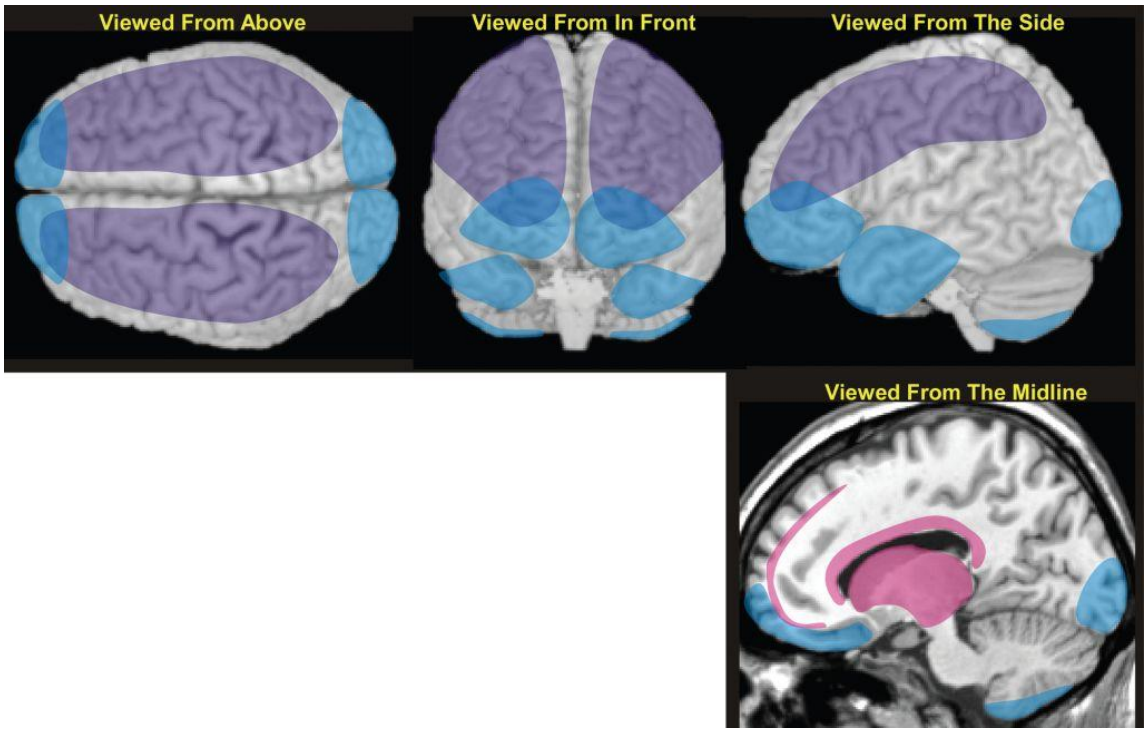


**Figure 2-2 - "The most common types of nonpenetrating traumatic brain injury are diffuse axonal injury, contusion, and subdural hemorrhage. The most common locations for diffuse axonal injury (pink) are the corticomedullary (gray matter-white matter) junction (particularly frontotemporal), internal capsule, deep gray matter, upper brainstem, and corpus callosum. The most common locations for contusions (blue) are the superficial gray matter of the inferior, lateral and anterior aspects of the frontal and temporal lobes, with the occipital poles or cerebellum less often involved. The most common locations for subdural hemorrhage (purple) are the frontal and parietal convexities." Figure and caption taken from (9)**

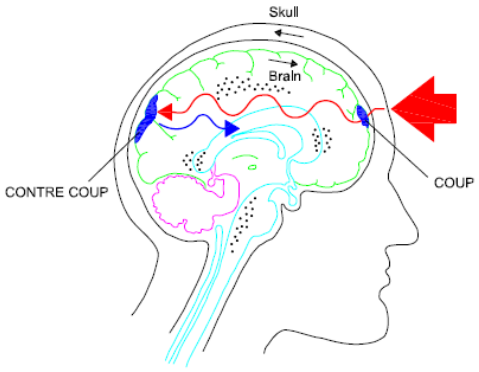


**Figure 2-3 - Coup-Contrecoup Injury - Figure taken from (13) adapted from (15)**

In a different simulation study, Nyein et. al. used the Virtual Test Facility (16)(17), a suite of integrated computational solid and fluid mechanics solvers, to investigate the response of a validated human head model (18) to a frontal blast (19). Specifically, and what is of high relevance to this project, they investigated the effect of the ACH on intracranial blast wave mitigation. They found that the main wave transmission pathways are the soft tissues directly in contact with the blast and that cavitation is more likely a result of wave reflections inside the skull rather than the blast wave underpressure (19). Furthermore, they discovered that the liner pads of the ACH provide a slight pressure concentration effect on the skull, but that overall that the ACH provides unappreciable mitigation of the blast wave. However, they also found that the ACH does not enhance the damage due to the blast wave, in contradiction with other findings using more simplistic models (i.e. (20)) (19). They did find that adding a face shield potentially can dramatically reduce the blast wave pressure transmitted to the brain for a blast exposure (19).

Taylor and Ford performed a modeling and simulation study to investigate the role of stress wave interactions in blast-induced TBIs (21). Simulation work was done using the shock physics code CTH, an Eulerian formulation finite-volume code capable of simultaneously tracking up to twenty different materials . They used high resolution photographic data to construct the head model, differentiating between skull, white matter, gray matter, and cerebrospinal fluid. Their results suggest that early-time stress wave interactions lead to stress localizations contributing to multifocal axonal injury (21). Furthermore, they suggest that blast-induced TBI may occur much earlier than previously thought, that is before the usual linear and rotational accelerations thought to cause TBI occur (21).

Although there has been a great deal of effort to understand the mechanisms behind blast-induced TBI (22), it remains a controversial and active topic of research as to whether or not the brain is

even susceptible to primary blast injury (9). However, this project, as do so many others, proceeds under the assumption that something can and should be done to mitigate primary blast-induced TBIs.

## 2.2 Air Blast Characteristics

IED detonations involve chemical explosions, whereby a condensed explosive material (either solid or liquid) rapidly oxidizes, creating very hot high pressure gases (23). Large amounts of energy are released, leading to local high pressures. In chemical explosions, almost all of this energy expands outwards in the form of a shockwave. As the blast wave moves outwards, the air pressure falls back to atmospheric pressure. Because of the momentum of the gas particles, the pressure briefly falls below atmospheric pressure, causing the characteristic "underpressure" of the blast (23).

A typical pressure time trace of a point in the path of an "ideal blast wave" is shown in Figure 2-4. The air at the point of interest is initially at atmospheric pressure $p_0$. With the arrival of the blast wave at the arrival time $t_a$, the pressure experiences a discontinuous jump to the blast peak overpressure $p_S^+ + p_0$. The pressure then decays back to atmospheric pressure at time $t_a + T^+$. As mentioned before, gas molecule momentum causes the pressure to briefly drop slightly below atmospheric pressure to the peak underpressure $p_0 - p_S^-$. After a length of time $T^-$ the air returns to atmospheric pressure. Important blast quantities illustrated by Figure 2-4 include the positive phase duration $T^+$ and the peak overpressure $p_S^+$. In reality, the jump in pressure does not occur discontinuously, and a parameter of interest is the time it takes to attain the peak over pressure, called the rise time $t_r$. Finally, the specific impulse of the positive phase duration, as defined in Equation 2-1, is also of interest (23).

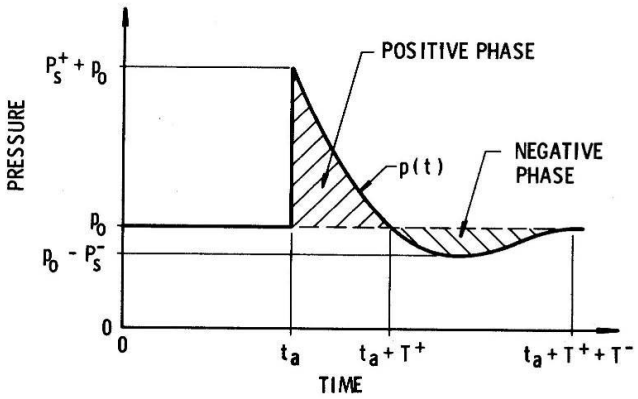


**Figure 2-4 - Characteristics of an "ideal blast wave" (24)**

$$i_S = \int_{t_a}^{t_a+T^+} \left(p(t) - p_0\right) dt$$

**Equation 2-1**

It is often of interest to have an expression describing the profile shown in Figure 2-4. One such expression, known as the Friedlander equation is given in Equation 2-2 (23)(25).

$$p(t) = p_S^+ \left[1 - \frac{t}{T^+}\right] \exp\left\{-\frac{bt}{T^+}\right\}$$

**Equation 2-2**

The parameter $b$ is known as the waveform parameter and is a function of peak overpressure (23).

Of course, it is instructive to know how a blast wave travels through air. To investigate this, one can employ the ideal gas model for air assuming a non-temperature dependent constant volume specific heat.

$$p_e = NR\rho\vartheta = (\gamma - 1)c_v\rho\vartheta = \left(\frac{c_p}{c_v} - 1\right)c_v\rho\vartheta$$

**Equation 2-3**

$$E = c_v\vartheta$$

**Equation 2-4**

Here, $p_e$ is the equilibrium pressure of the air, $N$ is the mole number, $R$ is the universal gas constant, $\rho$ is the density, $\vartheta$ is the temperature (on an absolute scale), $E$ is the internal energy, $c_p$ is the constant pressure specific heat, and $c_v$ is the constant volume specific heat (26). Equation 2-4 is valid only in the situation that $c_v$ is a constant. This assumption will remain in effect throughout this project. For a shockwave passing through air initially at rest, the following jump conditions can be derived from the conservation of linear momentum and conservation of energy, respectively (26).

$$-NR(\rho_+\vartheta_+ - \rho_0\vartheta_0) = \rho_0 C_S^2(F_+ - 1)$$

**Equation 2-5**

$$\rho_0 c_v(\vartheta_+ - \vartheta_0) = -NR\rho_0\vartheta_0(F_+ - 1) + \tfrac{1}{2}\rho_0 C_S^2(F_+ - 1)^2$$

**Equation 2-6**

Here, the + subscript indicates the region immediately behind the shock, and the 0 subscript indicates the properties of the air at rest. States achieved immediately behind the shock are known as Hugoniot states. Also, $F_+ = \rho_0/\rho_+$ and $C_S$ is the shock velocity. These relationships can be combined to the relationship shown below (26).

$$(1-F_+)\{[F_+ + 1/2(\gamma-1)(F_+-1)]M^2 - 1\} = 0$$

**Equation 2-7**

Here, the Mach number $M = |C_S|/c_0 = U_S/c_0$ and the speed of sound in air $c_0^2 = \gamma(\gamma-1)c_v\vartheta_0$ have been used (26). Equation 2-7 allows for two states of the material. The first, $F_+ = 1$ corresponds to the material at rest. The other state is given below.

$$1 - F_+ = \frac{2}{\gamma-1}\left(1 - \frac{1}{M^2}\right)$$

**Equation 2-8**

Solving Equation 2-8 for the deformation gradient after the shock yields the jump in density across the shock as a function of the shock velocity.

$$\frac{\rho_+}{\rho_0} = \frac{M^2(\gamma+1)}{M^2(\gamma-1)+2}$$

**Equation 2-9**

Solving Equation 2-8 for the Mach number yields an expression for the shock velocity in terms of the peak overpressure $p_S^+ = p_+ - p_0$ (27).

$$U_S = \sqrt{\frac{p_0}{\rho_0}}\sqrt{\frac{\gamma+1}{2}\frac{p_S^+}{p_0}+\gamma}$$

**Equation 2-10**

Combining Equation 2-5 and Equation 2-6 and inserting the expression for the Mach number obtained from Equation 2-8, the following expression for jump in temperature across the shock is obtained (26).

$$\frac{\vartheta_+}{\vartheta_0} = F_+\left(\frac{1-F_lF_+}{F_+-F_l}\right)$$

**Equation 2-11**

$$F_l = \frac{\gamma-1}{\gamma+1}$$

**Equation 2-12**

Having the temperatures and densities, the pressure jump across the shock can be determined from Equation 2-3 (27).

$$\frac{p_+}{p_0} = 1+\frac{2\gamma}{\gamma+1}\left(M^2-1\right)$$

**Equation 2-13**

In the limit of an infinitely strong shock in an ideal gas initially at rest (i.e. $M \to \infty$), from Equation 2-8 it can be seen that $F_+ \to F_l$. For air, $\gamma = 1.4$, and Equation 2-12 reveals that a strong shock in air can increase the density by at most a factor of 6 (26).

The relations above generally express the properties at the blast discontinuity. However, it is useful to have a description of the whole blast domain. An important technique to generate such a description is known as theory of point blast waves (28). Sedov (29), von Neumann (30), and Taylor (31) describe exact self-similar solutions to the equations of fluid dynamics; however, these solutions are only valid for very strong shocks (28)(32). Sakurai (33) developed a perturbation solution in an attempt to accurately describe the blast over the whole regime of shock strengths (28). He assumed a linear velocity profile behind the shock and that the derivative of the density with respect to the Mach number

can be neglected. These two assumptions lead to relatively inaccurate results in the weak shock regime (28).

Following the same general approach as Sakurai, Bach and Lee developed the theoretical basis for a point blast solution valid over the full regime of shock strengths (28)(34). They start from the mass (Equation 2-14), momentum (Equation 2-15), and energy (Equation 2-16) conservation equations given below for unsteady adiabatic expansion of a blast wave.

$$(\phi-\xi)\frac{\partial\psi}{\partial\xi}+\psi\left(\frac{\partial\phi}{\partial\xi}\right)+j\phi\frac{\psi}{\xi}=2\theta\eta\frac{\partial\psi}{\partial\eta}$$

**Equation 2-14**

$$(\phi-\xi)\frac{\partial\phi}{\partial\xi}+\theta\phi+\frac{1}{\psi}\frac{\partial f}{\partial\xi}=2\theta\eta\frac{\partial\phi}{\partial\eta}$$

**Equation 2-15**

$$(\phi-\xi)\left(\frac{\partial f}{\partial\xi}-\frac{\gamma f}{\psi}\frac{\partial\psi}{\partial\xi}\right)+2\theta f=2\theta\eta\left(\frac{\partial f}{\partial\eta}-\frac{\gamma f}{\psi}\frac{\partial\psi}{\partial\eta}\right)$$

**Equation 2-16**

$$\phi(\xi,\eta)=\frac{u(r,t)}{\dot{R}_S(t)}\quad f(\xi,\eta)=\frac{p(r,t)}{\rho_0\dot{R}_S^2}\quad \psi(\xi,\eta)=\frac{\rho(r,t)}{\rho_0}$$

**Equation 2-17**

$$\theta(\eta)=\frac{R_S\ddot{R}_S}{\dot{R}_S^2}\quad \xi=\frac{r}{R_S(t)}\quad \eta=\frac{c_0^2}{\dot{R}_S^2}=\frac{1}{M^2}$$

**Equation 2-18**

In these equations, $r$ is the distance from the point of detonation, $R_S, \dot{R}_S, \ddot{R}_S$ are the location, radial velocity, and radial acceleration of the blast front, respectively, and $u$ is the air particle velocity. Also, for a spherical blast wave, $j=2$ (28). These equations are solved with the following boundary conditions at the blast front, following from the normal shock conditions derived above (28).

$$\phi(1,\eta) = \frac{2}{\gamma+1}(1-\eta)$$

**Equation 2-19**

$$f(1,\eta) = \frac{2}{\gamma+1} - \frac{\gamma-1}{\gamma(\gamma+1)}\eta$$

**Equation 2-20**

$$\psi(1,\eta) = \frac{\gamma+1}{\gamma-1+2\eta}$$

**Equation 2-21**

The key to method of Bach and Lee is assuming a power law relationship the density profile.

$$\psi(\xi,\eta) = \psi(1,\eta)\xi^{q(\eta)}$$

**Equation 2-22**

The exponent is solved by plugging Equation 2-22 into the mass conservation integral.

$$q(\eta) = (j+1)[\psi(1,\eta)-1]$$

**Equation 2-23**

Equation 2-22 and Equation 2-23 can be used along with the conservation mass (Equation 2-14) and the boundary condition $\phi(0,\eta) = 0$ (the velocity at the detonation point is zero by symmetry) to obtain an expression for the particle velocity behind the blast discontinuity.

$$\phi(\xi,\eta) = \phi(1,\eta)\xi(1-\Theta\ln\xi)$$

**Equation 2-24**

$$\Theta = \frac{-2\theta(\eta)\eta}{\phi(1,\eta)\psi(1,\eta)}\frac{d\psi(1,\eta)}{d\eta}$$

**Equation 2-25**

The expressions for density and particle velocity and their derivatives are plugged into the conservation of momentum equation and integrated to obtain an expression for the dimensionless pressure.

$$\begin{aligned} f(\xi,\eta) &= f(1,\eta)+ f_2\left(\xi^{q+2}-1\right)+ f_3\left[\xi^{q+2}\left[(q+2)\ln\xi-1\right]+1\right]+ \\ & f_4\left[2-\xi^{q+2}\left[(q+2)^2\ln^2\xi-2(q+2)\ln\xi+2\right]\right] \end{aligned}$$

**Equation 2-26**

$$f_2=\frac{\psi(1,\eta)}{q+2}\left[(1-\Theta)\left\{\phi(1,\eta)-\phi^2(1,\eta)\right\}-\theta\left\{\phi(1,\eta)-2\eta\frac{d\phi(1,\eta)}{d\eta}\right\}\right]$$

**Equation 2-27**

$$f_3=\frac{\psi(1,\eta)}{(q+2)^2}\left(\theta\left\{\Theta\phi(1,\eta)-2\eta\frac{d}{d\eta}\left[\Theta\phi(1,\eta)\right]\right\}-\Theta\phi(1,\eta)-\Theta^2\phi^2(1,\eta)+2\Theta\phi^2(1,\eta)\right)$$

**Equation 2-28**

$$f_4=\Theta^2\phi^2(1,\eta)\frac{\psi(1,\eta)}{(q+2)^2}$$

**Equation 2-29**

The solution of the dimensionless particle velocity and pressure profiles requires knowledge of $\theta(\eta)$ as well as its derivative. Plugging in the density, particle velocity, and pressure expressions into the conservation of energy integral, the following relationship is obtained (28).

$$\begin{aligned} \frac{d\theta}{d\eta}=-\frac{1}{2\eta}\left\{\theta+1-2\phi(1,\eta)-\frac{D_1+4\eta}{\gamma+1}-(\gamma-1)(j+1)\left[\phi(1,\eta)-\frac{(D_1+4\eta)^2}{4\theta\gamma(\gamma+1)}\right]\right\}+ \\ \frac{D_1+4\eta}{8\eta^2(\gamma+1)}\left[\frac{(D_1+4\eta)\phi(1,\eta)}{\theta}-\frac{\phi(1,\eta)(\gamma+1)}{\theta\psi(1,\eta)}+2(\eta+1)+(\gamma-1)(j+1)\frac{\gamma+1}{2\theta}\phi^2(1,\eta)\right]+ \\ \frac{2\theta\left[2+(\gamma-1)(j+1)\right]}{D_1+4\eta} \end{aligned}$$

**Equation 2-30**

$$D_1 = \gamma(j+3)+(j-1) \quad y = \left(\frac{R_S}{R_0}\right)^{j+1} \quad R_0 = \left(\frac{E_0}{\rho_0 c_0^2 k_j}\right)^{\frac{1}{j+1}}$$

**Equation 2-31**

In Equation 2-31, $E_0$ is the energy released by the blast and $k_j = 1,2\pi,4\pi$ for $j = 0,1,2$ (28). Differentiating the expression for $y$, the following expression is obtained (28).

$$\frac{dy}{d\eta} = -\frac{(j+1)y}{2\theta\eta}$$

**Equation 2-32**

Equation 2-30 and Equation 2-32 are a system of ordinary differential equations that can be numerically integrated (e.g. with fourth-order Runge-Kutta) to fully describe the point blast solution pressure and particle velocity (28). Numerical integration must proceed from the initial condition $\theta(0) = \theta_0$ and $y(0) = 0$. However, both Equation 2-30 and Equation 2-32 are singular at this condition. To circumvent this difficulty, Bach and Lee begin the numerical integration from a small perturbation of $\eta$ and expand an initial condition of the following form (28).

$$\theta(\eta) = \theta_0 + \theta_1\eta + \theta_2\eta^2 + \theta_3\eta^3$$
$$y(\eta) = y_1\eta + y_2\eta^2 + y_3\eta^3 + y_4\eta^4$$

**Equation 2-33**

Coefficients of Equation 2-33 are provided in Appendix A. Results of Bach and Lee's method are provided below along with a comparison with other attempts (28).

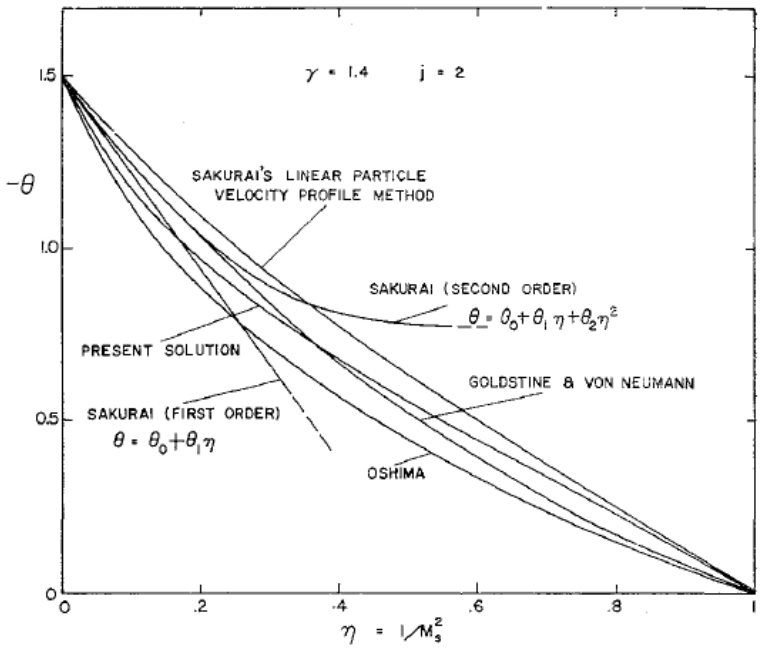


**Figure 2-5 - "The variation of the shock decay coefficient $\theta$ vs shock strength $\eta$ for spherical blast waves, $\gamma$ =1.4" (28)**

## 2.3 Air Blast Interactions With Structures

Air blast interaction with structures has been an important topic of research as well. A simple yet informative analysis to examine is that of a blast wave normally reflecting off of an infinitely rigid surface. The pressure of the air impinging on the rigid surface has two components, the static pressure and the dynamic pressure. For air, the reflected pressure $p_r$ can be related to the atmospheric pressure and peak overpressure of the blast wave as shown below (23).

$$p_r = 2p_S^+ \frac{7p_0 + 4p_S^+}{7p_0 + p_S^+}$$

**Equation 2-34**

For peak overpressures very small compared to atmospheric pressure, the minimum reflected pressure is twice the peak overpressure. In the opposite limit, the maximum reflected pressure is eight times the peak overpressure. Equation 2-34 was derived by Rankine and Hugoniot assuming air behaves like a real gas with a constant ratio of specific heats. Experimentally measured ratios of reflected pressure to peak overpressure have reached as much as twenty (23).

Kambouchev, Noels, and Radovitzky have performed several studies extending Taylor's (35) analysis of fluid-structure interaction for waves in the acoustic range (27)(32)(36)(37). Taylor showed that the impulse transmitted by a reflected wave to a free-standing plate is reduced due to pressure relief effects caused by the motion of the plate (32)(35). Kambouchev et. al. investigated this effect analytically for uniform (37) and exponential (36) incident blast profiles of arbitrary intensities for the asymptotic limits of very heavy and very light plates (32). They also developed a numerical method to simulate blasts having arbitrary profiles incident on a free-standing plate. The method is a shock-capturing finite-difference scheme solving the Lagrangian form of the equations of compressible flow based largely on the von Neumann and Richtmyer algorithm (38) as presented by Drumheller (26)(32). The method is applied not only to uniform and exponential profiles but also to the point source solution provided by von Neumann and Sedov(30)(29). Through simulations and analytical work Kambouchev et. al. demonstrate that fluid-compressibility effects greatly affect the momentum transmitted to a free-standing plate from an incident blast wave (32). Specifically, lighter plates acquire less momentum at the cost of greater displacement (32).

There have been many studies on the interaction of blast waves with cellular materials (i.e. foams and honeycombs), defined by Gibson and Ashby to be materials "made up of an interconnected network of solid struts or plates which form the edges and faces of cells" (39). The most important property defining these materials is the relative density: the ratio of the density of the cellular material to that of the solid material composing the walls of the cells (39). Once this ratio exceeds 0.3, the material is no longer cellular but rather is a solid material containing isolated pores (39).

Mazor et. al. considered the effect of inserting a foam at the end of a shock tube on the pressure transmitted to the back wall of the tube following an incident shock wave (40). They develop the governing equations for the problem and offer a proof for why insertion of the foam can only increase the pressure transmitted to the back wall as demonstrated experimentally by Skews et. al. (41) and others (40). In fact, the results of Gvozdeva et. al. (42) investigating this problem with polyurethane foam suggest the peak pressure reflected from the end wall of the shock tube is higher due to the foam, this peak pressure increases as the initial length of the foam increases, and that there is an asymptotic limit where the increase in length of foam no longer increases the peak pressure (43). Ben-Dor et. al. investigated this uniaxial strain problem further experimentally and numerically (using the von Neumann and Richtmyer algorithm) with an open-cell polyurethane foam (43). The major outcomes of this effort were validation of their numerical simulation code qualitatively with their own experiments

and those of others as well as determination some dependencies of the shock propagation through the foam specific to the uniaxial strain case (43).

Li and Meng modeled shock propagation through a cellular material using a one-dimensional mass-spring model (44). While cellular materials generally attenuate low-intensity pulse pressures when the stress waves do not cause densification, Li and Meng considered the "unpredictable" behavior when higher intensity stress waves are transmitted. Their results suggest that blast pulse shape helps determine whether the shock is enhanced or attenuated in a cellular material. Furthermore, their model indicates that while momentum and energy decrease as the shock passes through a cellular material from nonlinear dissipation, the peak stress or pressure may be amplified. They develop dimensionless parameters for material properties and loading conditions to give critical conditions for blast pulse transmission enhancement. It should be noted, however, that this model considered only the structure of the solid phase of the cellular material; consideration of the fluid phase may provide additional insights into the behavior under shock loading (44).

Hanssen et. al. investigated the effect of aluminum foam panels on the energy and impulse imparted to a blast pendulum due to a close-range detonation (45). Their experimental results showed that the impulse and energy transferred to the pendulum increased with the addition of foam panels. They try to explain the results through an analytical solution and non-linear finite element simulation in LS-DYNA®. Though the results were not explained as expected, they did show that while the local response to a blast can be shaped by addition of the foam panels, the global response of the structure is governed by the total impulse imparted rather than the shape of the impulse. They do suggest that the increased transmission of impulse and energy may be due to the change in shape of the original planar panel geometry to a double-curved geometry (45).

Levy et. al. considered propagation of shock waves in rigid porous materials via numerical simulations (46). They used a multiphase approach considering the dynamics of both the solid composing the porous structure as well as the fluid inside the structure at the representative elementary volume level. An upwind shock-capturing total variation diminishing scheme for the governing equations was developed and validated against experimental results for a number of different initial conditions, providing the first time compaction waves in a porous media were successfully simulated (46).

Several investigators have considered shock wave propagation through sandwich structures. Xue and Hutchinson conducted a numerical study using the explicit form of the finite element software ABAQUS® comparing the deflection of a metal sandwich structure to that of a solid metal structure of equal mass. Their results suggest that such sandwich structures outperform their solid counterparts of equal material and weight if the core of the sandwich structure is sufficiently strong (47). This analysis, however, neglected important aspects of the blast problem, including fluid-structure interaction and strain-rate dependence of materials. Later, Qiu et. al. looked at the same problem analytically and computationally (using ABAQUS®) including fluid-structure interaction effects and strain hardening (48). Their computational results showed reasonable agreement with the analytical ones They conclude that strain hardening had a negligible effect on this sandwich plate response and confirm the conclusion of Xue and Hutchinson that an optimized sandwich design can sustain a larger shock impulse than a monolithic design of the same mass and material (48).

Zhuang et. al. examined shock propagation through bi-material sandwich structures of alternating polycarbonate and either glass, aluminum, or stainless steel via flyer-plate experiments (49). They found a number of interesting things, including the following: 1) Periodically layered composites can support steady structured shock waves. 2) Scattering of the shock wave due to internal interfaces slows the propagation velocity of the wave and increases the rise time of the shock. 3) Also, the higher the intensity of the shock, the steeper the shock front. 4) Furthermore, increasing the number of interfaces while maintaining the total weight of each constitutive material increases the nonlinearity of the composite as well as contributes to greater energy dissipation. 5) Finally, impedance mismatch between constitute materials contributes to the dissipation and dispersion of the shock wave (49).

Berezovski et. al. investigate a similar set-up as did Zhuang in a computational context (50). They employ a composite wave propagation scheme involving a Gudonov step after several second-order Lax-Wendroff steps to solve the one-dimensional governing equations. Results are shown to agree well with those of Zhuang. Furthermore, they explore a parameter of non-linearity incorporating material, geometrical, and blast information to help determine the response characteristics (50).

Main and Gazonas considered the optimization of a sandwich structure consisting of two solid plates sandwiching a cellular material (51). They propose an analytical solution and then compare these results with a finite element simulation in LS-DYNA® for the problem of an air-blast incident on the structure with the back face unconstrained. It was found that the capacity of the sandwich structure to mitigate shock transmission was limited by the impulse required to create full densification in the core

cellular material. Furthermore, their results suggest blast mitigation is enhanced with increasing the fraction of total mass in the front face of the sandwich structure. This, however, leads to undesirable back face accelerations and, therefore, they propose an optimal mass ratio for a maximum allowed back face acceleration (51). Karagiozova et. al. used the commercial finite element code ABAQUS® to investigate air-blast loading of sandwich structures including an aluminum foam core (52). They found that optimizing a blast mitigation structure of this type depends on the interaction effects of sandwich geometry and material properties.

## 2.4 Blast Mitigation Strategies

An incredibly important reason to understand the characteristics of blast waves as well as their interactions with structures and materials is to be able to design equipment to protect people and infrastructure from ill-intentioned blast effects. A popular method of blast wave mitigation under consideration is use of water. Chong et. al. developed and validated a finite element model in MSC-Dytran® demonstrating the effectiveness of volumes of water surrounding an explosive mitigating the blast effects (53). Overpressure and impulse density are reduced when the shock breaks up the water into droplets, further increasing the surface area available for heat transfer for vaporization and reducing the temperature of the surroundings. Their findings were consistent with previous experimental results indicating that the higher the water to explosive ratio, the greater the reduction in peak pressure from the blast (53). Homae et. al. considered surrounding an explosive with a mixture of water gel and small foam polystyrene spheres as well as sand (54). Their results suggest for a given mass, the lower density mixtures provide superior blast mitigation, while for a given volume, the 50/50 mixture of sand to polystyrene or sand provide the best blast mitigation (54).

Schwer and Kailasanath take a different approach using numerical simulations to investigate the effect of a water mist on a blast (55). Through parametric studies, they indicate a number of conclusions regarding the effectiveness of water mist at blast mitigation. First, they suggest the mitigation of the shock-front using water mist is through momentum extraction. Next, for a water mist to be effective, it does not need to be directly adjacent to the explosive, just relatively close. Furthermore, they showed a relatively diffuse mist of water may be just as effective as having a "water wall" surrounding the explosive. In addition, results indicate that there exists an optimal droplet size to maximize mitigation at various distances from an explosive (55).

Of course, other mitigation techniques not using water exist as well. Pfannes et. al. investigate shock propagation through a chain of elastic spheres of gradually reducing diameters, also referred to as "tapered granular chains' (56). When larger spheres contact smaller spheres, momentum is conserved while kinetic energy is not. The effect of the tapered granular chain is to decimate the original shock into tiny shocks. These tiny energy bundles are eventually absorbed by the system due to friction and restitution effects. Results of the study indicate that the greater the tapering of the beads the higher the absorption of the shock energy by the system (56).

Nesterenko surveys use of "soft" condensed matter (including granular and porous materials and foams) for blast mitigation (57). According to Nesterenko, the important parameters of a "soft" condensed matter for determining blast mitigation capabilities are density, porosity, and relative geometrical size. Furthermore, blast mitigation may be enhanced by including larger pores along with the smaller pores in the material, allowing energy absorption through large displacements of adjacent particles as large pores collapse. In accordance with other efforts, Nesterenko agrees that nonlinearity of periodically layered composites and granular materials may be exploited to tailor the response of a structure to shock loading. Furthermore, while shock enhancement by "soft" condensed materials is possible, it can be avoided by using a sufficiently thick layer of material. The main conclusion from the broad survey of work is that these types of materials can be successfully used for shock/blast wave mitigation (57).

Allen et. al. investigated the blast mitigation characteristics of different material properties (58). Experiments were performed by surrounding an explosive by water, glycerin, expanded Perlite, or sand. They found that porosity plays an important role in determining blast mitigation capabilities and that there exists and optimum porosity for blast mitigation for a given material. Furthermore, they found that more dense materials provide a greater level of blast attenuation and that evaporation of water did not provide a mitigating mechanism (58).

# Chapter 3 The Use of Filler Materials for Head Protection

The use of a fluid-filled helmet to protect against head trauma has been considered before. In his 1971 patent, Morgan describes a multitude of chambers connected through valves inside a helmet structure (59). Some of the chambers would be filled with a nearly incompressible fluid. Upon impact, the fluid would be forced through the valves into the empty chambers. Then, through clever design, the fluid would return to the original chambers. The energy required to achieve this fluid motion represented a direct measure of the impact energy dissipated (59). Others have made similar efforts. Patents by Holt (60), Villari (61), Gooding (62), Hosaka (63), Calogne (64), and Mendoza (65) spanning the last four decades all describe some manner of including fluid inside helmet liners. These patents all focused on improving protection from head impacts, not from blast loading as is the focus of this study.

Improvement of helmets in general has been an active research topic, moreso for impact protection than for blast protection. Forero Rueda et. al. investigated different designs of liners for equestrian helmets using finite element simulations (66)(67). In the first paper, they looked at the performance of two different liners: the first was composed of three layers of foam of different densities and the second was a conventional liner composed of a single foam. Results indicated that attenuation of peak acceleration was tied to the contact area, distribution of material stresses, and dissipated plastic energy density. Peak accelerations were reduced by increasing contact area and varying foam density through the thickness to ensure plastic absorption of energy as the foam deforms (66). In a second paper, Cui et. al. consider a functionally graded foam of varying density rather than layers of different density foam to avoid delamination and crack propagation, and similar results were obtained to those in the first paper (67).

In a very interesting and relevant paper, Aare and Kleiven describe simulations using LS-DYNA3D® of ballistic impacts on a human head wearing a military helmet (68). The helmet used in this study is the Personal Armor System Ground Troops' (PASGT) helmet, the predecessor to the Advanced Combat Helmet (ACH) being considered in this study. Their simulations indicate that there exists an optimal helmet shell stiffness to prevent stress transmission to the skull, though no implications on pressure transmission to the brain are indicated (68).

## 3.1 Sports Helmet Research at MIT

Professor Young at MIT has pursued improved helmet performance via inclusion of filler materials in foam liners of sporting helmets since 2004 (69). The original idea included a liner

constructed from a closed-cell foam containing a series of channels and reservoirs to spread the forces from impact and distribute the fluid to different areas in the liner away from the impact site. In general, the liner was to include a mesh of coupled channels and reservoirs filled with an incompressible fluid. The proposed mechanisms for increased biomechanical protection were reduction in the peak force as well as lengthening of the duration of the forces caused by impact. A conceptual drawing of such a liner is shown below (69).

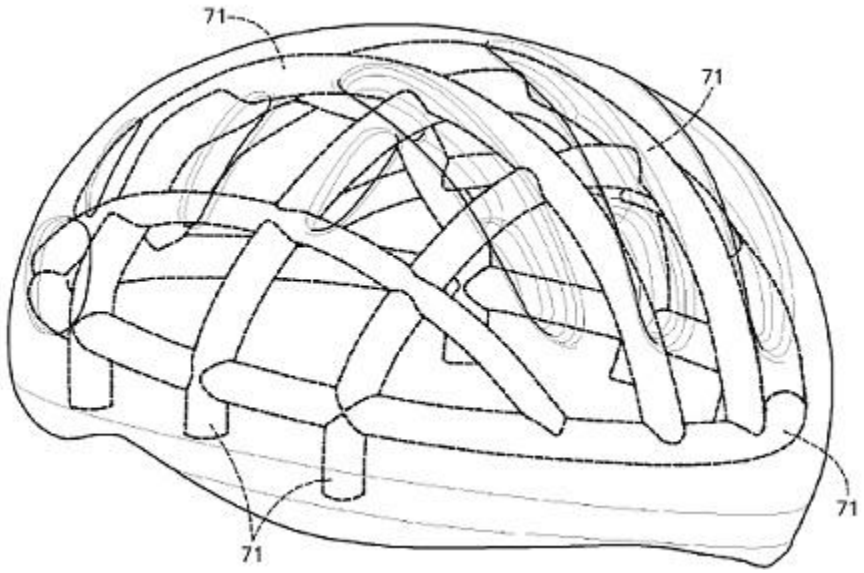


**Figure 3-1 - A mesh of interconnected channels (69)**

Claire and Vue investigated the effectiveness of viscous dissipation for peak acceleration reduction (70). They showed up to a 35% reduction in peak forces may be attained by surrounding VN600 foam - a closed-cell vinyl nitrile foam provided by Der-Tex Corporation (www.dertexcorp.com/) with a highly viscous fluid compared to the performance of the foam alone. Improvement was found in both spatial and temporal distribution of the forces using the viscous fluid. Furthermore, they showed acceleration reduction by including fluid-filled channels inside the VN600 (70).

Stewart completed a Master's degree thesis project investigating the benefits of the resilient VN600 over the traditional bicycle helmet liner material expanded polystyrene (EPS) and the effects of channel geometry and fluid filler viscosity on peak acceleration reduction (71). Experiments were performed via drop tests using a headform conforming to ASTM F1447-06 bicycle helmet drop testing standard. The headform was dropped onto a test sample resting on a flat anvil. The setup is shown below(71).

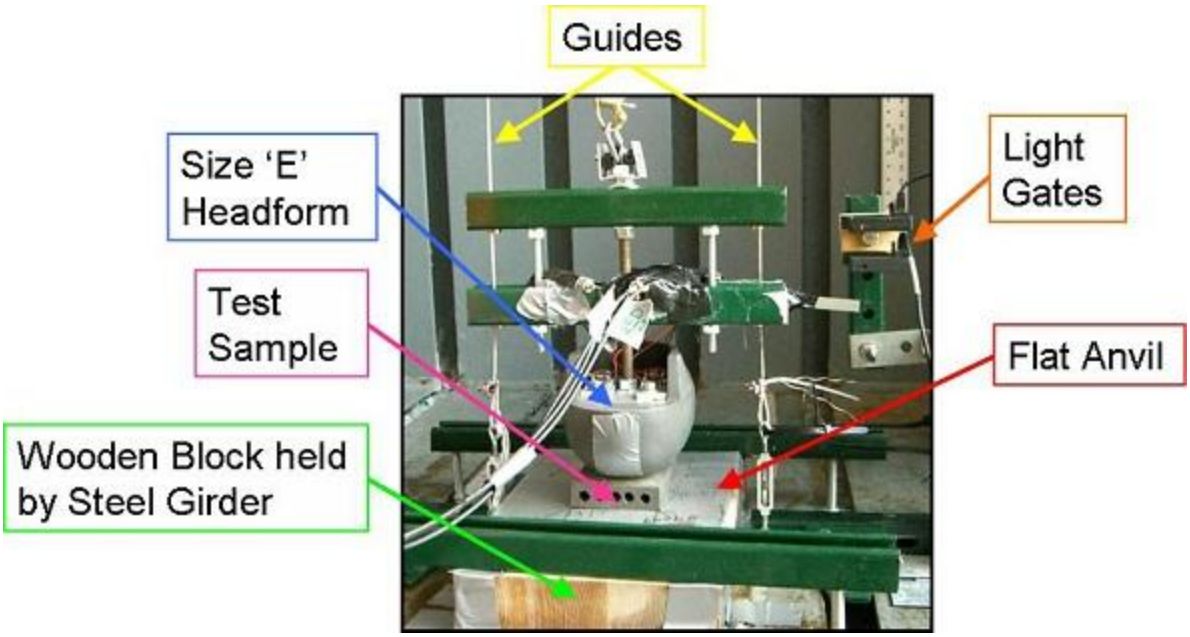


**Figure 3-2 - Drop Test Apparatus (71)**

Acceleration data was collected using accelerometers attached to the headform. Impact velocity was recorded via consecutive light gates. Tests were conducted using both constrained and unconstrained channels. That is, in one design fluid flowed freely into and out of the channels, whereas in the other fluid was trapped in the channels. Furthermore, multiple drops were performed on each sample, testing the integrity of the samples over multiple impacts(71).

Results showed that VN600 substantially outperformed EPS in terms of peak headform acceleration, especially over multiple impacts. Tests of samples of varying channel diameters using air and water with the channels constrained showed higher peak headform accelerations over samples with no filler materials, consistent with the findings of Claire and Vue (70). Tests using air and water in unconstrained channels showed noticeably different characteristics. Results for air were not appreciably different than those of no filler materials. However, using water as a filler material showed acceleration reduction, with the best reduction occurring with 3/8 in diameter channels. Other tests were conducted with various mixtures of water and glycerin as a filler material in unconstrained channels. Of the mixtures tested, the most effective at reducing peak acceleration was 30% glycerin by weight. A representative chart summarizing these results is provided below (71).

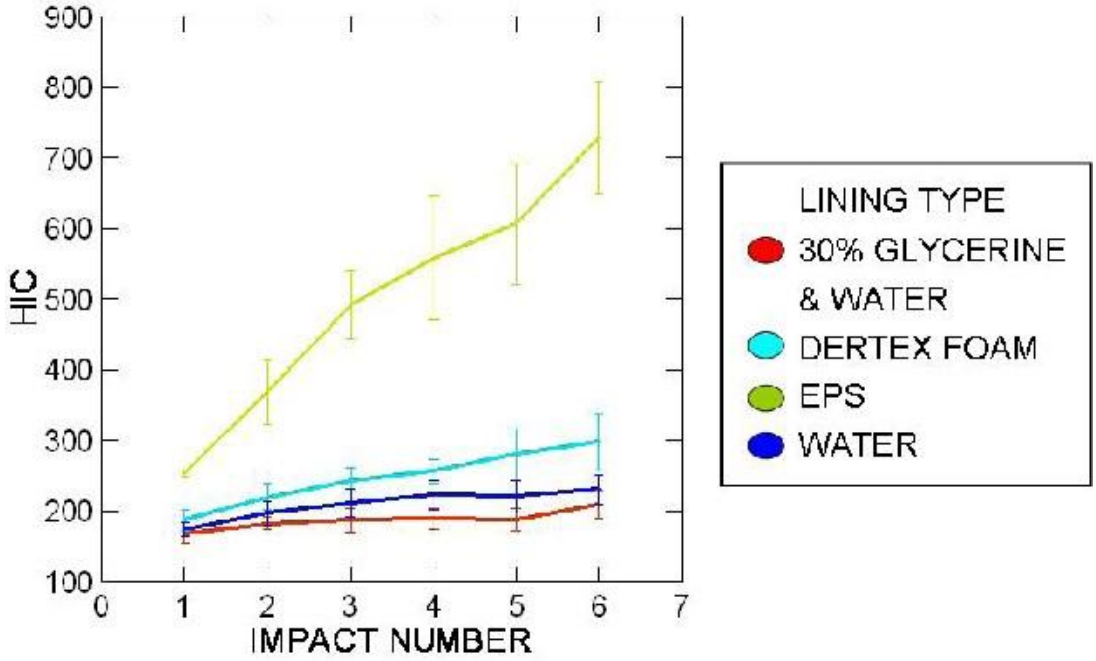


**Figure 3-3 - Performance of VN600 with and without channels compared to EPS (71)**

Testing was performed at MIT on ski helmets and other test samples as well using the same test apparatus as Stewart (4). The first set of tests demonstrated the superior performance of a high end ski helmet manufactured by POC® over a cheaper helmet in both impact and load-deflection tests. These helmets are shown below.

**Figure 3-4 - Ski helmets tested by Leedom (left) and POC (right) (4)**

Other testing involved samples of VN600 having either zero, one, or two channels filled with water, glycerin, or glass beads. In the dual channel configuration, only water was tested. Pictures of the samples are shown below.

**Figure 3-5 - (left) Solid block of VN600 (center) single channel (right) dual channel (4)**

Results from these tests indicate that for impact scenarios, smaller channels produced a lower acceleration with water as a filler than did larger channels. Furthermore, glycerin out-performed water as well. Both of these results indicate viscous losses contribute to stress wave mitigation in impact events. These preliminary results were encouraging enough to pursue this technology further as a head protection method (4).

## 3.1 Blast Protection Using Filler Materials

Promising results of using filler materials to provide protection from impacts encouraged application of the technology to the problem of blast-induced traumatic brain injury. In the first stage of this research, materials having various physical properties were tested in a simplified geometry to investigate their mitigation properties inside channels in VN600 foam. The second stage of the project is to investigate a design for an actual helmet prototype liner, which is the topic of this thesis.

For his Master's thesis, Alley performed blast experiments on sandwich structures containing the various filler materials (72). Samples were 10 in x 10 in x 1 in, and those with filler materials had an 8 in x 10 in x 0.5 in cavity. Samples were held between two 1/8 in thick pieces of poly(methyl methacrylate), or PMMA and were exposed to a blast from an explosive driven open-ended shock tube. The mouth of the shock tube was 12 in from the front of the test sample. The pressure measurement region behind the sample was surrounded by a PMMA enclosure to prevent the shock wave from converging around the sample and confounding the isolation of the transmitted shock strength. The experimental setup is shown in Figure 3-6. Data was collected with a pressure transducer located 2.75 in behind the center of the test sample (72).

Several filler materials were considered encompassing a wide variety of physical characteristics. These included the granular/porous solid fillers CAB-O-SIL®, aerogel, expanding foam, volcanic tuff, and glass beads. Fluid fillers tested included water and glycerin. Results of the tests are provided in Table 3-1 (72).

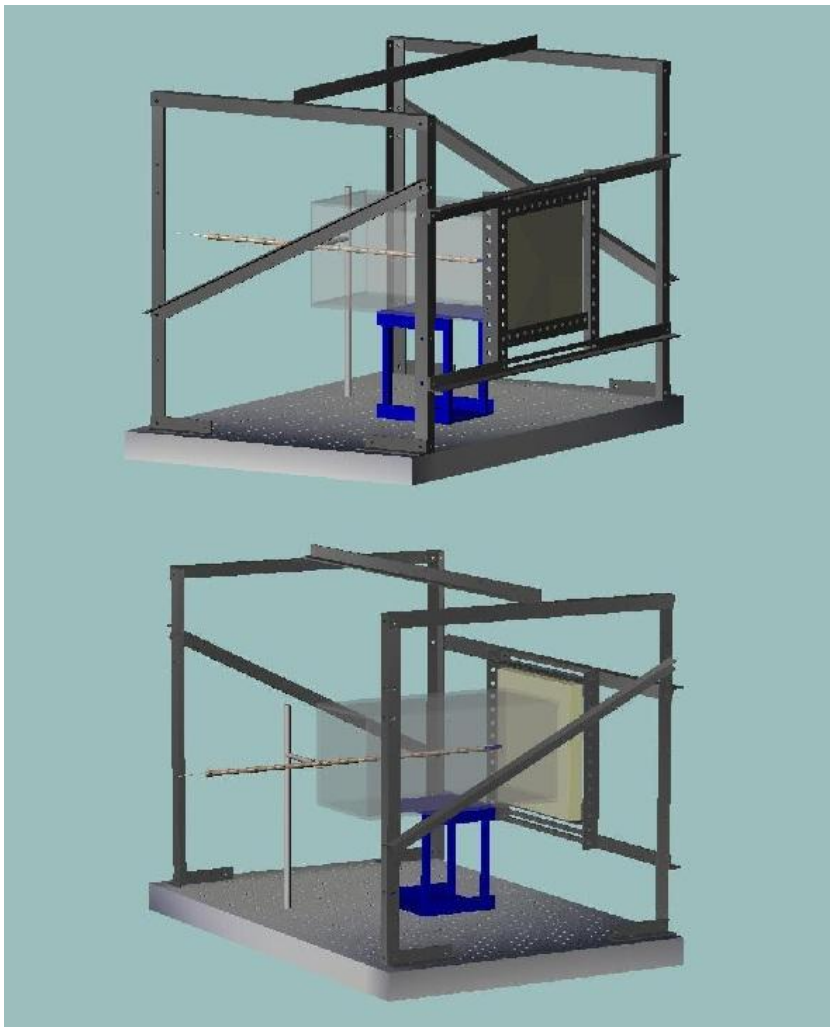

**Figure 3-6 - Setup used by Alley (72)**

| Sample | Impulse [psig-ms] | Arrival Time [ms] | Duration [ms] | Rise Time [ms] | Peak [psig] |
|---|---|---|---|---|---|
| Free-Field | 5.19 | 0.57 | 1.13 | 0.02 | 15 |
| Solid | 0.36 | 0.74 | 1.27 | 0.10 | 0.86 |
| Cabosil | 0.47 | 1.00 | 0.98 | 0.40 | 0.98 |
| Aerogel | 0.41 | 0.81 | 1.14 | 0.55 | 0.91 |
| Expanding Foam | 0.45 | 0.80 | 1.42 | 0.82 | 0.80 |
| Tuff | 0.34 | 1.26 | 1.31 | 0.57 | 0.56 |
| Glass Shot | 0.28 | 0.76 | 1.68 | 0.43 | 0.47 |
| Water | 0.38 | 0.83 | 1.53 | 0.60 | 0.57 |
| Glycerin | 0.34 | 0.86 | 1.58 | 0.43 | 0.45 |

**Table 3-1 - Results from Alley's testing of sandwich plates (72)**

Experimental results suggest the high density fillers, tuff, glass beads, water, and glycerin, provide the best mitigation levels, especially with respect to impulse and peak pressure. While water

and glycerin both performed well, there was no discernible advantage to the higher viscosity of glycerin over that of water leading to blast mitigation. All samples show high levels of blast pressure attenuation and impulse reduction; however, it should be noted that most of this attenuation was attributable to the PMMA sheets sandwiching the test samples (72).

Christou worked towards a finite element model of blast loading of these samples validated with the results of Alley (73). The model was developed using ABAQUS/CAE® and solved using the ABAQUS/Explicit® code. To maintain a distinct definition of the test sample while accommodating the large deformations in the air domain experienced during shock transmission, he used the coupled Eulerian-Lagrangian (CEL) formulation (73). In this formulation, the air domain is treated using an Eulerian formulation of the governing equations while the test sample and supporting structure are treated with the Lagrangian formulation. General contact algorithms are used to track the boundary between materials (74). More about CEL will be discussed later.

As a first step, Christou verified that the solution provided by ABAQUS® of a uniform planar shock in air reflecting normally off a rigid surface agrees with the shock jump conditions as described in section 2.2. Specifically, he found that the pressure jump, density jump, and particle and shock velocities agreed with theory. Error in these values increased with an increase in the strength of the shock, though at the shock levels tested in the project errors were around 1%. In the reflected region, particle velocities showed a substantial percentage of error, though error in absolute value was small. Overall, the results demonstrate that ABAQUS® is capable of simulating air blast scenarios (73).

Christou found instabilities in the solution surrounding the passage of the shock in the form of local oscillations of the solution near the jump. These instabilities may be treated using artificial viscosity, which allows shocks to be captured that have a width less than the mesh size. ABAQUS/Explicit® includes a linear term and a quadratic term of artificial viscosity. The linear term is linear in volumetric strain rate and is meant to dampen ringing effects. The quadratic term is quadratic in volumetric strain rate and applies only when the material is under compressive stress (74). Christou determined for these simulations that the best coefficient for the linear term is 0.2 and that for the quadratic term is 1.2 (73).

To simulate blast loading, Christou applied a decaying pressure load at one end of the air domain. The load was tuned in such a way as to agree with the experimentally measured free field pressure profile. For simplicity, Christou assumed a planar incoming wave, and symmetry boundary

conditions were imposed on lateral sides of the air domain to achieve this effect. Results were obtained for a solid foam sample as well as a sample with water as a filler material. The numerical and experimental results agreed in order of magnitude, but values did not show excellent agreement. Peak pressure for the water filler material matched well, but it was out of phase with the experimental results (73).

A likely reason for the discrepancy between Christou's model and experimental results is the very low transmitted pressures involved. Based on the sensitivity of the pressure transducers, there may have been as much as 50% discrepancy between measured results and actual results. To alleviate this issue, the experimental test setup was reconsidered. These efforts were recently described in Goel's thesis (4). Smaller test samples were used this time. Furthermore, the test samples were secured flat against an aluminum plate. Two pressure transducers were inserted into the plate with the diaphragm flush with the front face of the plate. One transducer was behind the center of the test sample, and the other was adjacent to, but not covered by, the test sample. The test setup is shown below.

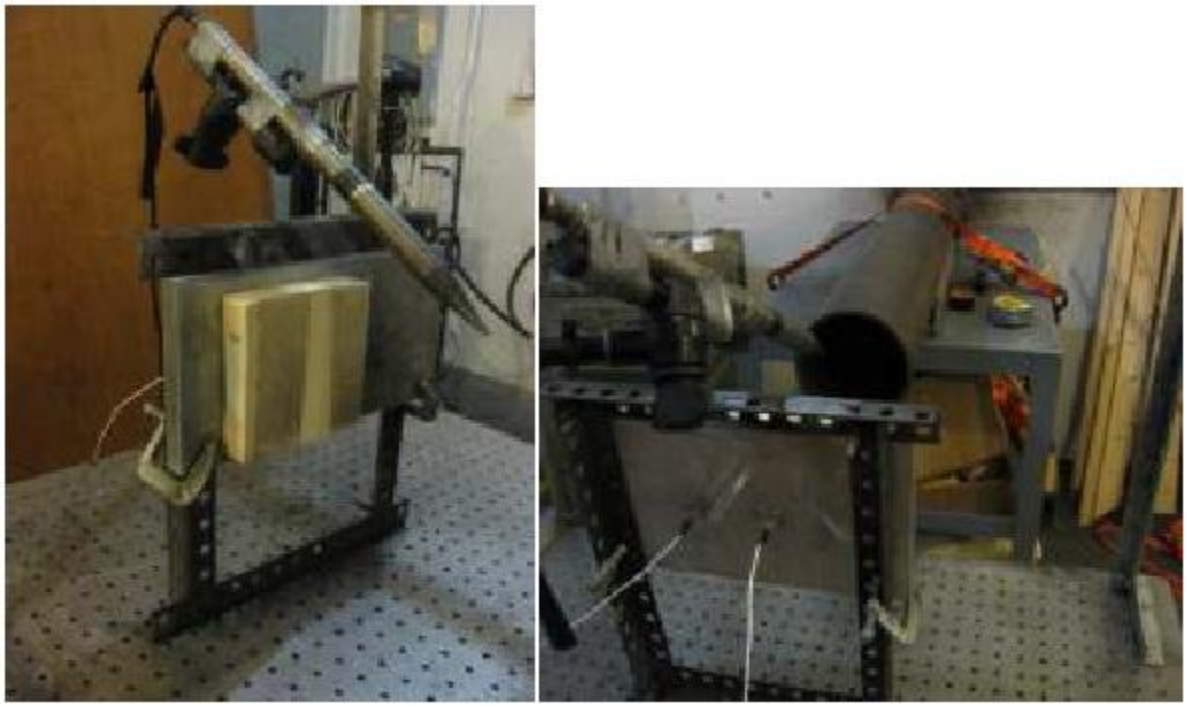

**Figure 3-7 - Modified experimental setup (4)**

Test samples for these experiments were similar to those used by Alley, only smaller. That is, samples were 5 in x 5 in by 1 in, and cavities were 5 in x 3 in x 0.5 in. Filler materials tested included

glass beads, aerogel, volcanic tuff, CAB-O-SIL®, water, glycerin, and AgileZorb™. AgileZorb™ is an advanced material containing nanoporous spheres suspended in a hydrophobic gel (www.agilenano.com). This material was blasted directly. Also, a standard pad from an Advanced Combat Helmet was blasted for comparison purposes. Peak pressures for each sample are provided below.

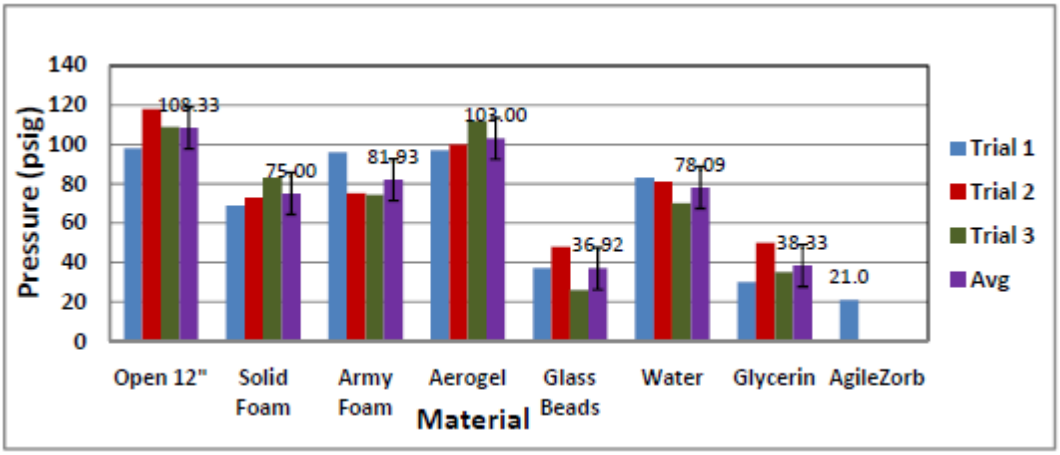


**Figure 3-8 - Results from modified testing of sandwich structures (4)**

Performance of each filler material may be assessed from Figure 3-8. With the exception of aerogel, all samples tested provide some attenuation of the peak pressure. AgileZorb™ shows the greatest reduction in peak pressure. While these results were promising, the company that makes this material was not interested in pursuing further research with this group. Glycerin and glass beads were the most promising among the remaining filler materials. Water, solid VN600 foam, and the Army pads performed roughly the same as shown here. Results also show that the rise times increase using glycerin and water fillers, a desirable effect for minimizing damage to the brain (4).

A finite element model of the new scenario was then pursued. The release of ABAQUS® v 6.10 included the ConWep (https://pdc.usace.army.mil/software/conwep/) air blast module. Given a point of detonation and equivalent mass of TNT for the explosion, the module imposes appropriate loading on structures, including dynamic pressure effects (74). The main advantage of using this module is avoiding modeling the air domain and shock propagation through it, substantially reducing the computational effort. This module rather than CEL is employed by Goel to achieve blast loading. However, for fluid filler materials, CEL is still used for the channel domain. Good agreement is found between the measured and simulated loading, as indicated in the figure below (4).

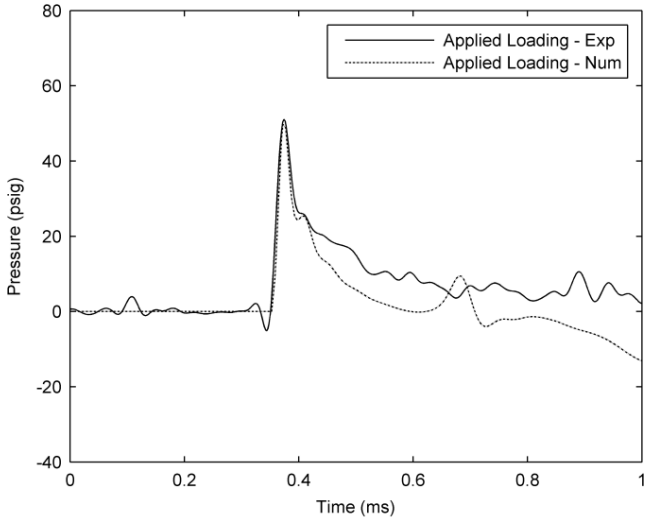


**Figure 3-9 - Comparison of experimentally measured and numerically applied loading (4)**

It is evident from the figure that use of the ConWep module captures the rise time and peak pressure of the applied loading very well and is sufficient for use in these simulations. Simulations using solid foam and other filler materials were then performed, with peak pressure used as a gauge of similarity between experiments and simulations. Very good agreement between peak pressures was found for solid foam, glass beads, and glycerin. Simulations indicated a lower peak transmitted pressure for the aerogel filler material, while the same was not true experimentally. A plausible explanation for this discrepancy is the lack of an accurate material model for aerogel, which is largely composed of air and is very compressible. Discrepancy in the results with water as a filler material are not easily explained. The simulations predict water to perform very similarly to glycerin, though experimentally glycerin looks better than water (4).

After having a validated finite element model, Goel pursued parametric and sensitivity analyses. He varied viscosity of a fluid filler material over several orders of magnitude. Results from these simulations indicate that for the blast problem, viscosity does not play a role like it did in impact experiments. He verified this property by simulating impacts on similar samples and demonstrating that viscosity does affect those results. He also looked into varying the channel geometry, including multiple round channels as well as interconnected channels. The results suggest that the configuration of the channels does not matter as much as the amount of filler material present. That is, blast mitigation may be more of an inertial effect than anything (4).

# Chapter 4 Material Characterization

In order to perform numerical simulations, accurate material models are required to describe air, VN600, and all filler materials involved. The material models used are described below.

## 4.1 Fluid Materials

The fluid materials for this study, air, water, and glycerin, are described using equations of state describing the hydrodynamic behavior of the materials. That is, they are described by constitutive equations defining the pressure of the material as a function of the density and internal energy (74). Deviatoric behavior for these materials is modeled using Newtonian viscosity. This model assumes the deviatoric and volumetric responses are uncoupled. Deviatoric stress is related to the deviatoric strain rate and engineering shear strain rate as given below.

$$\vec{S} = 2\eta\dot{\vec{e}} = \eta\dot{\vec{\gamma}}$$

**Equation 4-1**

Here, $\vec{S}$ is the deviatoric stress, $\dot{\vec{e}}$ is the deviatoric part of the strain rate, $\eta$ is the viscosity of the fluid, and $\dot{\vec{\gamma}}$ is the engineering shear strain rate (74). In general, viscosity is a function of temperature. However, in this project it is assumed the dynamics of the problem are fast enough to ignore this temperature dependence.

### 4.1.1 Air

The model applied to air is the ideal gas law. This was mentioned in Section 2.2, but is revisited here to point out some properties required by ABAQUS®. Pressure, density, and temperature of an ideal gas are related as follows.

$$p + p_A = \rho R\left(\vartheta - \vartheta^Z\right)$$

**Equation 4-2**

Here, $p$ is the gauge pressure, $p_A$ is atmospheric pressure, $\rho$ is the density, $R$ is the gas constant, $\vartheta$ is the temperature, and $\vartheta^Z$ is the absolute zero on the temperature scale being used. An important feature of an ideal gas is that the specific energy depends only on the temperature, which is given below.

$$E_m = E_{m0} + \int_{\vartheta_0 - \vartheta^Z}^{\vartheta - \vartheta^Z} c_v(T)dT$$

**Equation 4-3**

Here, $E_{m0}$ is the initial specific energy at the initial temperature $\vartheta_0$ and $c_v$ is the constant volume specific heat, which is only a function of temperature for an ideal gas (74). The gas constant may be calculated by dividing the universal gas constant by the molecular weight of the gas under consideration. Furthermore, for an ideal gas, $R = c_p - c_v$ where $c_p$ is the constant pressure specific heat (74). Two of the quantities temperature, pressure, and density needs to be specified to fully define the initial state of the gas.

For this project, time scales of compression of the air are very small, and it assumed the analysis is adiabatic and that air has a constant specific heat. Calculation of the specific energy Equation 4-3 is simplified greatly.

$$E_m = c_v\left(\vartheta - \vartheta^Z\right)$$

**Equation 4-4**

The ideal gas equation of state may then be recast in the form given here, the same relation given by Equation 2-3.

$$p + p_A = (\gamma - 1)\rho E_m$$

**Equation 4-5**

Properties used for air in this project are given in the table below.

| | |
|---|---|
| $\rho$ | 1.208 kg/cu m |
| $\vartheta^Z$ | -273.15 deg C |
| $\gamma$ | 1.4 |
| $c_v$ | 718.16 J/kg-K |
| $p_A$ | 101325 Pa |
| $\eta$ | 1.83E-5 kg/m-s |

**Table 4-1 - Air Properties**

### 4.1.2 Water and Glycerin

For modeling viscous, incompressible fluids governed by the Navier-Stokes equations of flow, ABAQUS® suggests use of the linear $U_S - U_p$ equation of state model (74). The equation of state describes the volumetric response, with the bulk modulus acting as a penalty parameter for the incompressible constraint (74).

Water and glycerin are modeled using the Mie-Grüneisen equation of state, which is linear in energy. The form used here is given below.

$$p - p_H = \Gamma\rho\left(E_m - E_H\right)$$

**Equation 4-6**

The subscript $H$ stands for the so-called Hugoniot properties, and $\Gamma$ is the Grüneisen ratio. The Grüneisen parameter is defined by a material constant $\Gamma_0$ and reference density $\rho_0$ as given below.

$$\Gamma = \Gamma_0 \frac{\rho_0}{\rho}$$

**Equation 4-7**

The Hugoniot energy is related to the Hugoniot pressure as given below.

$$E_H = \frac{p_H \eta}{2\rho_0}$$

**Equation 4-8**

The quantity $\eta = 1 - \rho_0/\rho$ is the nominal volumetric compressive strain. Plugging Equation 4-7 and Equation 4-8 into Equation 4-6 yields an expression for pressure as a function of density and specific energy.

$$p = p_H\left(1 - \frac{\Gamma_0\eta}{2}\right) + \Gamma_0\rho_0 E_m$$

**Equation 4-9**

Equation 4-9 and the energy equation form a coupled system that is solved by ABAQUS/Explicit® at simultaneously at each material point (74).

It remains to determine an expression for the Hugoniot pressure. It has been shown that a linear Hugoniot model relating the shock velocity $U_S$ and particle velocity $U_p$ represents the shock response of a wide variety of materials well (26). This relationship is expressed as follows.

$$U_S = c_0 + sU_p$$

**Equation 4-10**

A common fit to Hugoniot data of pressure and density is given below, parameterize by the same variables as in Equation 4-10.

$$p_H = \frac{\rho_0 c_0^2 \eta}{(1 - s\eta)^2}$$

**Equation 4-11**

The quantity $\rho_0 c_0^2$ is equivalent to the elastic bulk modulus of the material at small nominal strains, connecting the use of this relation to model fluids (74). The expression for the Hugoniot pressure suggests a limit for density in tension, below which negative sound speeds are calculated for the material (74).

$$\rho_{\lim} = \frac{s\rho_0}{s - 1}$$

**Equation 4-12**

In the absence of other specific initial conditions, ABAQUS/Explicit® assumes the material is at the reference state, $E_m = 0$, $p = 0$, and $\rho = \rho_0$ (74). Parameters used for water and glycerin are provided below.

| | | Water | Glycerin |
|---|---|---|---|
| $\rho_0$ | kg/cu m | 1000 | 1260 |
| $s$ | | 1.92 | 1.60 |
| $c_0$ | m/s | 1490 | 1900 |
| $\Gamma_0$ | | 0.1 | 0.78 |
| $\eta$ | kg/m-s | 0.001 | 1.500 |

**Table 4-2 - Parameters used for fluid filler materials**

## 4.2 Solid Materials

Unlike fluids, which are all treated using an equation of state, each solid is modeled using its own stress-strain/strain-rate relation.

### 4.2.1 VN600 Foam

VN600 is a closed-cell elastomeric foam provided by Der-Tex Corporation. The solid phase of the foam is constructed of vinyl nitrile. The typical compressive stress-strain curve for an elastomeric foam is given below.

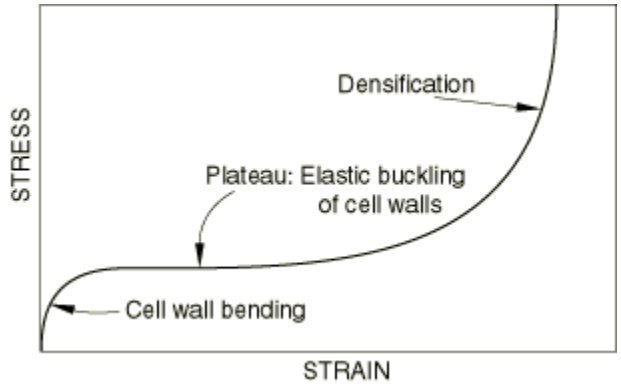


**Figure 4-1 - Compressive stress-strain curve for an elastomeric foam (74)**

There are three main phases of compressive deformation of the foam. Initially, the foam deforms in a linear elastic manner. Deformation is controlled by cell-wall bending and, for closed-cell foams, by cell face stretching (39). Often an elastic modulus $E^*$ coinciding with the initial slope of the stress strain curve is defined. During the second phase, the stress-strain relationship plateaus where there is little stress increase for a large increase in strain. Compression during this phase causes elastic buckling in the cell walls. In closed cell foams, the pressure of the entrapped gas and membrane stretching increase the level and slope of the plateau (74). Eventually, the cells have almost completely collapsed and opposite cell walls touch and the solid phase itself is compressed. This causes a rapid stress increase in a process labeled densification (74)(39). A typical tensile stress-strain curve for elastomeric foams is shown below.

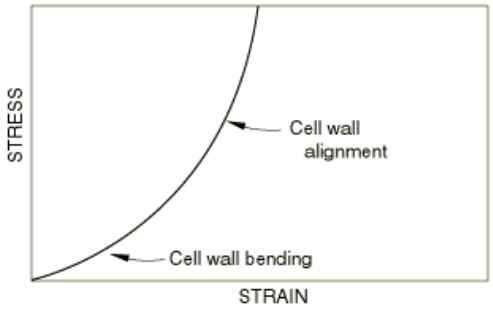


**Figure 4-2 - Tensile stress-strain curve for elastomeric foam (74)**

As in compression, the first stage of tension is a linear elastic region caused by cell wall bending and, for closed cell foams, stretching of cell faces. At large strains, cell edges are rotated towards the tensile axis, increasing the stiffness of the structure (74)(39).

The linear elastic deformation phase of an isotropic elastomeric foam is generally characterized by two moduli, usually chosen from the Young's modulus $E^*$, shear modulus $G^*$, bulk modulus $K^*$, and Poisson's ratio $\upsilon^*$ (39). Gibson and Ashby relate these quantities to the elastic modulus of the solid material composing the cell faces and edges $E_S$ and relative density $\rho^*/\rho_S$. For a closed cell elastomeric foam, comparison with test data indicate moduli are adequately described as follows (39).

$$\begin{aligned}
\frac{E^*}{E_S} &\approx \phi^2\left(\frac{\rho^*}{\rho_S}\right)+(1-\phi)\frac{\rho^*}{\rho_S}+\frac{p_0(1-2\upsilon^*)}{E_S(1-\rho^*/\rho_S)} \\
\frac{G^*}{E_S} &\approx \frac{3}{8}\left\{\phi^2\left(\frac{\rho^*}{\rho_S}\right)^2+(1-\phi)\frac{\rho^*}{\rho_S}\right\} \\
\upsilon^* &\approx \frac{1}{3}
\end{aligned}$$

**Equation 4-13**

Other quantities included in Equation 4-13 are the fraction of the solid material in the foam contained in the cell edges $\phi$ and the initial pressure of the pore gas $p_0$ (39). Generally the linear elastic region for these materials exists for small strains, e.g. less than 5%. Compression beyond this point is still fully recoverable and, consequently, elastic. However, the response is nonlinear past the elastic collapse stress $\sigma_{el}^*$ (39). A stress-strain ($\sigma^* - \varepsilon$) relation describing the behavior of a closed cell foam including gas pressure contributions during this plateau stage is given below (39).

$$\frac{\sigma^*}{E_S} = 0.05\left(\frac{\rho^*}{\rho_S}\right)^2 + \frac{p_0\varepsilon}{E_S\left(1-\varepsilon-\rho^*/\rho_S\right)}$$

**Equation 4-14**

An expression for the elastic collapse stress is provided as well (39).

$$\begin{aligned}\frac{\sigma_{el}^*}{E_S} &\approx 0.05\left(\frac{\rho^*}{\rho_S}\right)^2 + \frac{p_0 - p_{at}}{E_S} \\ \frac{\sigma_{el}^*}{E_S} &\approx 0.03\left(\frac{\rho^*}{\rho_S}\right)^2\left(1+\left(\frac{\rho^*}{\rho_S}\right)^{1/2}\right)^2 + \frac{p_0 - p_{at}}{E_S}\end{aligned}$$

**Equation 4-15**

These expressions include a correction for the difference between the initial pore gas pressure and atmospheric pressure $p_{at}$. Both expressions are for closed cell foams, and the second includes a density correction (39). After a limiting strain $\varepsilon_D$, opposite cell walls touch and are compressed. At this point the slope of the stress-strain curve approaches $E_S$, which is so much larger than $E^*$ that the curve appears vertical. Experimental data suggest that the limiting strain may be estimated as follows (39).

$$\varepsilon_D = 1 - 1.4\frac{\rho^*}{\rho_S}$$

**Equation 4-16**

Use of the relations presented here requires knowledge of the mechanical properties of the solid material composing the cell walls and edges. While other properties of the bulk foam material were provided by the manufacturer, none of those required here were available.

For the blast problem at hand, it is required to understand the behavior of VN600 under high strain rates. Christou performed low strain rate (~1%/s) uniaxial and volumetric compression tests and used scaling arguments to estimate the stress-strain relationship at high strain rates (73). For this work, a different approach was taken to directly measure the behavior of VN600 at high strain rates. One way of performing high strain rate uniaxial compression tests on materials is to use a Split-Hopkinson Pressure Bar (SHPB) (75). The essence of the test is to suspend a sample of test material between two bars. A compressive wave is transmitted via one bar to the sample. Some of the wave is reflected, and

some is transmitted. Strain gauges on each bar record the behavior of the bars contingent on the sample properties. Dr. Simona Socrate performed SHPB testing on VN600 foam at strain rates of 1500/s and 1000/s. Because of how soft VN600 is, she used a nontraditional approach for gathering data, stitching together results of multiple passes of the compressive wave through the sample.

Using the results of the SHPB test results as well as the results from Christou's low strain rate testing, Dr. Socrate developed and validated a material model in ABAQUS®. The nonlinear elasticity of the foam is described using a hyperelastic model with the Marlow strain energy potential. The uniaxial SHPB compression testing at the 1500/s strain rate is used to provide the instantaneous deviatoric response of the material. This data can be found in (4). The volumetric response is captured by defining a Poisson's ratio of 0.25. Strain-rate dependence of the materials is achieved by including a time-domain viscoelastic model wherein coefficients in a Prony series are directly specified. Those parameters are given below.

| | g_i Prony | k_i Prony | tau_i Prony |
|---|---|---|---|
| 1 | 0.6 | 0.6 | 0.001 |
| 2 | 0.22 | 0.22 | 1 |
| 3 | 0.11 | 0.11 | 10 |

**Table 4-3 - Coefficients in the viscoelastic Prony series for VN600**

In addition, the density of the foam had been previously determined to be 108 kg/cu m (73). Predictions of this material model at various strain rates along with comparisons to experimental data are provided in Figure 4-3. The predictions agree well with both the SHPB tests and the low strain rate tests. No intermediate rate data were available for comparison, but it was expected that strain rates experienced in simulations would be near the high end.

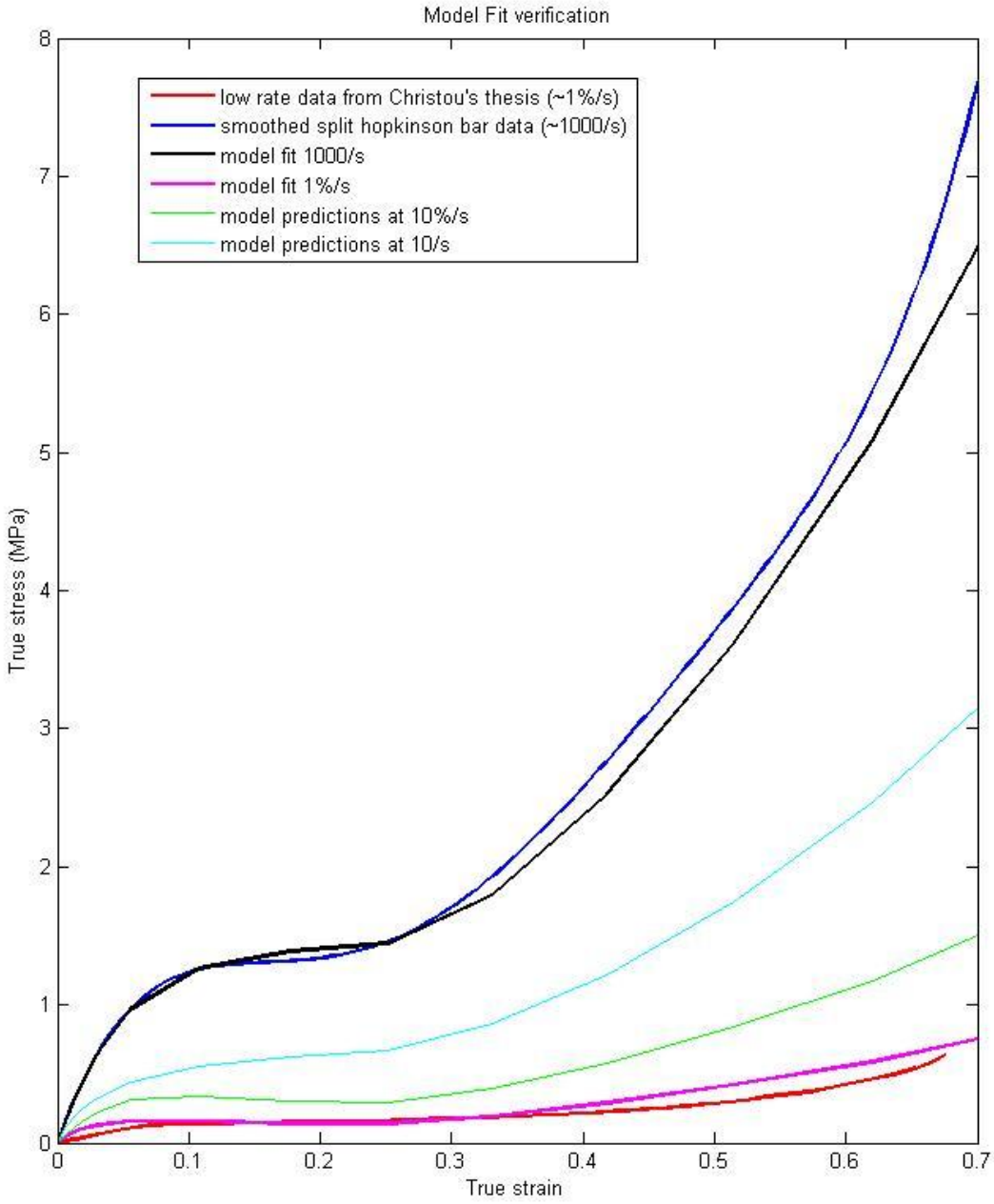


**Figure 4-3 - Comparison of the model predictions and experimental results**

### 4.2.2 Advanced Combat Helmet

The ACH shell is a composite material constructed of layers of aramid fibers combined with a matrix material. Because it is constructed of a fiber-reinforced composite, the shell experiences anisotropic strength properties and is most likely complicated to fully describe. In fact, characterization

of the mechanical response of the ACH shell material is a topic of current research. For the work presented here, the approach used by Nyein et. al. (19) investigated the response of the ACH to blast loading is followed. The helmet shell and ACH pads are modeled using hyperelasticity with a neo-Hookean strain energy potential. Parameters used to define the helmet model are provided below (19).

| Material | Density | Young's Modulus | Poisson's Ratio |
|---|---|---|---|
| | kg/cu m | Pa | |
| Shell | 1440 | 1.24E9 | 0.36 |
| Pads | 136 | 8.00E+06 | 0.2 |

**Table 4-4 - Parameters used for the ACH helmet**

### 4.2.3 Glass Beads

A filler material of primary interest for this project is glass beads. For testing, glass beads of mesh size 40-60 from McMaster-Carr® (part number 3398K11 or 3386K71) were used. These are spherical beads having nominal diameters ranging from 0.0098 in - 0.0165 in (76). The measured density of the glass beads (as a granular material as opposed to each individual glass bead) is 1460 kg/m$^3$. There are a couple of different approaches to treating the response of such granular materials to loading. One approach is to model the dynamics and interactions of each individual particle within the granular material. This approach is broadly known as the discrete element method (DEM). Several open source and commercial codes are available implementing this method as well as interfaces for coupling it with other codes (see for example LAMMPS at http://lammps.sandia.gov/). In many situations of interest, the scale of the system is much larger than the scale of the individual particles, and it becomes impractical to model the dynamics of each individual particle.

To improve the efficiency of these models involving multiscale phenomena, it is desirable to have a continuum representation of granular materials in the form of a constitutive model. An example of such a relationship for the incremental elastoplastic effective stress-strain response for hydrostatic compression of cohesionless soils is provided by Pestana and Whittle (77).

$$d\varepsilon = n\left[\frac{\delta_b^{\theta}}{C_b\left(\sigma'/p_a\right)^{1/3}} + \frac{\rho_c}{\left(\sigma'/p_a\right)}\left(1-\delta_b^{\theta}\right)\right]\frac{d\sigma'}{p_a}$$

**Equation 4-17**

Here, $\sigma'$ is the mean effective stress, $\varepsilon$ is the natural volumetric strain, $e$ is the current void ratio, $p_a$ is an arbitrary reference stress, $n$ is the current porosity, $C_b$ is a constant to be determined experimentally, $\rho_c$ is the slope of the Limiting Compression Curve (LCC) in $\log e - \log \sigma'$ space, $\theta$ is a positive constant exponent, and $\delta_b$ is the dimensionless distance between the current mean effective stress and the equivalent LCC stress at the same void ratio (77). Parameters in this expression can be determined through one-dimensional or hydrostatic compression testing. In a different modeling analysis, Humrickhouse explores several hyperelastic models developed for granular materials, specifically for application in nuclear safety analysis (78). Testing of these models was achieved by implementing a user material routine in ABAQUS®. He found that while hyperelastic models are intended to capture a "well-known" behavior of the dependence of the elastic moduli of granular materials on the square root of the pressure in the material, they suffer similar short-comings to a much simpler linear elastic model. In fact, his findings suggest that linear elasticity is often an appropriate choice of constitutive model for granular materials (78).

Because mechanical properties were not immediately available for the glass beads used in this project, it was necessary to perform mechanical testing. To this end, consolidation (or confined compression) tests were performed in the Soils Lab in the Department of Civil and Environmental Engineering at MIT with the help of Dr. Jack Germaine and Prof. Andrew Whittle. The set-up for these tests is shown below.

**Figure 4-4 - Consolidation Test Set-up**

Test samples were 2.053 cm tall and 6.32 cm in diameter. Different initial densities of the materials were achieved by included water with the material, though it was found that an extremely limited range of densities (1.487 g/cm$^3$ - 1.599 g/cm$^3$) was realizable. Samples were loaded to 5.09 MPa, then completely unloaded, then reloaded and unloaded again. The strain rate of loading was 5.08x10$^{-3}$ mm/s. Results for these tests are provided below.

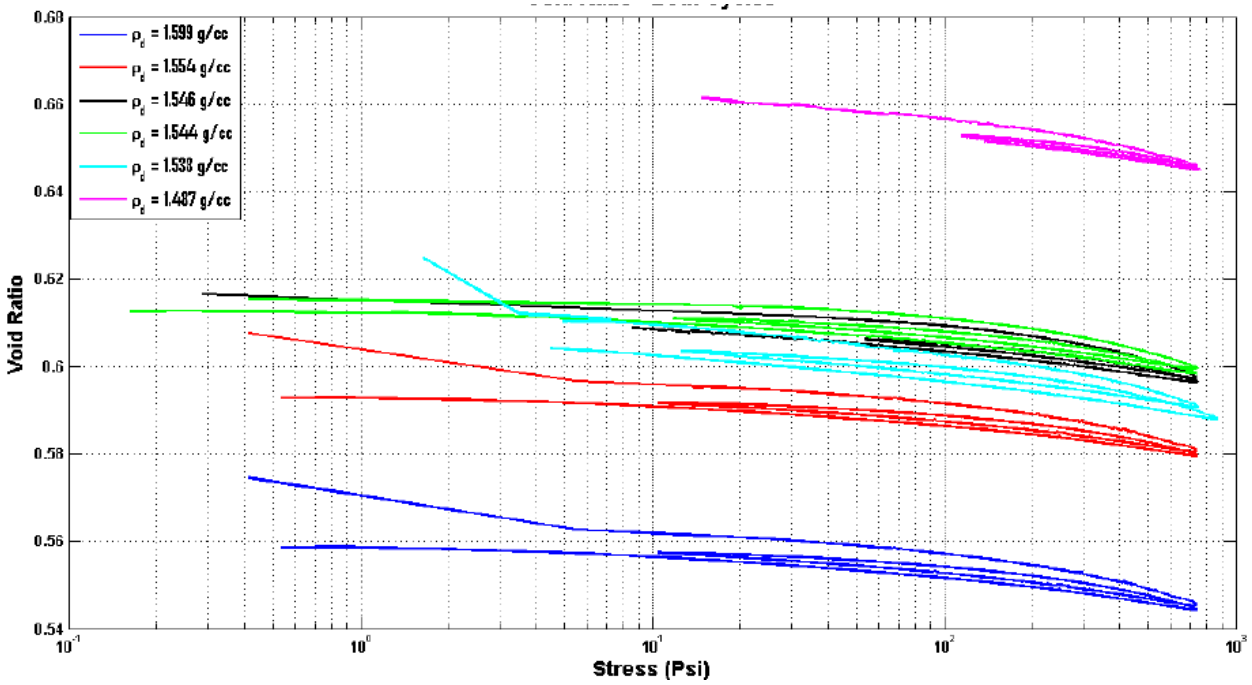


**Figure 4-5 - Consolidation Test Results**

The most representative curve of the state of the material for experimental blast testing is that for initial density of 1.487 g/cm$^3$, and this curve is used in further determination of glass beads material properties.

Following the recommendation of Humrickhouse, a linear elastic model for glass beads will be assumed. For the testing performed for this project, it is not anticipated that the stress in the glass beads will exceed 500 kPa (compared to the ~5 MPa achieved during consolidation tests). The vertical stress-vertical strain curve up to 500 kPa for the first loading of glass beads is given in Figure 4-6. The slope of the fitted line in the figure is 2.095x10$^8$ Pa, and this represents the constrained modulus $D$. The constrained modulus is related to the elastic modulus $E$ and Poisson's ratio $\upsilon$ as given here (79).

$$D = \frac{E(1-\upsilon)}{(1+\upsilon)(1-2\upsilon)}$$

**Equation 4-18**

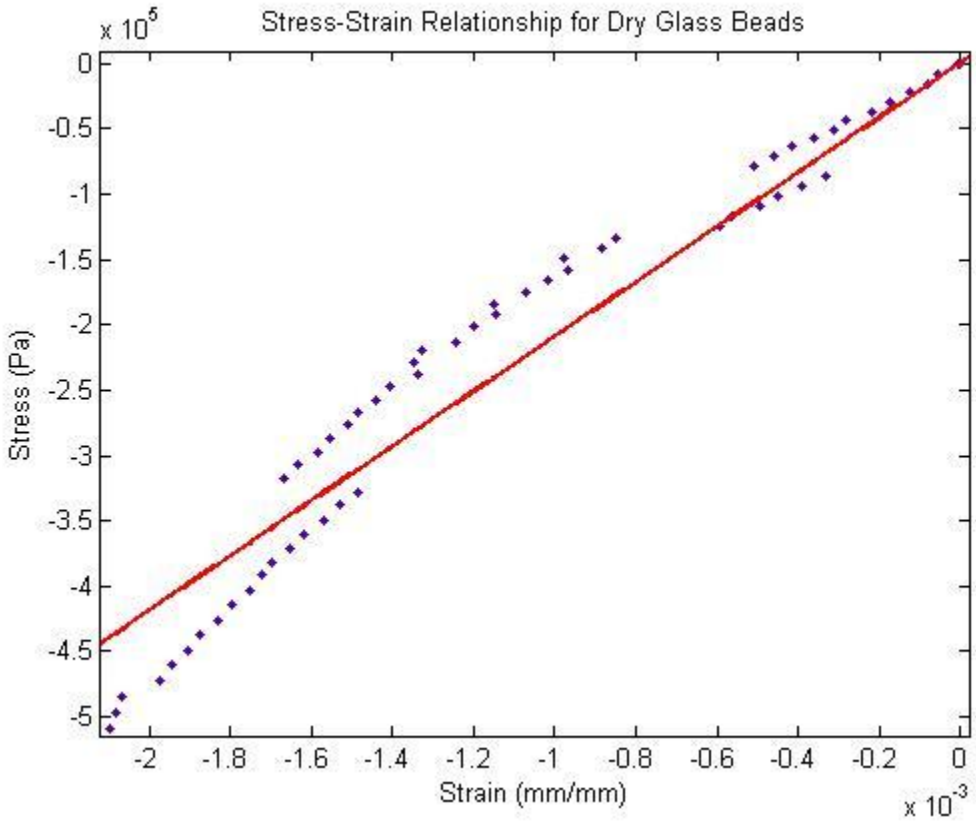


**Figure 4-6 - Dry glass beads stress-strain data and fit**

For modeling linear elasticity in ABAQUS®, it is required to input the elastic modulus and Poisson's ratio. Here, a Poisson's ratio of 0.3 is assumed (80). Given this Poisson's ratio and the experimentally determined constrained modulus, the elastic modulus according to Equation 4-18 is $1.5563 \times 10^8$ Pa. As a point of verification, the constrained compression test was simulated in ABAQUS® using this material model. The mesh and set-up for the simulation is shown in Figure 4-7. The bottom boundary is constrained to zero displacement in the Y-direction. The circumference of the sample is constrained to zero displacement in the X- and Z-directions. The top face is displaced in the negative Y-direction, consistent with the experimental procedure. Figure 4-8 shows the vertical stress-vertical strain relationship predicted during the simulation. Comparing these results with Figure 4-6, one can see agreement between these model parameters and those obtained through experimental data analysis.

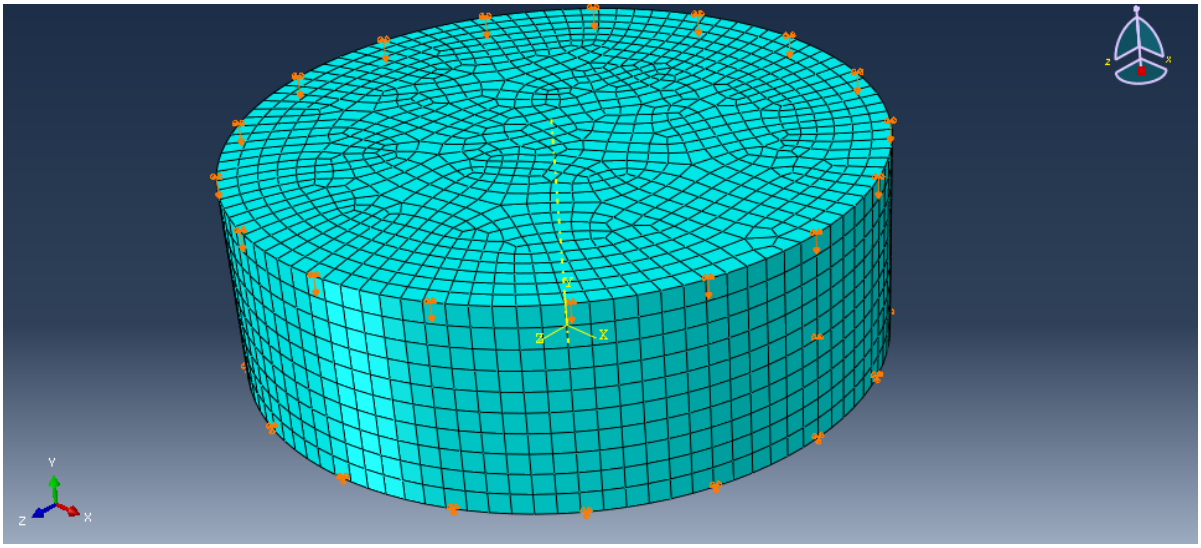

**Figure 4-7 - Mesh and set-up for consolidation simulation**

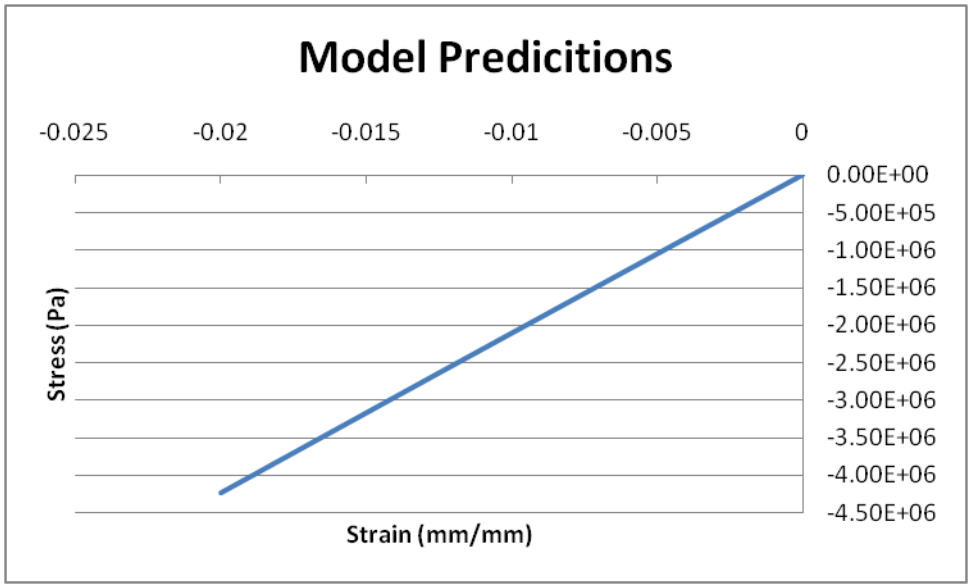


**Figure 4-8 - Abaqus model predictions for the consolidation test**

### 4.2.4 PMMA

Two different relations are required for modeling PMMA, properties of which are taken from literature. The initialization step of the numerical model uses a linear elastic model, while the blast step uses the Mie-Grüneisen equation of state. Parameters for the equation of state are available in (81). Parameters for the linear elastic model were estimated based values found on the internet, for example (82). Shear behavior was introduced through linear elastic strain modulus.

| | | |
|---|---|---|
| $\rho_0$ | kg/cu m | 1180 |
| $s$ | | 1.82 |
| $c_0$ | m/s | 2260 |
| $\Gamma_0$ | | 0.75 |
| G | GPa | 1.148 |
| E | GPa | 2.2 |
| v | | 0.39 |

**Table 4-5 - Material parameters used for PMMA**

### 4.2.5 Aerogel

Aerogel is modeled using the Mie-Grüneisen equation of state as well. Shear behavior was again treated with a linear elastic shear modulus. Properties used for aerogel are provided below (4).

| | | |
|---|---|---|
| $\rho_0$ | kg/cu m | 95 |
| $s$ | | 1.08 |
| $c_0$ | m/s | 567 |
| G | MPa | 4.17 |

**Figure 4-9 - Material parameters used for aerogel**

# Chapter 5 Blast Experiments

Blast tests were performed on the first prototype of a liner including the technology discussed here. Tests were performed on the standard helmet pad included with the ACH as well as liners constructed of Der-Tex with channels for filler materials. Filler materials tested included glass beads, aerogel, water, and (pure) glycerin. In this chapter, the experiments are discussed, and the results obtained are presented.

## 5.1 First Helmet Liner Prototype

The purpose of this project is to introduce additional functionality (i.e. blast protection) to the liner of the ACH. Figure 5-1 below shows the outer shell of the ACH (purchased from GENTEX® Corporation, Simpson, PA, USA). Figure 5-2 below shows the standard set of helmet pads that are included with the ACH. Other pad sets may be purchased for the helmet. Furthermore, attachments (i.e. night vision goggles, cameras, etc.) and coverings are frequently added to the outside of the helmet shell as well.

**Figure 5-1 - The Advanced Combat Helmet**

**Figure 5-2 - Standard ACH liner pad configuration**

Figure 5-3 shows the first prototype of an ACH helmet liner incorporating the relevant technology from this research.

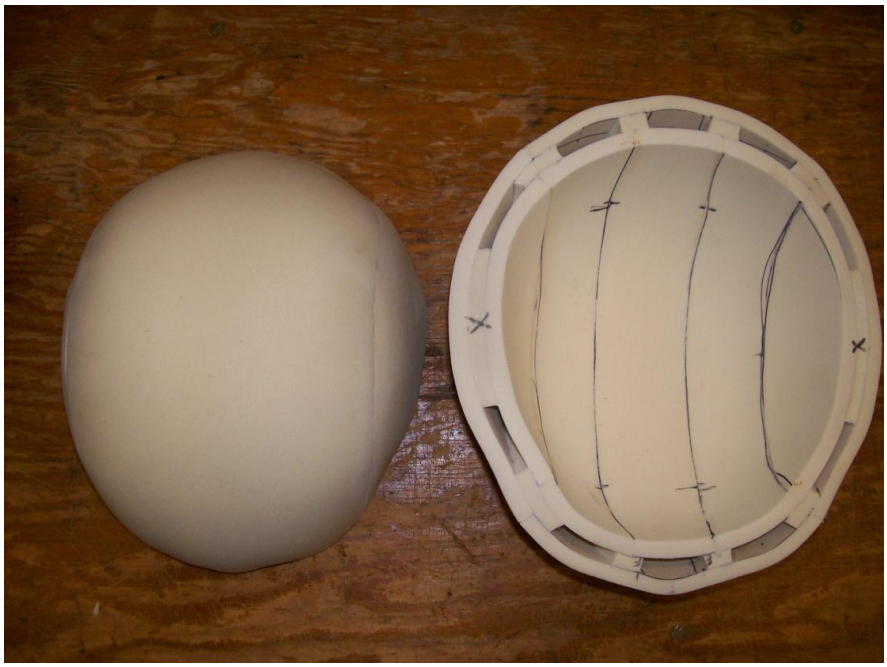

**Figure 5-3 - Top and bottom views of the first prototype liner**

The prototype is constructed essentially of three 0.25" thick layers of Der-Tex foam. The outermost layer, which contacts the helmet shell, is a solid layer constructed of three cuts of foam. Pieces of foam are attached using 3M® Hi-Strength 90 Spray Adhesive, which was found to provide sufficient bonding strengths while not chemically reacting with the foam in an adverse way. The second layer in the liner defines the channel geometry. There are five parallel channels each 3 cm wide. Finally, the last layer is composed of five cuts of foam provided a sealing cover to each individual channel.

There are a few important issues to mention regarding this prototype. First, this is only a first prototype meant to provide initial insight into the performance of such liners as well as a basis for comparison of numerical modeling. It may or may not suggest the optimally designed liner. Secondly, the quality of the constructed prototypes depends largely on the skills of the person manufacturing them. To construct these liners in a commercial fashion using specially designed molds would be prohibitive in both time and cost at this stage in the project. Finally, this prototype is one single liner covering the entire inside of the helmet compared to the modular design of the standard pads for the ACH. This is mainly for simplicity of design for an initial prototype. The optimal design for a liner may, in

fact, resemble the current modular design. The figure below shows the newly designed liner installed in the ACH shell.

**Figure 5-4 - The prototype liner installed in the ACH shell**

Another interesting consideration for this initial prototype is the weight comparison between the ACH with the standard pads and the ACH with the new liner filled with various filler materials. This comparison is provided below.

| S. No. | Material | Weight (g) | % Difference wrt Army Pads | % Difference wrt helmet* |
|---|---|---|---|---|
| 1 | Liner made of Der-Tex Foam | 150 | 56 | 3.9 |
| 2 | Liner with cavities in Der-Tex Foam | 127.5 | 34 | 2.3 |
| 3 | Army Foam Pads | 96 | - | - |
| 4 | Glass Beads in (2) | 443 | 361 | 25.0 |
| 5 | Aerogel in (2) | 148 | 54 | 3.7 |
| 6 | Water in (2) | 344 | 258 | 18.0 |
| 7 | Glycerin in (2) | 400 | 316 | 22.0 |
| *Weight of Standard Size 'M' Army Helmet = 1.38 kg | | | | |

**Table 5-1 - Weight comparison (4)**

It is clear from Table 5-1 that this prototype design substantially increases the mass of the ACH. However, as mentioned before, this is only a first prototype. Optimization studies will need to be

performed to minimize the weight added by the filler materials while maintaining a sufficient level of blast mitigation.

## 5.2 Experimental Set-up

Blast experiments were performed at Purdue University with Prof. Steve Son and graduate student Ben Schimizze. A photo of the set-up is shown below.

**Figure 5-5 - Experimental Set-up**

Seen in Figure 5-5 is the explosively driven shock tube aimed at the "face" of the ACH. A photo and drawing of the shock tube assembly is provided below.

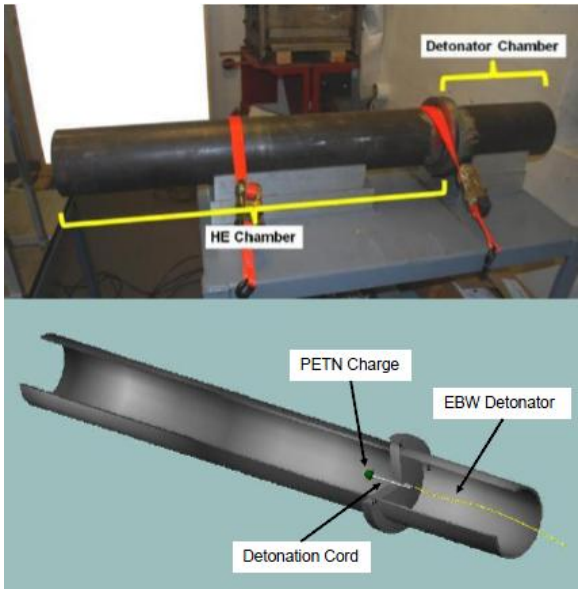


**Figure 5-6 - Explosively driven shock tube (72)**

Details of this shock tube have been discussed in detail elsewhere (72)(73)(4), but a brief review is provided here. The detonator for these experiments was a Teledyne RISI RP-502 exploding bridge wire (EBW) detonator located in the detonation chamber. Six inches of PETN detonation cord is then used to connect the detonation in the detonation chamber to the high explosive (HE) chamber, where 3 g of Primasheet 1000 by Ensign-Bickford Aerospace & Defense (EBA&D) in a spherical configuration was attached to the cord. Primasheet 1000 is a plastic explosive containing 63% PETN and has a detonation velocity around 6800 m/s. This produced an explosion with equivalent yield of 2.87 g TNT and 13.24 kJ. Within the HE chamber the shock wave is allowed to separate from the slower moving detonation products (72). For these experiments, the opening of the shock tube was centered on the closest point on the rim of the helmet and maintained at a distance of 12" away.

The helmet was supported by a PMMA hemisphere attached to a PMMA cylinder. This whole assembly was then placed inside a heavy steel pipe to hold it for experiments. This entire arrangement and orientation with respect to the shock tube is illustrated in Figure 5-7.

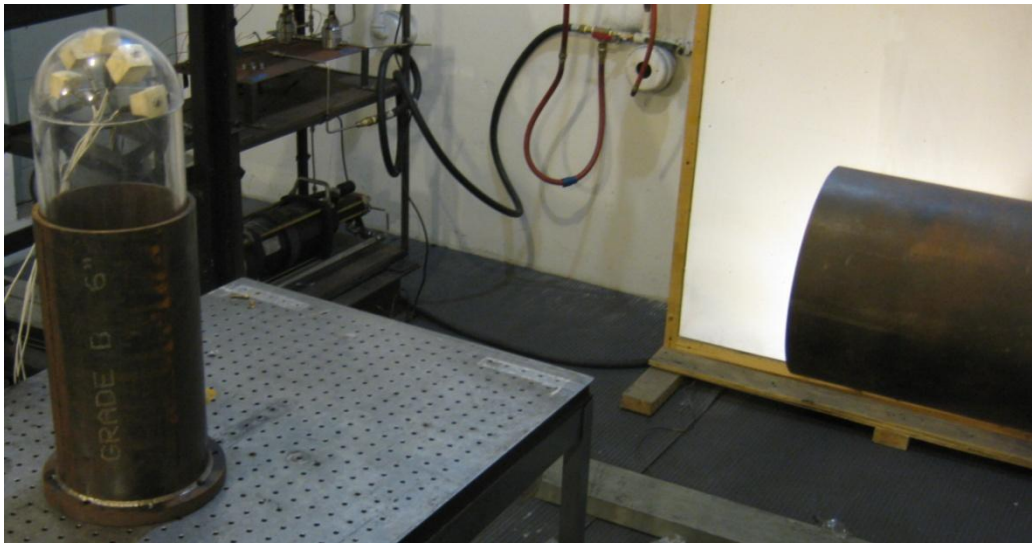


**Figure 5-7 - Support for the helmet during testing**

Also visible in Figure 5-7 are the five pressure transducers installed in the PMMA hemisphere. In this report, the gauges are labeled sequentially from 1 to 5 with gauge 1 being closest to the shock tube. These are piezoelectric pressure transducers PCB® models 113A22 and 113B22. Serial numbers and calibrations for these gauges are provided below in Table 5-2. Data from these sensors was conditioned and amplified using PCB® model 482A22 signal conditioners. Data was recorded by Tektronix® DPO4034

oscilloscopes. Finally, the data was filtered four times using the two-pass bandpass filter in DPlot® Graph Software within the 0-100kHz frequency band.

| Gauge | Serial Num. | b1 | b0 |
|---|---|---|---|
| 1 | 18623 | 0.9844 | 1.5042 |
| 2 | 19126 | 1.009 | -0.8876 |
| 3 | 19128 | 1.003 | 0.1036 |
| 4 | 17073 | 1.0095 | 0.2871 |
| 5 | 19122 | 0.9746 | 1.5629 |

**Table 5-2 - Pressure gauge details - Pressure (Pa)=1000*(Reading (V))*b1+b0**

It can also be seen from Figure 5-5 that the helmet is oriented with the channel openings pointing downwards for testing. Therefore, it was necessary to seal the channels. In previous experimental work with sandwich structures, channels were generally taped shut. It was difficult to get a sufficient seal (particularly for the fluid and glass beads filler materials) with this method. Additionally, the tape would generally have to be wrapped tightly around the test sample, leading to unknown initial stress distributions before a test even took place. Furthermore, fluid filler materials often prevented a good bond between the tape and the foam. To alleviate all of these issues for testing the liner prototypes, a new method was used to seal the channels. Each channel was filled completely with the desired filler material. Then, each channel opening was covered by using super glue to attach a small piece of Der-Tex foam over the opening. The super glue did not cause any discernible damage to the foam. Furthermore, this method seemed to provide an excellent seal to prevent leaking of any kind, even from fluid filler materials. Figure 5-8 shows these end caps applied to a test sample.

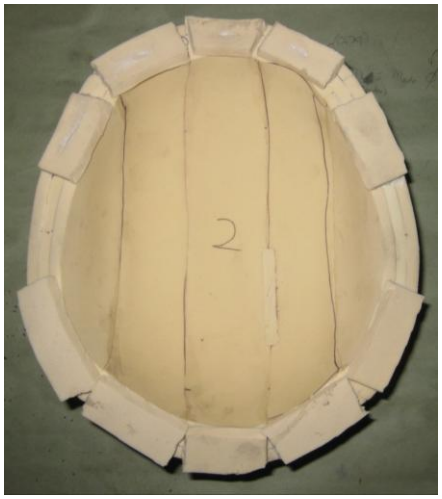


**Figure 5-8 - End caps over the channels**

## 5.3 Experimental Results and Discussion

Experiments were carried out using the standard ACH pads as well as the prototype liner filled with water, glycerin, glass beads, and aerogel. Two main comparisons of results are made here. First, a comparison between the pressure response at each of the gauges for a given trial is explored to get an idea of the spatial distribution of the pressures. Second, a comparison across different liners at each of the gauges individually is explored to compare the mitigation capabilities of the different liners. For all test results, the third gauge became saturated and data was unreliable. This data is excluded from these analyses.

### 5.3.1 Comparison By Filler Material

For each filler material, two tests were carried out. Helmet liners were not reused, but helmet shells were reused as they showed no indication of damage after the tests, nor were they anticipated to. Results for the standard ACH pads (called "Army Foam") are provided below.

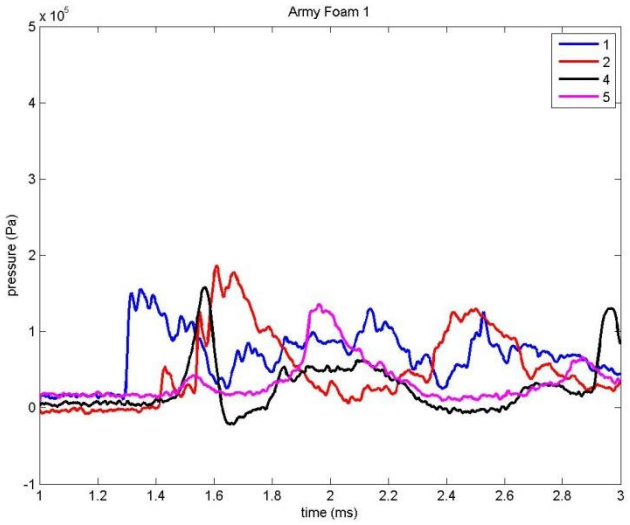


**Figure 5-9 - First ACH standard pad test**

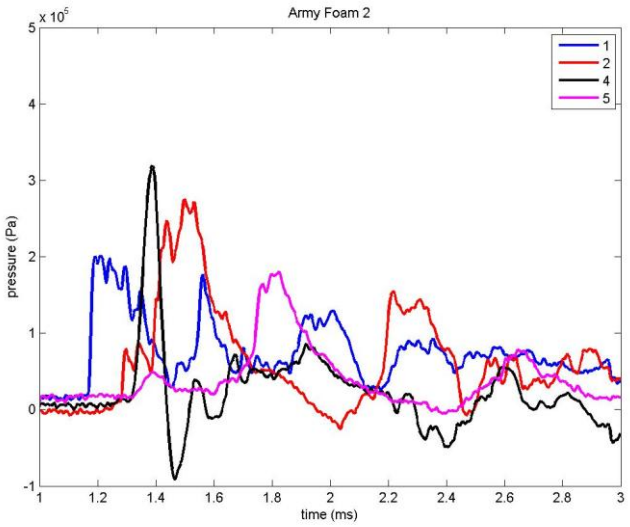


**Figure 5-10 - Second ACH standard pad test**

Qualitatively, these two results show similarities. The shapes of the waveforms are similar for gauges 1,, 2, and 5. Gauge 4 shows some greater variations in the second test compared to the first test. Peak pressure levels were greater during the second test. The peak pressure during the first test was just under 200 kPa, while that for the second test was nearly 350 kPa. It is interesting to note that the peak pressure for the fourth gauge is reached before the peak pressure for the second gauge, though it can be seen in both tests a pressure rise initiates sooner at the second gauge compared to the fourth gauge. The only "underpressure" seen is in the fourth gauge. Next, the results for glass beads are presented.

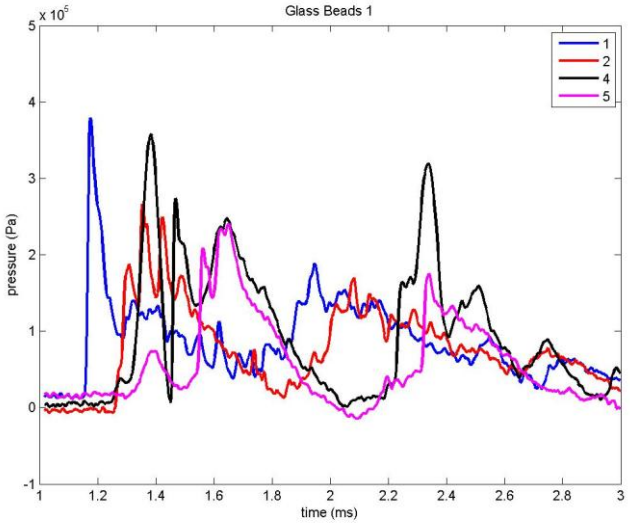


**Figure 5-11 - First glass beads test**

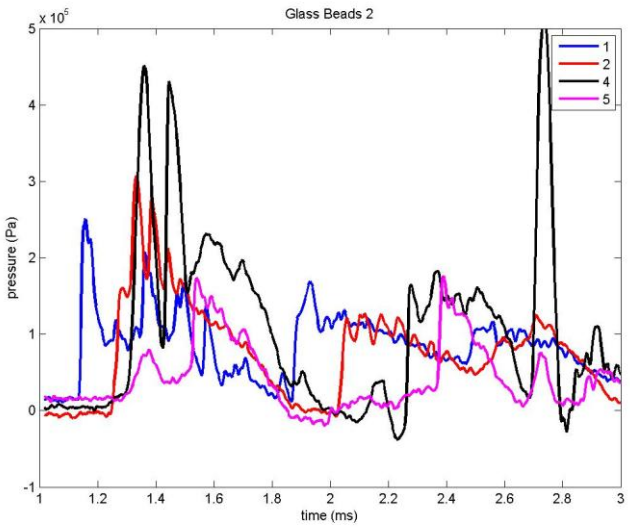


**Figure 5-12 - Second glass beads test**

Here, as with the ACH pad result, there are qualitative consistencies. The general shapes of the waveforms are similar for both tests. However, magnitudes between gauges and between tests do not match well. In the first test, the first gauge exhibits the peak pressure of about 380 kPa, gauges 2 and 5 exhibit similar peak pressures at about 275 kPa, and gauge 4 has a peak around 250 kPa. Gauges 2 and 4 reach their peaks at approximately the same time. In contrast, the highest peak pressure for test two is recorded by gauge number 4, initially about 450 kPa but also showing a later peak about 500 kPa. Also, the peak reached at gauge 2 is about 300 kPa, while that for gauge 1 is only around 250 kPa. The relative timing and oscillations after the initial peak are similar for all gauges between the two tests. The results for aerogel will be presented and discussed next.

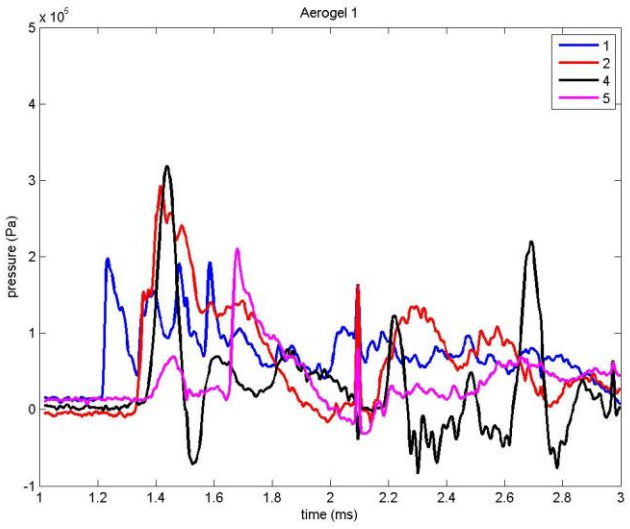


**Figure 5-13 - First aerogel test**

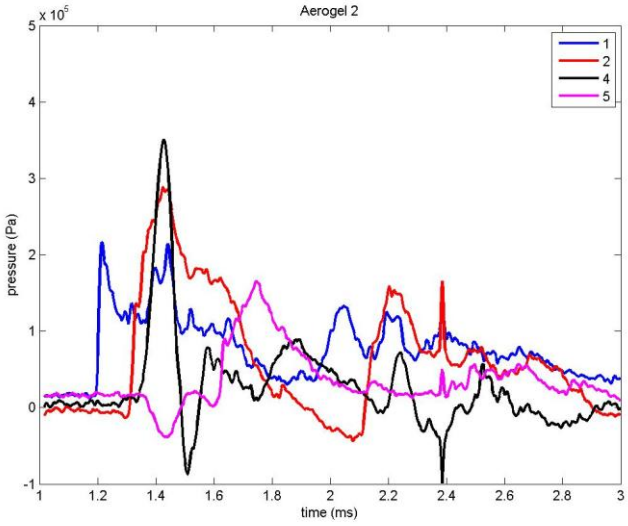


**Figure 5-14 - Second aerogel test**

Results between tests for aerogel are more consistent then the previously two considered cases. The peak pressure in both cases is obtained with gauge 4, and both are around 330 kPa. The second highest peak pressure was obtained at gauge 2 at the same time as gauge 4, in both cases just under 300 kPa. Gauges 1 and 5 recorded peak pressures around 200 kPa. Qualitatively the two tests show very similar results, particularly during the first millisecond of the blast event, leading to increased confidence in these results. Now, the results using fluid filler materials will be presented, beginning with glycerin.

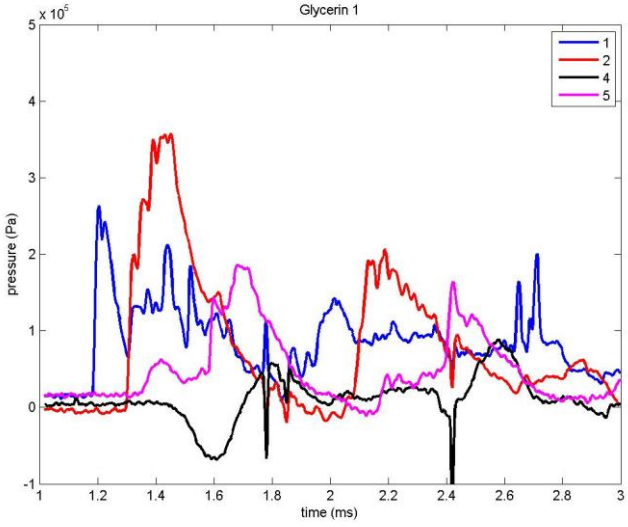


**Figure 5-15 - First glycerin test**

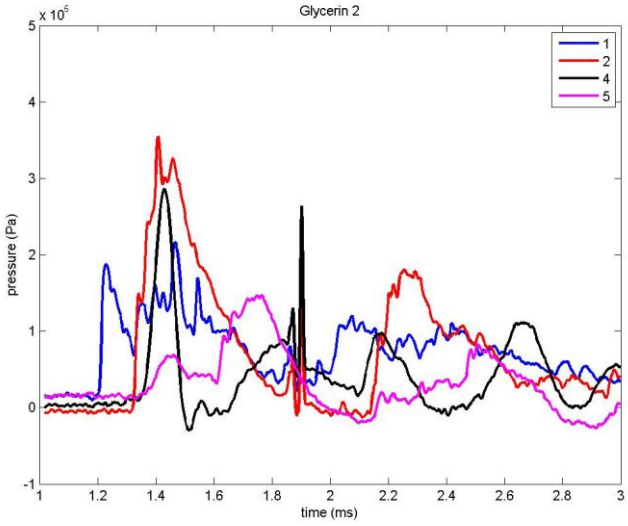


**Figure 5-16 - Second glycerin test**

As has been the case with the results presented so far, the shapes of the waveforms (except for gauge 4) are qualitatively similar between the two tests. In both tests the highest peak pressure was measured by gauge 2 at just under 400 kPa. Peak pressures for gauges 1 and 5 were 275 kPa and 200 kPa, respectively, for test 1, and 200 kPa and 150 kPa, respectively, for test 2. The response for gauge 4 was drastically different between tests. For test 1, there is no identifiable peak pressure. In fact, the first pressure change for this gauge is negative. This suggests, possibly, that the gauge became dislodged during testing. The result for gauge 4 from the second test is more in line with the previously discussed results. For this test and gauge, a peak pressure of just under 300 kPa is measured about the same time as the peak for gauge 2 is reached. Finally, the results for water will be presented.

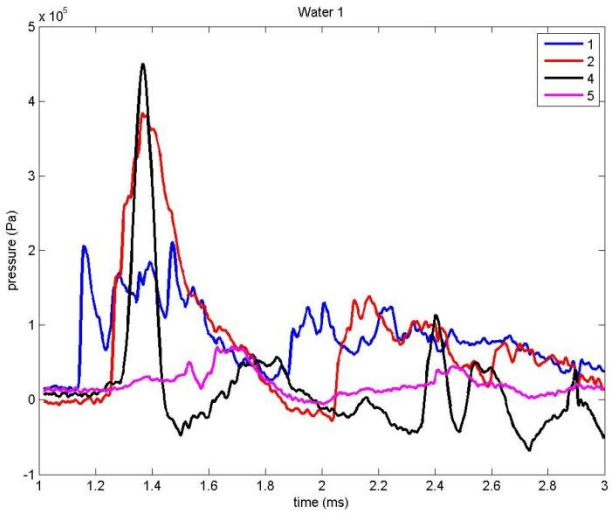


**Figure 5-17 - First water test**

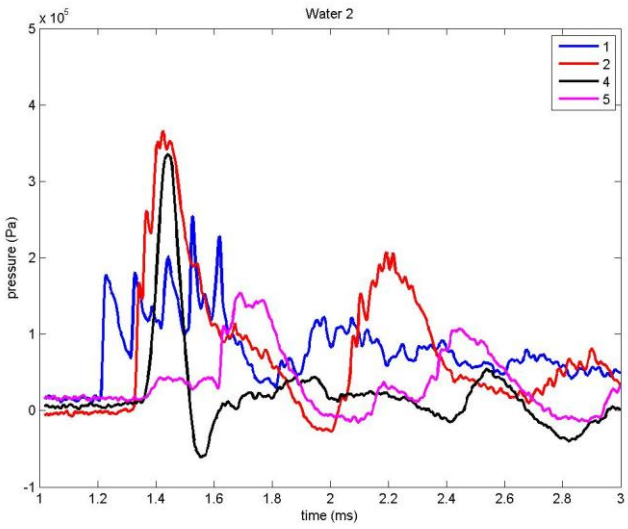


**Figure 5-18 - Second water test**

Once again the water results do display some qualitative consistencies between the two tests. In both tests, gauges 2 and 4 measure peak pressures at approximately the same time. In the first test, gauge 2 records just under 400 kPa while gauge 4 records over 450 kPa. In contrast, for the second test gauge 2 records a peak pressure of around 375 kPa while gauge 4 records only about 350 kPa. In both tests gauge 1 reaches an initial peak around 200 kPa; however, during the second test subsequent oscillations reach pressure levels of over 250 kPa. In the first test, gauge 5 records pressures under 100 kPa throughout the test, while for test two it records a peak pressure over 150 kPa.

### 5.3.2 Comparison By Measurement Location

To compare the performance of the different filler materials, the pressure readings at each gauge for the different tests are examined here. Results from the previous section suggest that it is not valid to simply average the pressure profiles for the two tests for each liner type to use in these comparisons. Instead, what is done here is to compare the "best" readings for each liner type and the "worst" readings of each liner type. That is, the tests with lower pressure levels for each liner type are compared, and the tests with higher pressure levels for each liner type are compared. Results for gauge 1 are presented first.

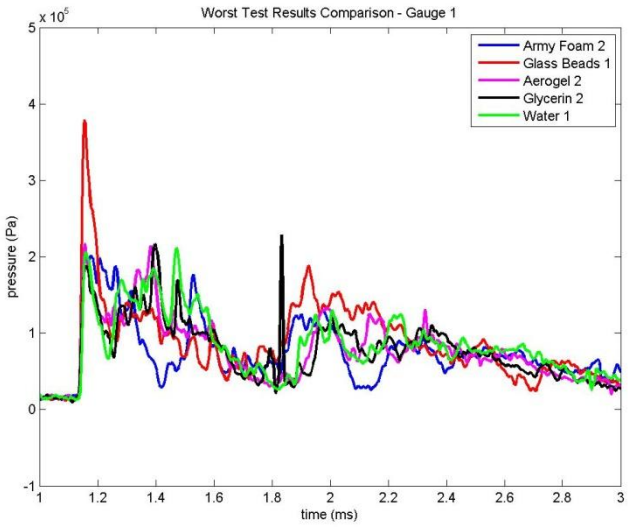


**Figure 5-19 - "Worst" case results at gauge 1**

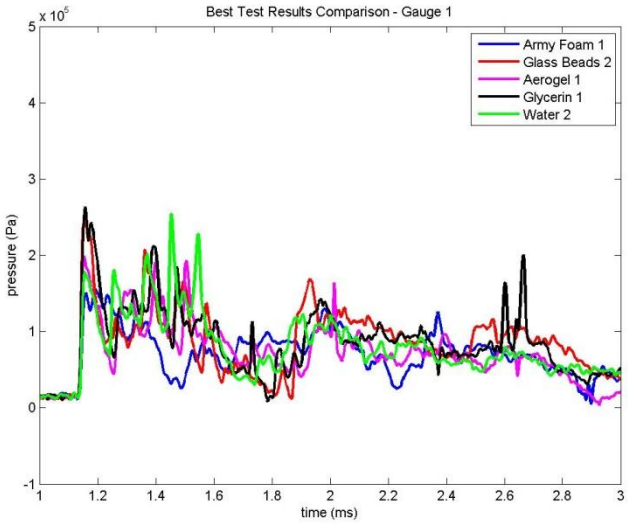


**Figure 5-20 - "Best" case results at gauge 1**

The pressure traces at gauge 1 for both tests for each material are given in Figure 5-19 and Figure 5-20. The time profiles were shifted for each so pressure began rising at the same time for all cases. In these figures it can be seen that, with the exception of the standard ACH foam, the general shape of the response curve for each filler material is the same. Positive overpressure durations for all filler materials are around 0.65 ms, after which another slower rise to peak in pressure is observed. The highest peak pressure observed was with a glass beads-filled liner at around 380 kPa. Comparing the worst cases for all liners, glass beads showed a consistently higher pressure throughout the blast event.

Water, aerogel, and glycerin all had very similar response curves. The peak pressure using the standard ACH pads was around 200 kPa, very similar to that using aerogel, glycerin, and water. The difference with the ACH pads was that a near-peak pressure was maintained for a longer period of time, then fell off sharply for a positive duration of only around 0.25 ms. The second "peak" pressure seen in the worst case figure probably corresponds to a reflection between the helmet support and the helmet and/or liner. The peak pressures reached during the second peak were roughly 50%-60% of the initial peak pressure.

The peak pressure reached in the best case comparison was with the glycerin-filled liner at around 275 kPa. The peak pressure with the glass beads filled liner was similar to glycerin. Aerogel and water had peak pressures just under 200 kPa, approximately the same as they were in the worst case comparison. For the filled liners, time durations were again around 0.65 ms. The peak pressure reached using the ACH pads was around 150 kPa, and again was maintained for a longer period of time before sharply falling for a time duration of around 0.30 ms. Again, a second pressure peak is later observed, with glass beads reaching the second highest peak pressure of around 170 kPa. Based on both comparisons and the peak pressures and smoothness of waveforms, it seems that for gauge 1 the ACH pads show the best mitigating capabilities. The results at gauge 2 are next discussed.

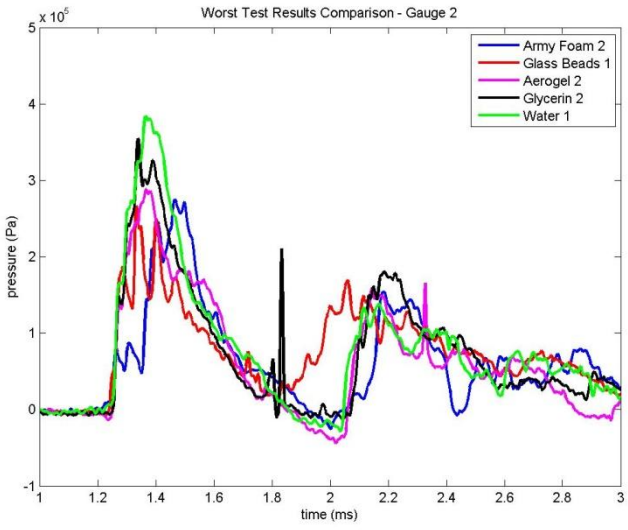


**Figure 5-21 - "Worst" case results at gauge 2**

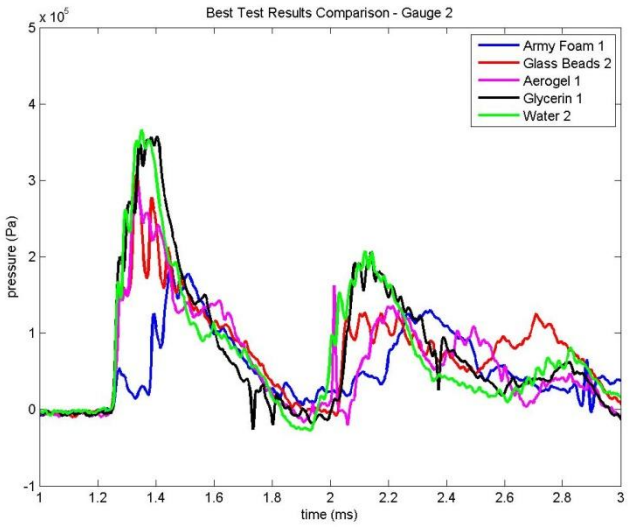


**Figure 5-22 - "Best" case results at gauge 2**

In both cases, water and glycerin reached the highest peak pressures of between 350 kPa and 400 kPa, generally higher pressures than seen at the first gauge. In the worst case, the ACH pads, glass beads filled liner, and aerogel filled liner all reached peak pressures around 285 kPa. The difference here is that the glass beads filled liners peaked first, followed by the aerogel liner, then finally the ACH pads. There is then a very narrow peak with the glycerin filled liner that was also observed at gauge 1. Positive durations were all about 0.70 ms, though looking at the fine scale variations glycerin had the shortest duration while ACH pads had the longest duration. Second pressure peaks are again seen with magnitudes around 50% of the initial pressure peaks.

The best case results show similarities to the worst case results. The glass beads-filled liner and aerogel filled liner again reached peak pressures of around 285 kPa at nearly the same time. However, the ACH pads reached a peak pressure of under 200 kPa much later than the other liners. Positive durations were around 0.65 ms, except for one low peak for glycerin which would make the "official" positive duration closer to 0.50 ms. Second pressure peaks are again observed with pressure magnitudes 50% to 60% of the initial peak pressure values. The lower pressure values and longest rise time suggest that the ACH pads provided the best mitigation at gauge 2. As mentioned before, gauge 3 became saturated during testing and results are unreliable. Therefore, gauge 4 will be discussed next.

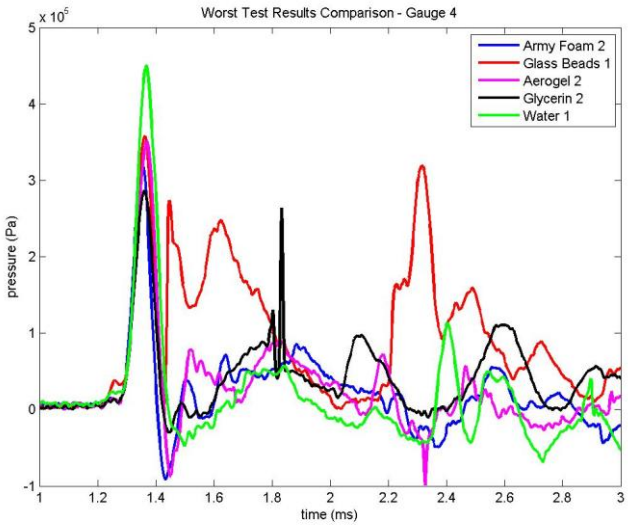


**Figure 5-23 - "Worst" case results at gauge 4**

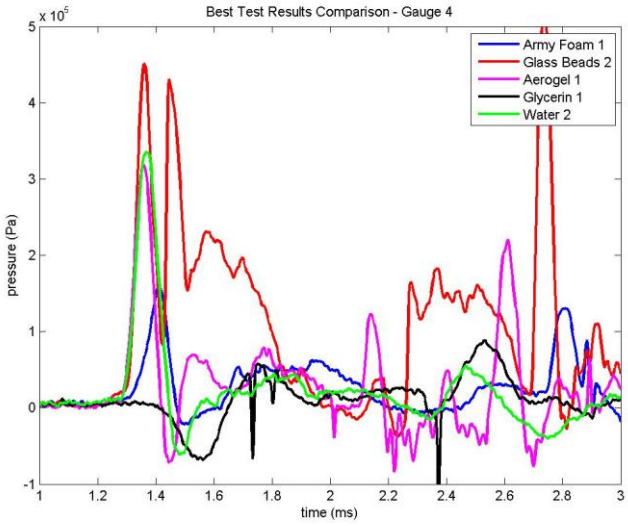


**Figure 5-24 - "Best" case results at gauge 4**

Similarities between the two divisions of tests here are more difficult to make. For the worst case test, water showed the highest peak pressure of around 450 kPa, the highest pressure discussed so far. Glass beads and aerogel came in second with peaks around 350 kPa, ACH pads were lower with a peak around 325 kPa, and glycerin was lowest at just under 300 kPa. The shape of these pressure peaks is much different than previous results as well. Pressure rise and fall was initially very fast, with positive durations only around 0.15 ms. Glass beads then exhibit an immediate pressure jump again, rising to about 275 kPa. The rest of the materials exhibit a negative (gage) pressure region, with the ACH pads

and aerogel filled liner reaching nearly -100 kPa. The only materials with a substantial second pressure events are glycerin and glass beads. Glycerin again shows a very sharp spike, also observed at the previously two discussed gauges. Glass beads, however, reaches a third pressure peak over 300 kPa.

The glass beads liner looks bad in the "best" case scenario as well. It reaches the highest peak pressure of nearly 450 kPa, relaxes back to atmospheric pressure, then jumps back up over 400 kPa almost immediately. There are two more lower level high pressure regions, followed by a third peak of over 500 kPa, the highest measured pressure of all tests and gauges. The water and aerogel filled liners exhibit peak pressures around 320 kPa and reach this value at about the same time glass beads first peaks. The ACH pads reach a peak of only about 150 kPa at a later time than the other materials peak. Glycerin shows virtually no positive pressure readings. In fact, pressure readings drop to negative values first. This suggests the gauge may have come loose during testing. At gauge 4, glass beads-filled liners display the worst results, while the ACH pads show the most promise. Finally, the results at gauge 5 are discussed.

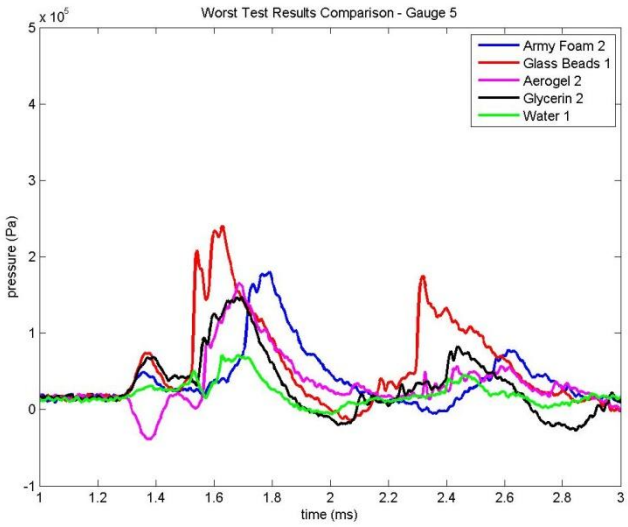


**Figure 5-25 - "Worst" results at gauge 5**

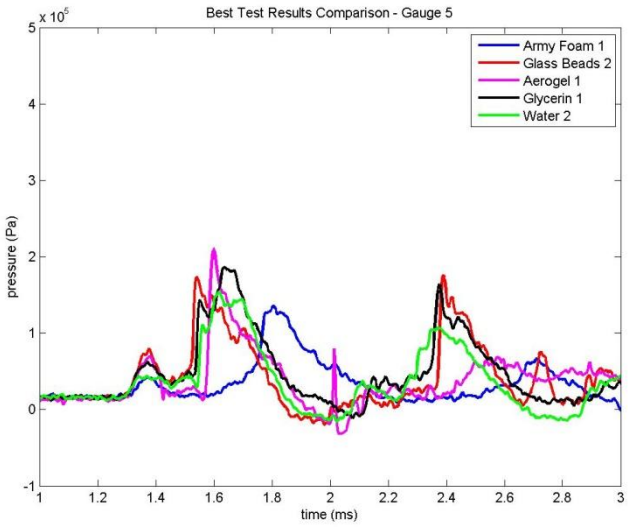


**Figure 5-26 - "Best" results at gauge 5**

With the exception of aerogel, in the worst case comparison at gauge 5 all tests show a smoother rise and fall of pressure to a relatively low (<100 kPa) peak value. Aerogel shows an initial pressure decrease during this same time frame. Higher pressure peaks are seen after this point. Glass beads exhibits the highest pressure peak of around 250 kPa and is the first to reach its peak value. Aerogel and glycerin later reach their peak pressure values of around 150 kPa. Then, the ACH pads reach the peak value of about 180 kPa. Smaller second peaks are again seen, with glass beads reaching the only significant peak value of just under 200 kPa.

Similar behaviors are observed for the best case scenarios. There is a small, smooth initial pressure hump followed by a sharp increase in pressure. This time, glass beads, glycerin, and water all show a jump in pressure at roughly the same time to values of 180 kPa, 150 kPa, and 120 kPa, respectively. Aerogel has a later jump in pressure up to over 200 kPa. Glycerin and water both show second jumps in pressure to values slightly higher than the original pressure jumps. The ACH pads liner is the last to reach its peak pressure of about 150 kPa. Later, glass beads and glycerin show second sharp jumps in pressure to peak values similar to those observed in the initial peak. Water shows a slower second rise in pressure up to just over 100 kPa. Results for gauge 5 again suggests glass beads do not provide as much mitigation as does the standard ACH liner.

## 5.4 Further Discussion of Experimental Results

Experimental results here are very interesting and somewhat contradictory to those performed on the sandwich structures using the same materials. With regards to sandwich structures, there was

very clear benefits to using Der-Tex foam with filler materials compared to the standard ACH helmet pads. Rise times were increased, peak transmitted pressures were reduced, and positive durations were increased. Glass beads, water, and glycerin were found to perform the best as filler materials, and aerogel was found to decrease the performance compared to a solid piece of foam. Quite opposite results have been found here. In most comparisons the ACH pads provided a larger increase in rise time and lower peak pressures compared to Der-Tex liners complete with filler materials. Glass beads-filled liners seem to consistently be among the worst performing at all gauges, though glass beads filled sandwich structures were among the best performers.

Another interesting aspect of these results to note is that pressure magnitudes show inconsistencies between the two tests at each material. This is most likely a result of several factors confounding these types of experimental results. First, the exact shape and location of the explosive and detonation cord are difficult to replicate from test to test. Test samples are prepared manually and are certainly not identical for every test. Furthermore, no matter how carefully the explosive is placed initially, assembly of the two shock tube chambers certainly moves the charge. Another important factor is the aim of the shock tube relative to the helmet set-up. To get perfectly consistent results, angular and translational alignment between the tube and helmet must be achieved. Furthermore, the helmet would need to be placed on the support exactly the same every time. Every effort was made to keep these factors consistent between tests, though without the aid of sophisticated laser alignment equipment. What is also important to observe, however, is that the shapes of the waveforms measured were fairly consistent between tests. In other words, even if the exact magnitude of the blast loading varied from test to test, the blast wave was still generally shaped the same way by the helmet and tube assembly. Pressure magnitudes may also be considered by comparing with other published results.

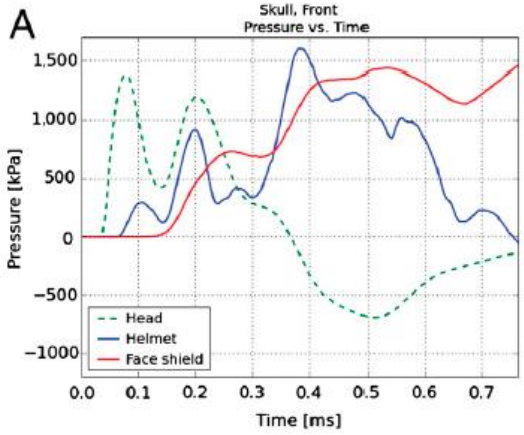


**Figure 5-27 - Numerical results from Nyein et. al. (19)**

The results presented in Figure 5-27 were obtained for a face on blast with 10 atm (1013.250 kPa) overpressure. The "head" trace is a blast directly onto a head model, the "Helmet" trace is with the usual ACH with standard pads, and the "Face shield" trace is for a new design they are exploring. The plot here is for the pressure on the front of the skull, in a location analogous to gauge 2 for the experiments performed here. Qualitatively, similar pressure increase profiles are seen for the experimental results and for the numerical results presented above for the "Helmet" trace. Also, the maximum pressure is just over 1.5 times the incoming overpressure compared to the experimental results here where the maximum pressure is most likely around 1.5 times the incoming overpressure. This fact can only be taken as an observation and not a hard confirmation of the validity of these results, though it is encouraging. A simplified geometry with different material properties was used here compared to cited simulation results. Nonetheless, it is worth mentioning.

Now, it is important to explore possible reasons these tests suggest the filled liner does not provide more blast mitigation capabilities than does the standard ACH pads. What are the main differences between what was done here and in-theater situations where blast mitigation really matters? First, there were large gaps between the liner and the support structure designed for these tests. A well-fitting ACH should maintain contact between the head and pads as much as possible. This eliminates free pathways for air to travel through, forcing compressive shock waves to travel through the pads/liner where dissipation and additional reflections may occur from impedance mismatches. The second pressure peaks seen in many of the tests are indicative of reflections between the PMMA support and the liner/helmet, something that should be avoided by a well-designed helmet liner. A second difference between this liner and the ACH pads is that the current prototype is of solid construction whereas the liner of the current ACH is of modular design. That should mean that free air pathways are eliminated by the new liner; however, as just discussed, the gap between the liner and PMMA prevents evaluation of this effect. Another difference is that in reality, the helmet covers a brain-filled skull while in these experiments, the helmet covered an air-filled PMMA tube. The dynamics of these two underlying structures are obviously different and will produce different results.

Data collection for this type of test is also an issue. The gauges used here are perfectly capable of handling the pressure levels observed. However, as mentioned before, they are pointed radially outward towards the helmet from inside the PMMA hemisphere. Pressure waves are transmitted through the PMMA tube and encounter the entire body of the sensor at various angles. It is unknown how these effects affect the measurements provided by the sensor.

# Chapter 6 Numerical Modeling

In addition to experimental work, a major thrust of this project is use of computer models to aid in the design and optimization of the new helmet liner. As previously mentioned, numerical modeling of the sandwich structure experiments has been done (73)(4). Two very different approaches were used in these two theses. Christou utilized the coupled Eulerian-Lagrangian (CEL) to provide air blast loading (73), while Goel took advantage of the ConWep module available in ABAQUS® v6.10 for loading. While Christou verified his numerical model with experiments as much as possible, the blast levels were so low that the uncertainty in results obtained was high. Goel was able to achieve accurate rise times and peak pressures using ConWep; however, positive durations and post-peak behaviors did not show an excellent match. Both of these results are significantly helpful when evaluating the validity of the model that will be presented here.

## 6.1 The Numerical Model

Modeling of the prototype dynamic response to blast loading was a nontrivial task, despite previous efforts on the sandwich structures. As alluded to in the introduction to this chapter, two different methods may be utilized to achieve blast loading, CEL analysis and the ConWep module. The significant advantage of the ConWep module is that modeling the air domain is unnecessary; loading is applied based only on the proximity and orientation of a surface with respect to a detonation point. However, there is a critical shortcoming of using the ConWep module. Reflections of shock waves from surfaces and shadowing of shock waves by interfering objects are not handled by the formulation (74). For the complicated geometry of the helmet, liner, and support structure, these effects must be accounted for. Therefore, it is necessary to use the CEL capabilities of ABAQUS®/Explicit to handle fluid-structure interactions for this project.

Coupled Eulerian-Lagrangian analysis is a very powerful feature offered by ABAQUS®. In a Lagrangian formulation, nodes of a mesh are fixed in the material and move as the material deforms. Furthermore, Lagrangian elements are always completely full of a single material; hence, the mesh defines the geometry of the structures considered. By contrast, in an Eulerian formulation, nodes are fixed in space, and material is allowed to flow into and out of elements. Naturally, this formulation is conducive to situations involving extreme deformations, such as gas flows. In ABAQUS®, Eulerian time incrementation is implemented with a "Lagrange-plus-remap" formulation. During the Lagrangian phase, nodes are assumed to be temporarily fixed in the material and deform accordingly. Then, during the Eulerian phase, significantly deformed elements are remeshed, and flow between elements is

calculated. CEL analysis allows for models to use both formulations, enabling simulations of multi-physics phenomena such as fluid-structure interaction (74).

In ABAQUS®, the Eulerian implementation is based on the volume-of-fluid method. That is, each element is assigned an Eulerian volume fraction indicating what fraction of the total element volume is occupied by a given Eulerian material. Whatever fraction of an element is not occupied by an Eulerian material is assigned void material, having neither mass nor strength. The actual shape of the structure composed of the Eulerian materials is constructed at each time step by creating planar facets governed by material volume fractions in neighboring elements. This method can lead to discontinuities in the constructed structure, and a fine resolution grid is usually necessary when using the Eulerian analysis (74).

What is truly important to this project are the fluid-structure interactions going on between the air, helmet liner, and support structure/head surrogate. Eulerian-Lagrangian contact in ABAQUS® is based on an enhanced immersed boundary method. Lagrangian parts overlap with an Eulerian mesh and occupy void regions. The general contact algorithm in ABAQUS®/Explicit then tracks the interfaces between Lagrangian structures and Eulerian materials. This formulation allows a simple, nonconforming Eulerian mesh to be constructed surrounding the domain of interest to capture the physics. This formulation requires that void material be initially included wherever a Lagrangian part overlaps. A Lagrangian part and Eulerian material may never occupy the same physical space (74).

Most of the preprocessing for this project was performed with ABAQUS®/CAE, including creation of all the geometry, boundary conditions, and material and section definitions. Initial conditions were largely written into the input file with a script, as will be discussed later. Because the blast events of interest were centered on the "face" of the helmet, symmetry was exploited so only half of the domain needed to be modeled and meshed. One of the first modeling decisions was how to handle the interface between the helmet shell and liner. In the standard ACH, the liner pads are attached to the shell with hook-and-loop pads. For the prototype liners tested, the liners were simply placed into the shell without any means of attachment. One could model the liner and shell separately and use contact conditions and tie constraints to join the two. For the time scales of interest, it was not anticipated that relative accelerations between the helmet and liner would matter. Therefore, for simplicity, the liner and shell were modeled as a single part, using separate section definitions to assign different material properties. The geometry for the standard ACH helmet is shown below along with its mesh.

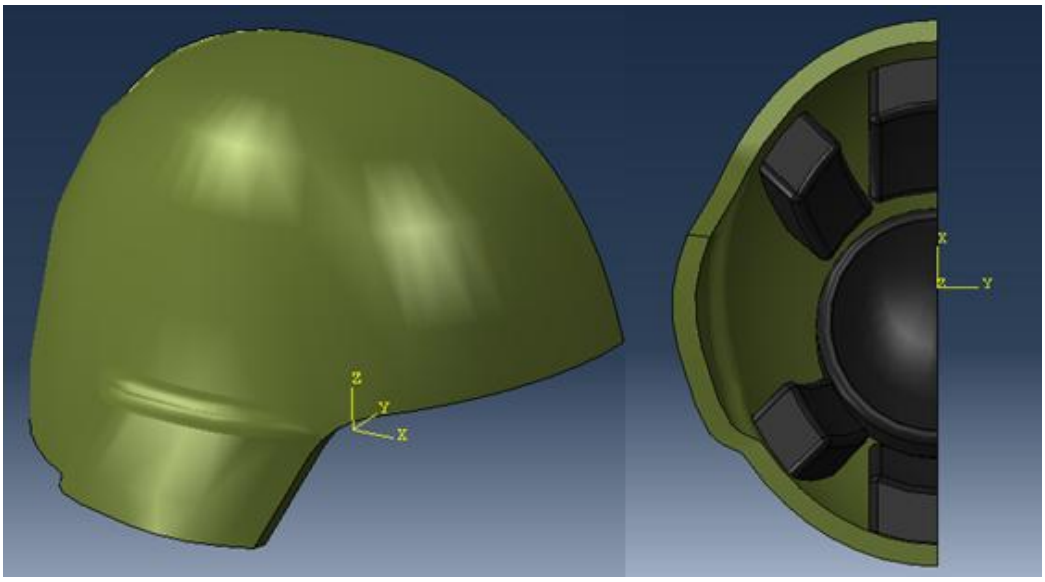

**Figure 6-1 - Standard ACH geometry**

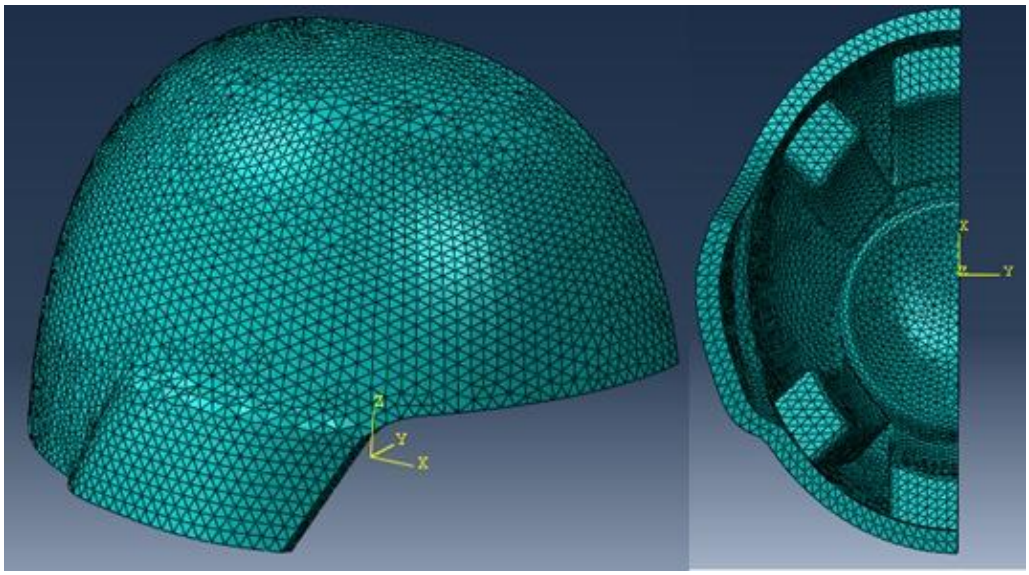

**Figure 6-2 - Standard ACH mesh - 66189 C3D4 elements (four node linear tetrahedral)**

Modeling of the helmet with the prototype liner required extra considerations. The main decision to make in that case was how to handle the filler materials. Water, glycerin, and glass beads all had the potential to flow and undergo large deformations, suggesting an Eulerian treatment should be used. Additionally, modeling these materials using an Eulerian formulation would introduce more realistic contact conditions between the filler and the foam. Similar contact properties may be obtained if the filler materials were modeled as Lagrangian parts separate from the helmet and liner, though overall filler behavior in the channels would not be realistic. Finally, the option to include filler materials

as a single part with the helmet and liner was also available, and this was the route chosen for these models. Attempts were made to model the filler materials with the Eulerian formulation. However, this led to an unidentifiable source of instability within the model and the Eulerian approach needed to be abandoned. The mesh of these liners inside the current ACH shell is shown below.

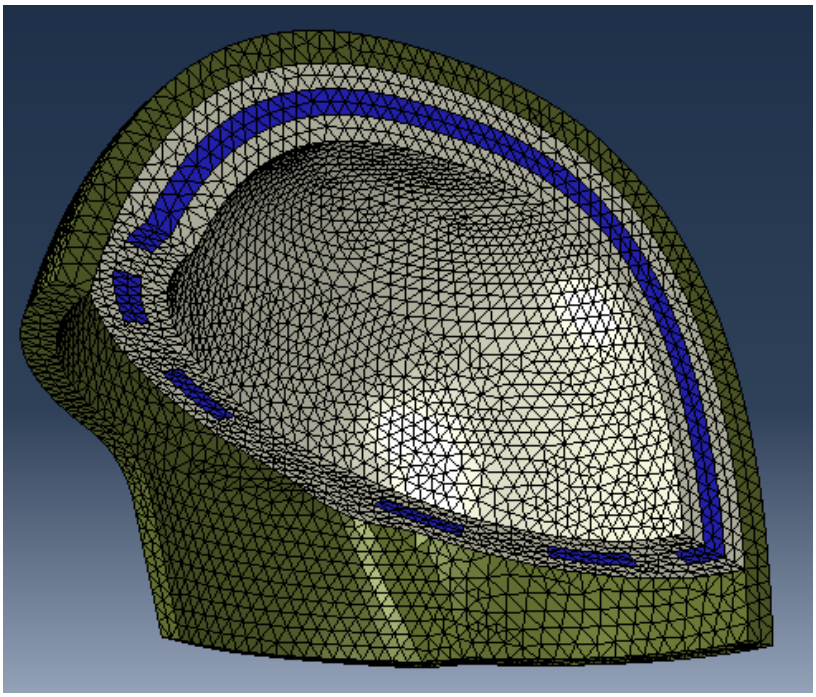

**Figure 6-3 - Mesh of helmet with prototype liner - 57260 C3D4 elements**

Assumptions were made when modeling the support structure as well (often referred to as "tube" in this report). This structure can be seen in Figure 5-7. Nominally this is a 6" OD PMMA cylinder with 1/8" thick walls topped with a PMMA hemisphere of compatible geometry. This structure is held in place by inserting it inside a steel pipe as seen in the figure. To reduce the model size and complexity, the steel tube was not included in the model. Rather, its effect was approximated by modeling the tube extending 10 cm from the base of the hemisphere and fixing the bottom surface of the tube. Furthermore, it can be seen in the figure that pressure gauges were secured in the hemisphere as well, requiring five drilled holes for the sensors and one larger hole for the wires to pass through drilled into the cylinder. Modeling of all the internal sensors and wires would have dramatically increased the complexity of the model. Furthermore, properties of the sensors, wires, etc would need to be approximated in a way that would likely be inaccurate. It was determined that the model would be most effective by simply modeling the tube with no holes or internal structures. The tube mesh is shown below along with yellow datum points corresponding to the pressure gauge locations. Elements

are sized to be as nearly cube-shaped as possible while including two elements through the thickness of the tube. These elements are small enough to limit the simulation time step, and having smaller elements would be undesirable. Shell elements could also be used; however, when used with the CEL formulation problems may arise regarding pressure on each side of the element.

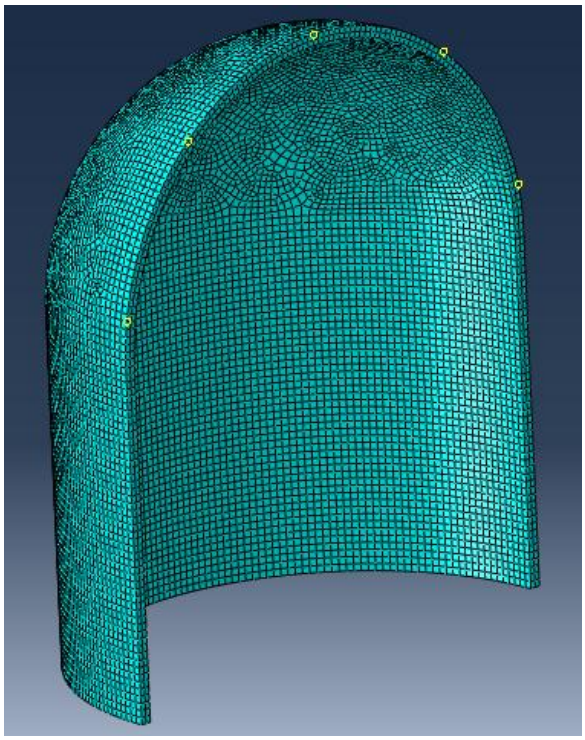

**Figure 6-4 - Tube mesh - 21274 C3D8 (eight node linear brick elements)**

The final part of the model is the air domain surrounding the helmet. As mentioned during the description of CEL analysis, often times the most effective Eulerian domain is a simple, regular grid of elements surrounding the domain of interest. It was decided to simply model the air domain as a rectangular prism surrounding the helmet. Symmetry is again exploited, and the symmetry plane of the air domain corresponds to the symmetry plane of the helmet and tube. The air domain extends approximately 2.3 cm beyond the back of the helmet, approximately 4.8 cm above the top of the helmet, approximately 3.0 cm outside the farther side of the helmet, and approximately 14.8 cm in front of the front of the helmet. The total overall dimensions of the air domain are 42.0 cm x 15.0 cm x 25.0 cm. Elements in the mesh of the air domain are 3.0 mm x 3.0 mm x 3.0 mm EC3D8R eight node linear Eulerian bricks with reduced integration and hourglass control. The default hourglass control is used. There are 581000 elements in the air domain mesh. The air domain surrounding the helmet as viewed from the symmetry plane is shown below.

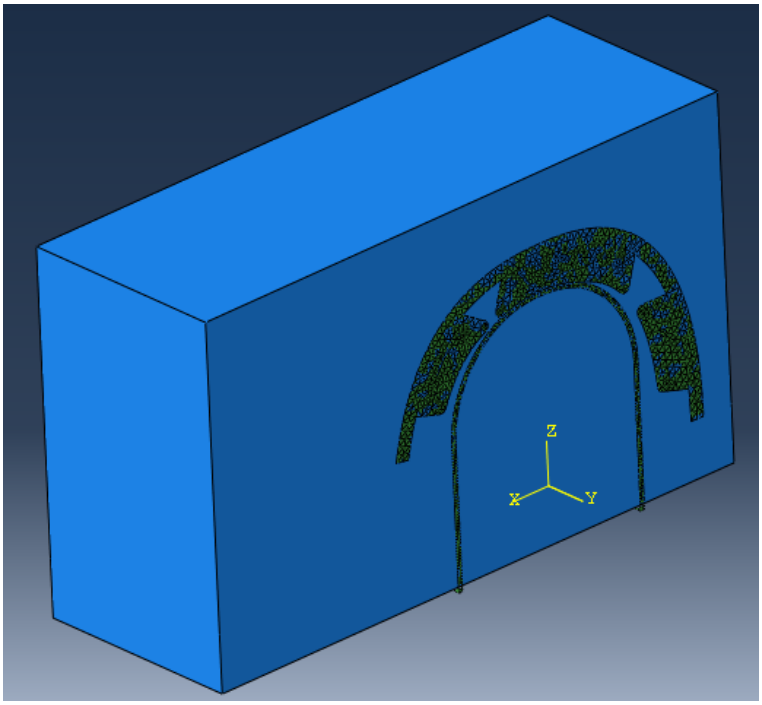


**Figure 6-5 - Air domain surrounding the helmet and tube**

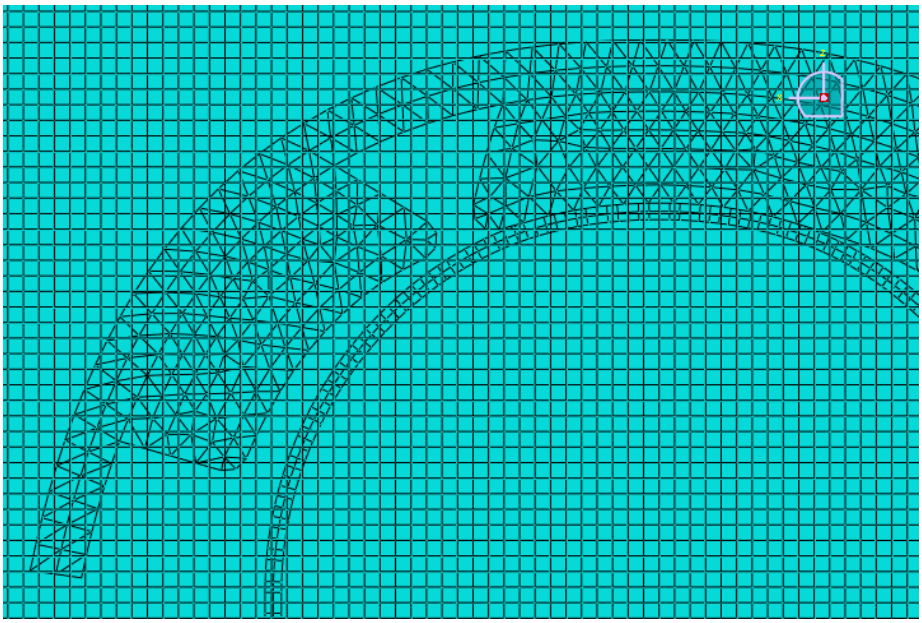

**Figure 6-6 - Comparison of meshes of the air domain, helmet, and tube**

From Figure 6-6, it is clear that the Eulerian mesh is rather coarse, especially with regards to the tube. Some elements extend to both sides of the tube. However, element size reduction quickly leads to a large number of elements. Nearly 700000 elements are used in the analysis as is, which already

pushes the limits of the capabilities of the machine these simulations are run on. This needs to be considered when interpreting results.

## 6.2 Model Initialization

Before a blast event could be simulated, proper interfacing between the tube and the helmet needed to be established. Rather than create conforming geometries, it was decided to use the realistic geometries and perform an initial simulation initiating contact between the two parts.

### 6.2.1 Boundary Conditions

The initialization step begins with the helmet above the tube so the distance from the top of the tube to the bottom of the top center portion of the liner are 18.0 mm apart, as shown below.

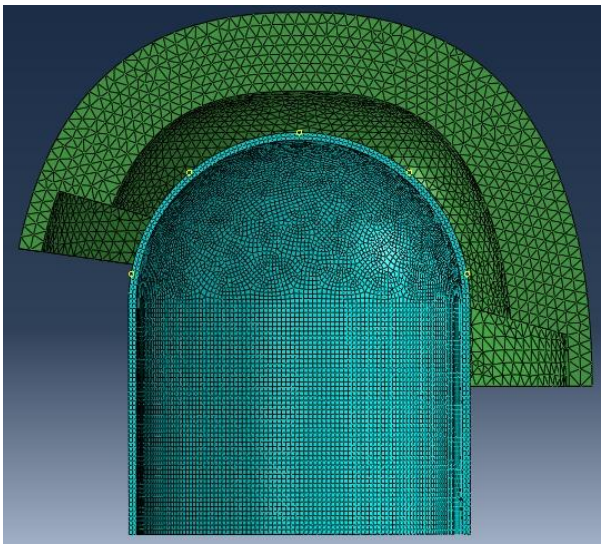

**Figure 6-7 - Placement of parts prior to the initialization step**

Symmetry boundary conditions were imposed on the tube and helmet. That is, displacement normal to the symmetry plane is prescribed a permanent value of zero throughout the simulation Figure 6-8. To prevent rigid body motion, nodes on the outside of the helmet shell were fixed completely at locations corresponding approximately to where the straps anchor to the actual ACH Figure 6-9.

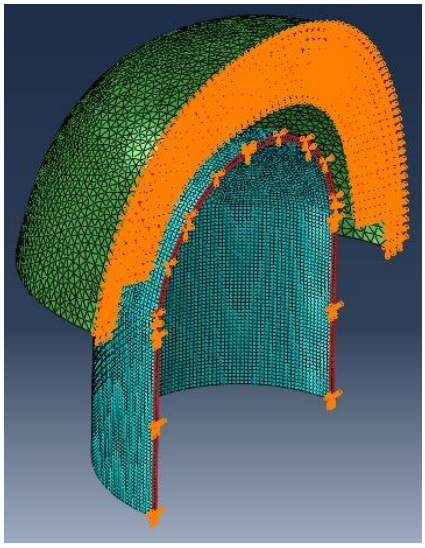

**Figure 6-8 - Orange and red regions correspond to locations of symmetry boundary conditions**

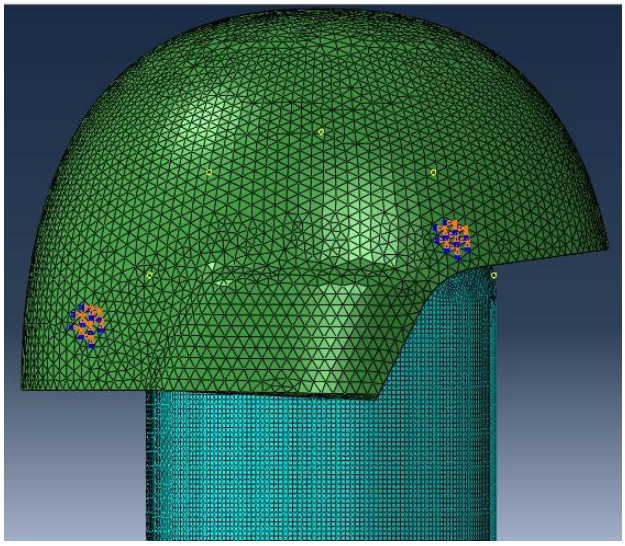

**Figure 6-9 - Anchor points for the helmet denoted in orange and blue**

To initiate contact between the parts, it is necessary to move one of the parts. As already indicated, the helmet was fixed. Therefore, the tube needed to be displaced to initiate contact. Corresponding to experimental observations, for the prototype liners the tube was displaced 18 mm towards the helmet, while for the ACH pads the tube was displaced 20 mm towards the helmet. To implement actual displacement, the bottom surface of the tube was prescribed the vertical displacement over the course of the simulation step. To prevent rigid body motion, this surface was also prescribed zero displacement in the direction parallel to the symmetry plane and perpendicular to the displacement direction. The surface prescribed these conditions is highlighted below. The general

contact algorithm is used to model interactions between the helmet and tube. Normal contact is implemented with the "Hard" Contact pressure-overclosure relationship using the default constraint enforcement method. Separation is allowed after contact. Tangential contact is treated as frictionless, a valid assumption based on the soft nature of the liner and the smooth nature of the tube surface.

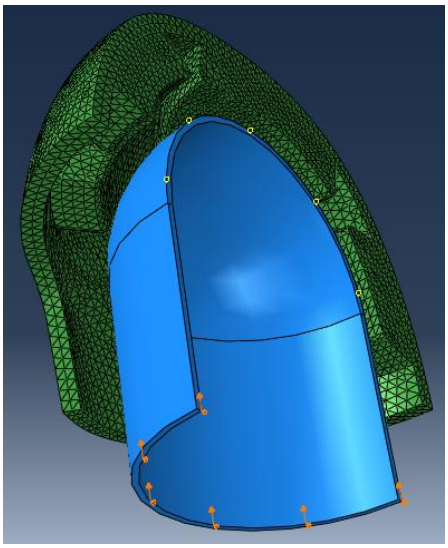

**Figure 6-10 - Orange arrows indicate prescribed displacement of the tube**

### 6.2.2 Simulation Details

For simplicity and efficiency, a general static step was taken using ABAQUS®/Standard. The step was taken over 10 seconds and accounted for nonlinear behavior. Automatic stabilization was used with a dissipated energy fraction of 0.0002 and a maximum ratio of stabilization to strain energy of 0.05. Step increments were automatically calculated to a maximum step size of 1 second. A direct solver was used with the Full Newton method and loads ramped linearly over the step. No extrapolation was used at the start of each increment. Because the material for Der-Tex includes viscoelasticity, a long-term solution was obtained with time-domain material properties.

For the fluid filler materials, an equation of state is used to describe volumetric behavior. This material model is not available in ABAQUS®/Standard. Hence, a new material approximation was required. Water is traditionally treated as an incompressible medium, and usual relations between elastic moduli generally fail when using a Poisson's ratio of 0.5. To approximate the strength of water for this initialization step, a linear elastic model was used wherein the Young's modulus was set to the bulk modulus of water, and Poisson's ratio was set to 0.4999. Stresses and strains within the channels

following this initialization step were low, and assumed to be adequate for describing the initialization for all filler materials.

The main output from these simulations is the deformed coordinates of the helmet, liner, and tube. These deformed parts are then used as the main parts for the blast simulation.

## 6.3 Air Blast Simulation

The deformed parts from the initialization analysis step are imported to compose the air blast model. Only the coordinates of the nodes are imported. The stresses developed during the initialization step are not imported, for the main purpose of the initialization step is simply to establish contact between the helmet and tube. A main difference between the initialization and blast steps is inclusion of the air domain in the blast step. Further details of the simulation are discussed next.

### 6.3.1 Boundary Conditions

The tube and helmet symmetry boundary conditions are the same in both steps. The region of the tube that was displaced in the initialization step instead is fixed in the two directions parallel to the symmetry plane corresponding to the steel tube holding the PMMA tube. The boundary condition fixing the helmet shell is released during this step and is not necessary during this dynamic analysis. This is physically realistic, for during experiments the helmet was simply placed on top of the tube.

The air domain is introduced during this step. Consequently, boundary conditions need to be imposed. On the symmetry plane, zero velocity normal to the symmetry plane is imposed. On all other surfaces of the Eulerian mesh, free inflow and free outflow conditions are imposed. These boundary conditions are illustrated below. General contact conditions are used for these simulations as well.

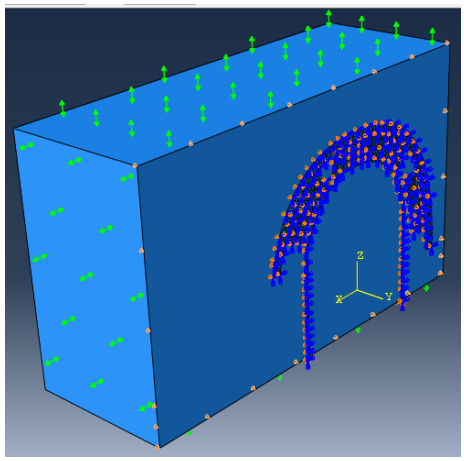

**Figure 6-11 - Boundary conditions on the Eulerian mesh**

### 6.3.2 Initial Conditions

There are a couple of different ways to impose air blast loading on the helmet. Like this work, Christou used CEL analysis for his blast simulations. He introduced a planar blast wave to the domain by imposing a time-varying pressure distribution on one of the Eulerian surfaces (73). While this approach allowed the velocity and temperature fields to evolve along with the pressure wave propagation, there were two drawbacks. First, simulation effort was increased substantially by waiting for the propagating blast wave to encounter the test sample. Second, the method was restricted to a planar wave. The test samples considered here are substantially larger than the samples Christou was simulating; hence, the planar wave assumption is less valid. To avoid these drawbacks, the general approach described by Kambouchev et. al. (32) is implemented here.

Kambouchev et. al. (32) used a closed-form solution to a strong air blast to initiate the velocity and pressure field in their work. The blasts considered in this work are not strong enough to use the same formulation. However, the Bach and Lee (34) provided a solution more valid for the levels experienced here. This solution was presented in detail in Section 2.2. It remained to estimate the parameters to input to the model to determine the pressure and velocity field throughout the air domain. Goel found the ConWep module provided an adequate loading condition for simulations (4). A simulation of the ConWep module loading several single elements out to a distance of 12" was used as the starting point. The loading was applied to the back surface of the elements to assess the transmitted pressure rather than the reflected pressure. The elements were fixed completely. Pressure was assessed by summing the reaction forces and dividing by the area of the element, consistent with the practices in the ABAQUS® verification manual (74). The peak pressure obtained at 12" from a blast of 2.87 kg TNT was 164500 kPa. This was used to estimate a shock velocity according to Equation 2-10. Equation 2-30 and Equation 2-32 were then solved using an fourth-order Runge-Kutta (traditional RK4) integration scheme. Finally, Equation 2-24 and Equation 2-26 are solved to give the velocity and pressure fields. A comparison of the pressure field predicted by the model of Bach and Lee and that given by the ConWep module is provided in Figure 6-12. The plot shows that the analytical expression provided by Bach and Lee adequately describes the behavior provided by the ConWep module.

The solution obtained with the Bach and Lee model is valid for spherical blast symmetry. The assumption applied in these simulations is that a spherical blast is initiated in open air at the center of the mouth of the shock tube. To that end, it is a straightforward procedure to initialize the state of the air domain based on a point of detonation.

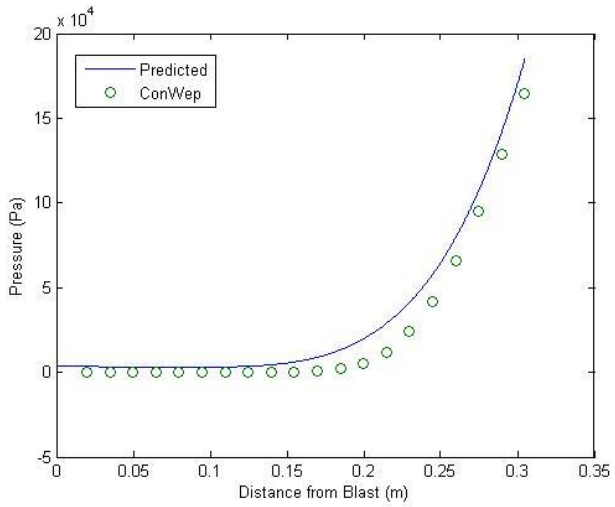


**Figure 6-12 - Comparing ConWep and the Bach and Lee model**

The general initialization of the blast model is described here. First, the helmet and tube are imported from the first simulation step. These parts and the air domain are assembled, and boundary conditions are imposed. Next, the Volume Fraction Tool in ABAQUS®/CAE is used twice in a non-intuitive way. First the volume fraction of helmet and liner in each Eulerian element is calculated. Second, the volume fraction of the tube in each Eulerian element is calculated. The input file is then manipulated directly to complete the field state initialization. First, the node numbers and locations of the Eulerian domain are pulled from the input file. Next the elements and corresponding node numbers are pulled from the input file. A script is then used with the Bach and Lee model to calculate the field velocities, pressures, and densities of each node in the Eulerian domain. The ideal gas model is used with the calculated pressures and densities to obtain the nodal temperatures. Initial air pressures can only be described for elements, not nodes. Therefore, each element is initialized with a pressure equal to the average of the pressures of its eight associated nodes. Volume fractions of each Eulerian element are initially set full of air. The volume fractions obtained with the Volume Fraction Tool are then subtracted from the appropriate elements to create void space for the Lagrangian parts within the Eulerian domain. A contour plot of the initialized pressure field is shown in Figure 6-13.

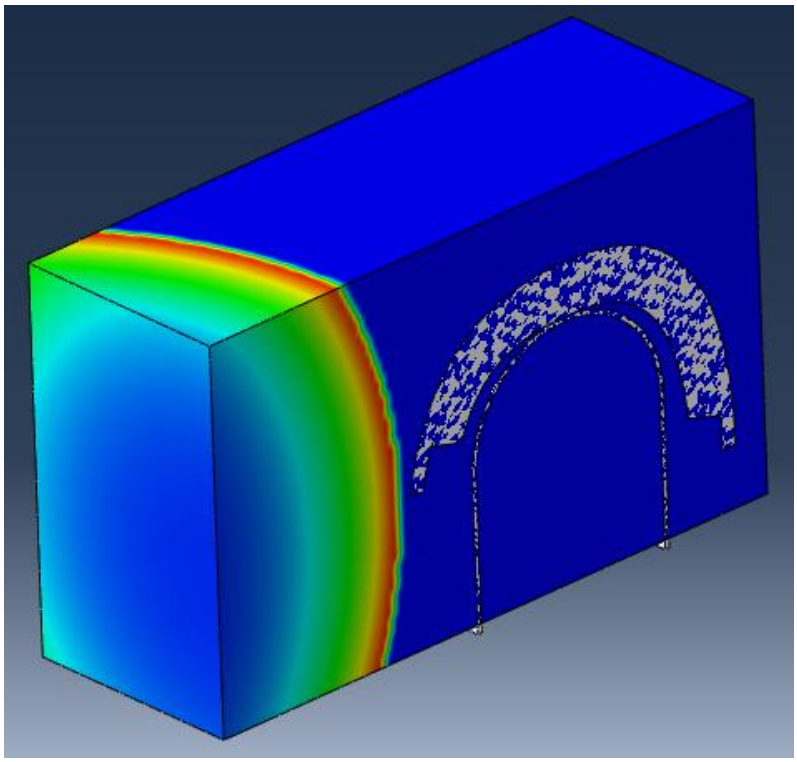

**Figure 6-13 - Contour plot of the initialized pressure field**

### 6.3.3 Simulation Details

Non-linear dynamic finite element simulations are run in ABAQUS®/Explicit v6.10. Simulations are run for a total time of 1 ms. Automatic time incrementation is used. Generally time steps were on the order of tens of microseconds. Consistent with the findings of Christou, linear and bulk viscosities were set to 0.2 and 1.2, respectively (73). To achieve the best understanding of the capabilities of the model, five simulations were run, corresponding to the helmet with standard ACH pads and the helmet with the prototype liner filled with water, glycerin, glass beads, and aerogel.

The data available for experimental validation are pressure values recorded by the pressure transducers embedded in the PMMA hemisphere. Several ways to take similar values from the simulations were considered. First, the air pressure of the Eulerian element immediately adjacent to the measurement location on the tube was investigated. Typical pressure values at this location seemed to be consistently low. This is not surprising considering the coarse nature of the mesh and the "sharp" shape of the blast wave front. Eulerian elements are restricted to reduced integration, and all quantities are evaluated at a single integration point at the center of the element. Second, it was considered to examine the pressure inside the elements of the tube near the measurement site. These measurements were also low and highly oscillatory, generally being affected by stress wave propagation through the

tube itself. Third, the contact pressure at the nodes of the tube corresponding to the experimental measurement locations were considered. This represents the stress developed in preventing penetration of air into the tube geometry. Generally pressure levels obtained numerically seemed consistent with those measured experimentally. The main drawback of using this measure is that underpressures are not recorded; however, overpressures are of greater interest for this model validation.

### 6.3.4 Results By Filler Material

First, the results for the model of the standard ACH helmet are presented. The pressure profile at each measurement location is provided below.

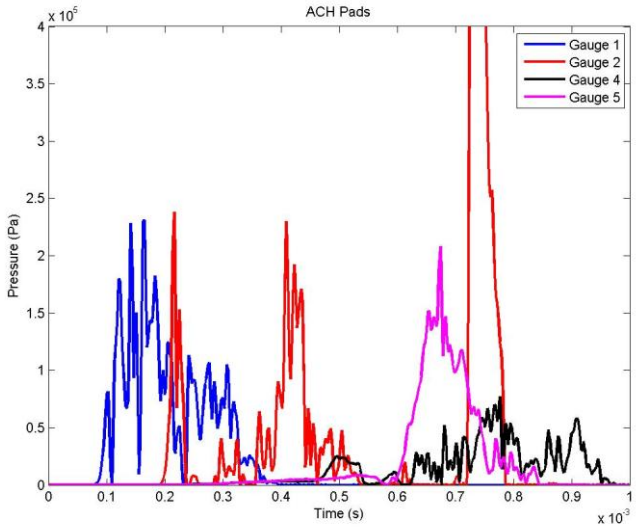


**Figure 6-14 - Simulation results for the standard ACH helmet**

As with all simulation results provided here, results have been run through the general SAE filer provided by ABAQUS® with a cutoff frequency of 100 kHz. Many of the features seen in Figure 6-14 are similar to the experimental results shown in Figure 5-9 and Figure 5-10, while there are some anomalous features as well. Initial peak pressures observed at gauges 1, 2, and 5 are in the 200 - 250 kPa range, consistent particularly with the second set of experimental results. Furthermore, temporal spacing between the peaks at these gauges is consistent with both sets of experimental results. This excludes the sharp initial peak seen at gauge 2, which was not at all seen experimentally. There is another high magnitude (>400 kPa) pressure peak observed at the second gauge location. While a second peak was observed experimentally, it did not occur until nearly a full millesecond after the initial peak. Not observed in the numerical model is the initial high pressure peak at the fourth gauge location that was

measured experimentally in both cases. However, the lower magnitude (<100 kPa) pressure variations seen numerically are consistent with experimental results. The other noticeable discrepancy between experimental and numerical results is the width of the pressure peaks. Experimentally, the high pressure regions lasted for a longer period of time, whereas the pressure peaks were more "sharp" numerically. Next, the results for the prototype liner filled with glass beads are discussed.

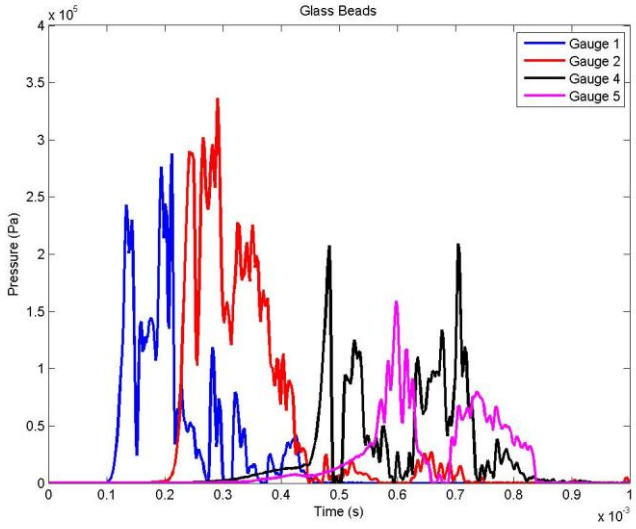


**Figure 6-15 - Simulation results for a glass beads-filled prototype**

The comparison between experimental and numerical results for a glass beads-filled liner is similar to that for the standard ACH helmet. The initial peak for gauges 1, 2, and 5 are around 250 kPa, 300 kPa, and 165 kPa, respectively, consistent especially with the second set of experimental results. Furthermore, temporal spacing of these peaks is consistent with experimental results as well. There are second, higher pressure peaks shortly after the initial pressure peaks at gauges 1 and 2. A similar behavior is seen for the second gauge, but not for the first gauge experimentally. Once again, there are high pressure peaks observed experimentally early in the blast event that are not observed numerically at gauge location 4. There are sharp pressure peaks observed numerically consistent in magnitude (~200 kPa) with pressures observed experimentally. As with the standard ACH pads, the pressure peak temporal widths numerically were much smaller than the widths seen experimentally. The results for an aerogel-filled prototype liner are discussed next.

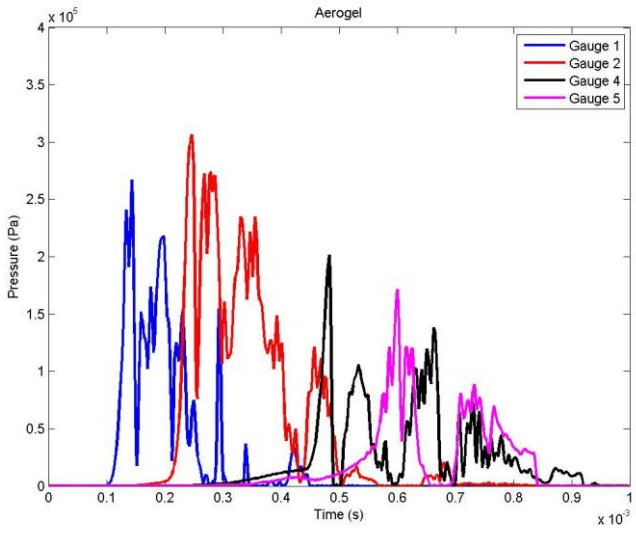


**Figure 6-16 - Simulation results for an aerogel-filled liner**

Many of the same observations may be made about the numerical and experimental results for an aerogel-filled liner as were made about the previously discussed cases. The simulated peak pressure at gauge 1 is slightly higher than those values obtained experimentally. However, consistent with experimental results the peak pressure at gauge 1 is lower than that at gauge 2. Peak pressures at gauges 2 and 5 are consistent with experimental results. Once again, temporal spacings between pressure peaks at gauges 1, 2, and 5 were consistent with experimentally obtained values. The only gauge showing no real consistency between experimental and numerical results is gauge 4. An early pressure peak is missed numerically. In contrast to previous results, gauge 4 pressure peaks observed numerically are not observed experimentally. Results for a glycerin-filled liner are presented next.

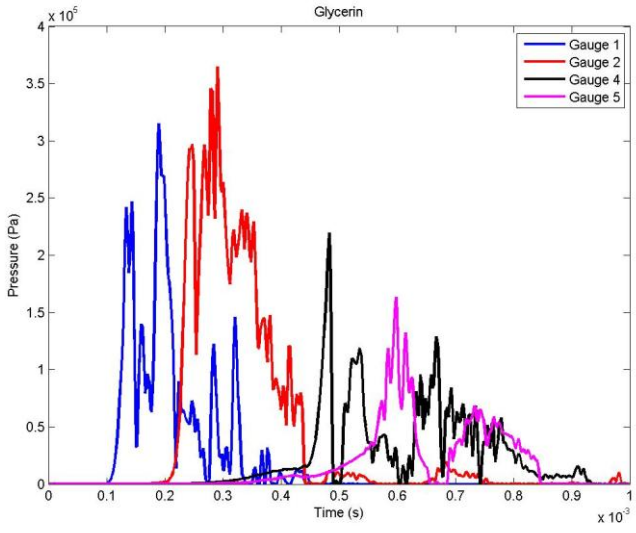


**Figure 6-17 - Simulation results for a glycerin-filled liner**

Similar consistencies between experimental and numerical results are observed for a glycerin-filled liner as were found previously. Peak pressure values obtained at gauges 2 (360 kPa) and 5 (185 kPa) and the initial peak pressure obtained at gauge 1 (250 kPa) matched particularly well with the first set of experimental data. Spacing of these particular peaks was also consistent with experimental results. A second pressure peak is seen numerically shortly after the initial pressure peak that was not observed experimentally. Similar inconsistencies are found for gauge location 4, an early pressure peak is missed and subsequently observed numerical and experimental pressure peaks do not match well in either time nor magnitude. Finally, the results for a water-filled liner are discussed.

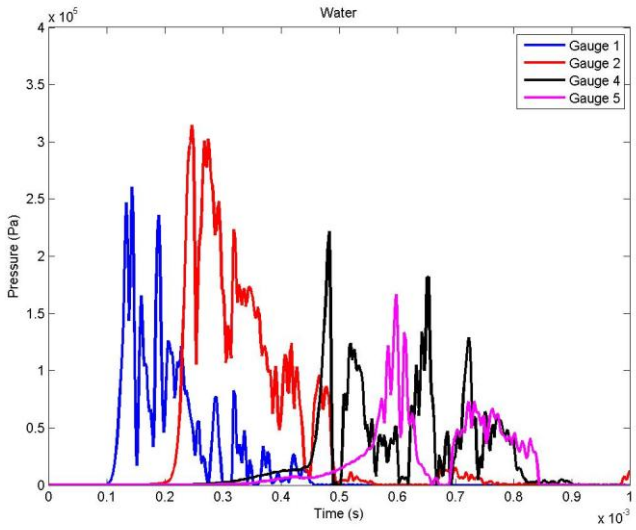


**Figure 6-18 - Simulation results for a water-filled liner**

The simulation results for water do not match quite as well with experimental results compared to the previously discussed cases, though the results are still sufficiently consistent. The numerical model seems to overestimate the peak pressure at gauge locations 1 and 5 while underestimating the pressure at gauge location 2. Spacing between the peaks, however, is consistent with experimental results. Once again, little consistency is observed between numerical and experimental results at gauge location 4.

### 6.3.5 Results By Measurement Location

To try to glean some insight into the relative performance of the different helmet liners with respect to this test stand, a comparison of pressure profiles by gauge location is performed below.

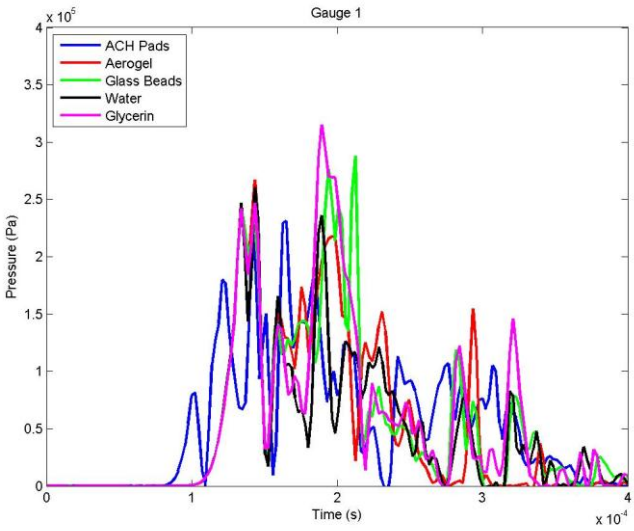


**Figure 6-19 - Comparison of numerical results at gauge 1**

At gauge 1 it is immediately clear that the altered geometry of the helmet liner affects when the pressure arrives at the first gauge, for every pressure profile starts rising at the same time except for the standard ACH. The early time pressure responses for all filled liners are very similar, differing only slightly in magnitude but all in the neighborhood of 250 kPa. Deviations in behavior occur after this point. Glycerin and glass beads experience a second high magnitude pressure peak, with glycerin reaching a top value of over 300 kPa. The lowest peak pressure of all liners was observed with the standard ACH pads, never reaching a value higher than 250 kPa. Furthermore, the rise time to peak pressure was the longest for the ACH pads, There were no appreciable differences in positive overpressure time durations. A comparison at gauge 2 is considered next.

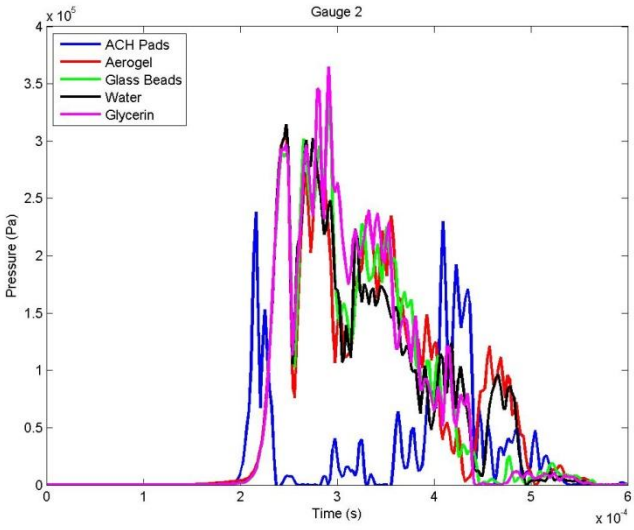


**Figure 6-20 - Comparison of numerical results at gauge 2**

It was noted in the previous section that the first peak seen here for the ACH pads was not observed experimentally. However, in light of the fact that at the first gauge, pressure started rising for the ACH pads before all the other liners, it would seem that this peak is very relevant. It is interesting to see that after this peak, there is virtually no contact pressure until later, when a second peak of nearly equal magnitude is observed. Regarding the other filler materials, once again profiles are very similar until after the peak pressure is reached. Glycerin reaches the highest peak pressure at over 350 kPa, with glass beads again reaching the second highest peak pressure of nearly the same value. The rise time is longer for the filled liners than it is for the standard ACH pads. Once again, the lowest peak pressure is observed using the ACH pads at just under 250 kPa. Results at gauge 4 are discussed next.

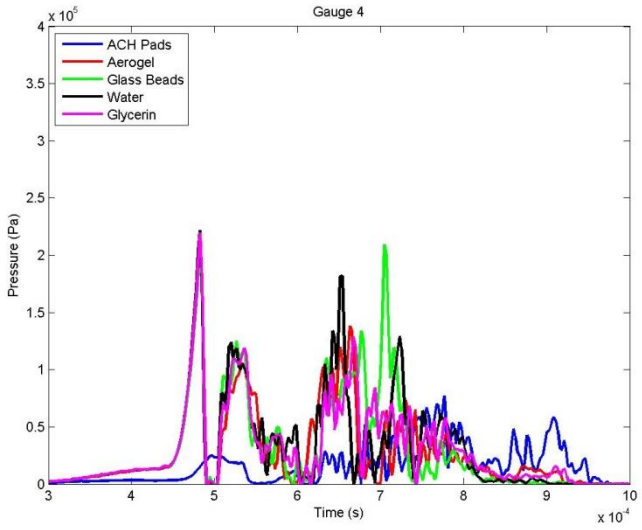


**Figure 6-21 - Comparison of numerical results at gauge 4**

While the numerical results did not show the same initial peak results as seen experimentally, there were later pressure peaks calculated. All filled liners experienced a peak pressure of 225 kPa, while pressure with the ACH pads never rose much about 50 kPa. The filled liners all displayed subsequent pressure increases, the highest of which occurred for glass beads (200 kPa). As has been the case so far, the pressure levels with the ACH pads have been lowest. Finally, the results at gauge 5 are examined next.

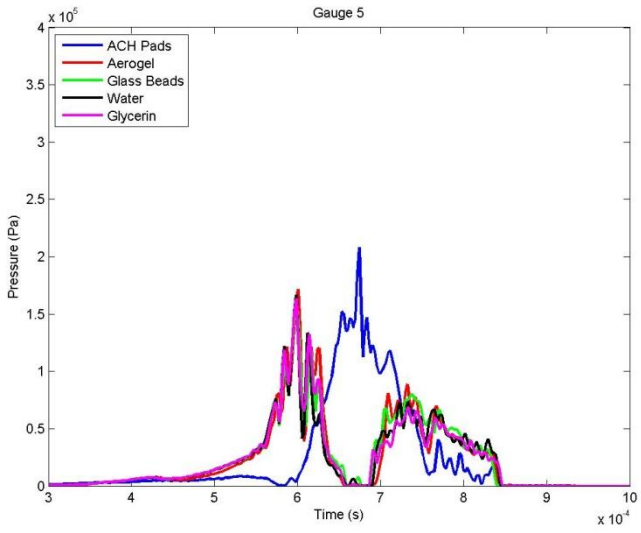


**Figure 6-22 - Comparison of numerical results at gauge 5**

Pressure profiles for all filled liners are very similar throughout the duration of the simulation, reaching a peak pressure of 170 kPa. The pressure peak for the ACH pads occurs later than the peak of the filled liner and is, in fact, higher in magnitude at over 200 kPa.

### 6.3.6 Further Discussion of Simulation Results

Caution must be exercised when drawing conclusions based on the work presented here. In general, comparisons of pressure profiles at the various measurement locations seem to indicate clearly that the ACH pads outperform the prototype liners in terms of peak pressures. Also, with respect to the first gauge, it seems the rise time to peak pressure is better with the ACH standard pads rather than the prototype liner explored here. However, the pressures measured in these experiments are not affected by the liner composition as much as geometry. This is not a result of a flaw in the single liner design as opposed to a modular design, rather it is a direct result of the liner not conforming to the geometry of the support structure. One example of evidence supporting this claim is that, despite having significantly different material models for filler materials, the prototype liners all showed very similar pressure profiles at all measurement locations initially. Furthermore, this claim is supported by a contour plot of the pressure wave interacting with the helmet and tube. In Figure 6-23, the pressure wave is clearly seen having traveled under the rim of the helmet and moving through the space between the liner and tube. Pressures recorded at the gauges are a result of this pressure wave traveling through air rather than a compression wave traveling through the helmet and liner.

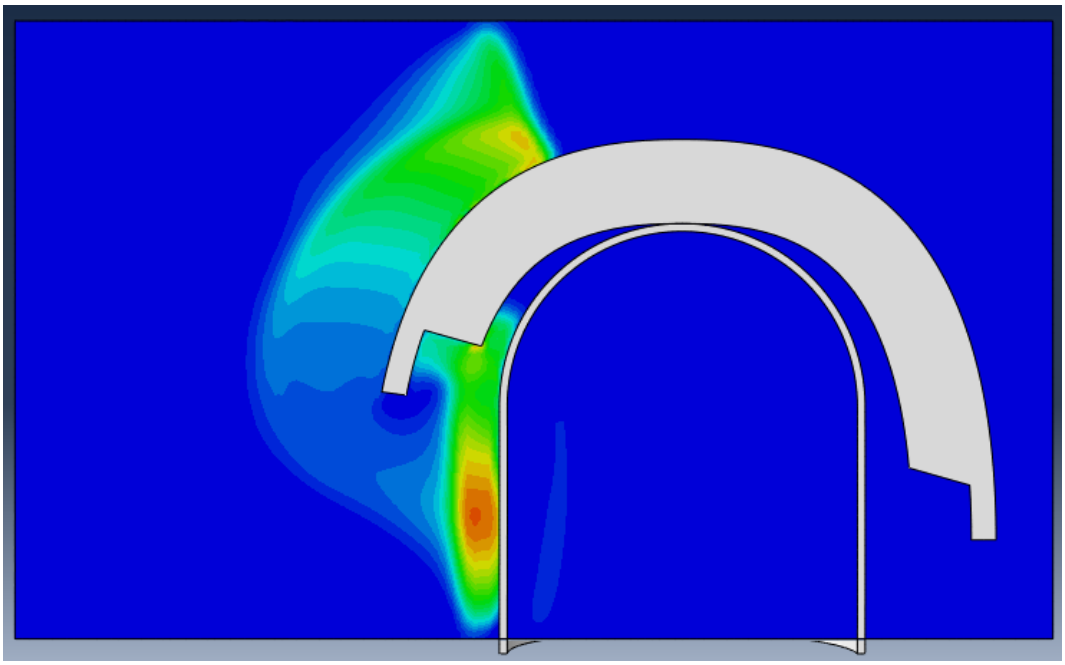

**Figure 6-23 - Contour plot of the pressure wave interacting with the helmet and tube**

It is also interesting to note the inconsistencies seen in gauge 4 for all simulations. The initial pressure peaks seen experimentally follow a very smooth profile, unusually smooth in fact. Furthermore, these peaks occur at the same time peaks occur at gauges much closer to the detonation point. This suggests a possible malfunction in this particular pressure gauge. This is further supported by the consistencies between experimental and numerical results found with the remaining gauges (excluding gauge 3, which became saturated).

The model worked remarkably well considering the relatively coarse mesh used to model the air domain. There were Eulerian elements that, in fact, had nodes both inside and outside the tube walls, though this seemed to cause no great difficulty. To obtain meaningful results it was necessary to take contact pressure readings from nodes not contained with an Eulerian element enclosing the full thickness of the tube. Originally it was attempted to avoid this issue all together by partitioning the air domain to coincide with the midplane of the walls of the tube. While this solved the issue of having elements fully encompassing the thickness of the tube wall, it led to swept meshes included elongated and deformed elements located in crucial areas of fluid-structure interaction. This "conforming" mesh is shown below, as well as the poorly shaped elements resulting from that particular mesh.

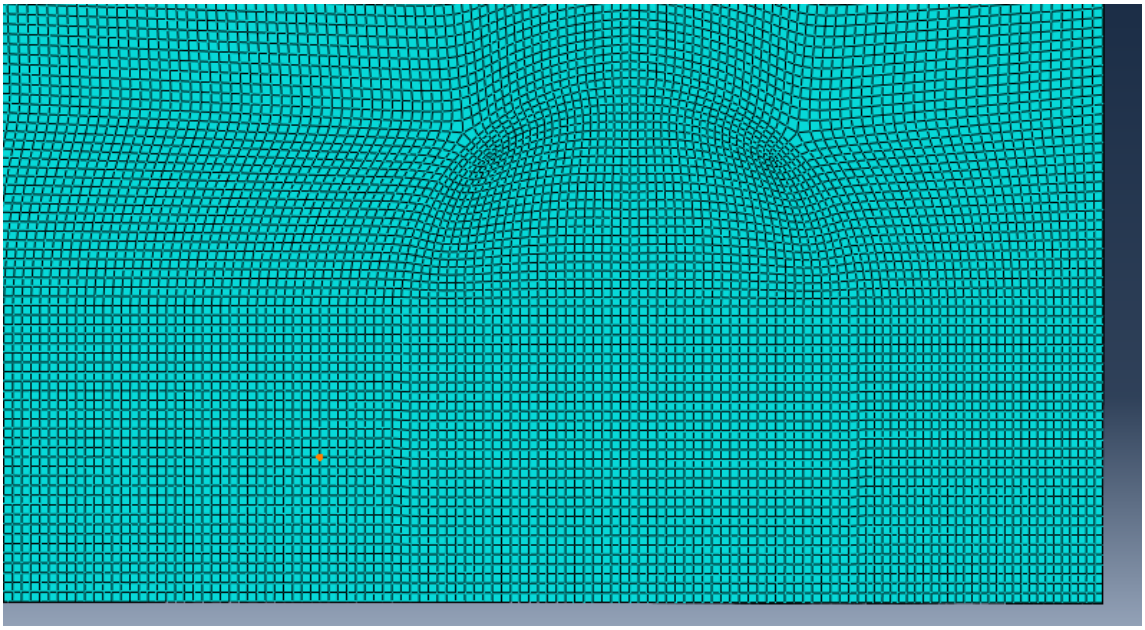

**Figure 6-24 - Illustration of conforming Eulerian mesh**

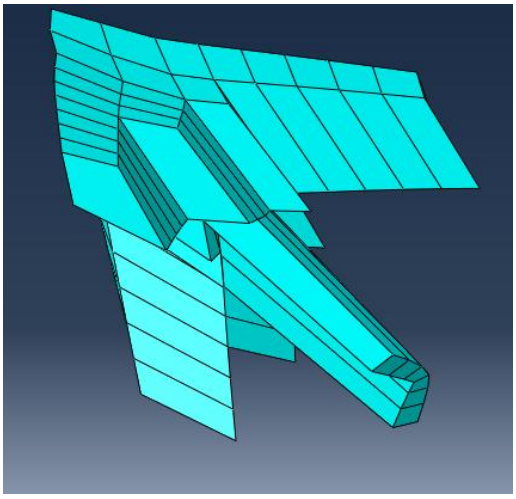

**Figure 6-25 - Illustration of poorly shaped elements resulting from the conforming mesh**

Pressure peak widths did not appear consistent with experimental results. However, this is likely a product of the initialization of the blast field using the relation of Bach and Lee. Those relations assume a spherical blast symmetry in free air. However, an explosive drive shock tube was used for experiments, which likely altered the shape of the blast wave. While the peak pressure and propagation velocity of the blast wave seem to have been captured well, the shape of the wave applied experimentally probably deviates somewhat from that applied numerically. Overall, comparisons with experimental results support the validity of the model that has been developed here.

# Chapter 7 Conclusions and Future Work

Insight obtained from the experimental and numerical work presented in previous chapters is summarized here.

## 7.1 Conclusions

The overall goal of this ongoing blast helmet project begun three years ago is to determine if a liner including channels filled with various materials can provide a greater degree of protection from blast waves than can the current ACH liner. It is unknown exactly what mechanisms cause blast-induced TBIs; hence, the protection capabilities of a helmet must be estimated based on various measures of mechanical performance. In previous work, such measures have included rise time to peak pressure, peak overpressure, positive overpressure time duration, negative time duration, blast underpressure magnitude, and blast impulse. The most accurate and accessible measures of comparison between the different liners for the work presented here are the rise times and peak pressures. On the basis of rise times and peak pressures observed during the numerical and experimental tests presented here, the current standard ACH configuration performed better than the prototype liners containing various filler materials. Rise times for all of the filled prototype liners are roughly the same. However, glass beads and glycerin-filled liners displayed the highest peak pressures during the early time of the blast event. An overly simple interpretation of these results suggests the prototype liners fail to achieve the main objective.

However, as cautioned in Section 6.3.6, it is probably premature to make judgments about the performance of the newly designed prototype helmet liner based solely on the results presented here. In reality, a soldier's helmet should fit much better than the helmet samples fit the test support structure, with each support pad mostly or fully contacting the head directly. The gaps between the helmet liners and the support structure in the work presented here were shown to provide a direct path for shock wave propagation through air, bypassing the liner for the most part. Differences in dynamic responses were observed for different liners; however, this is mostly due to compressing of the liner by the shock wave traveling through the air gaps rather than compression waves being transmitted through the helmet shell and liner to the tube. Furthermore, the blast event considered here corresponds to a soldier looking directly at the source of the blast. The helmet must protect against blasts from all directions, and in other orientations stress waves in the brain are more likely to be due to the transmission of a compression wave through the helmet rather than the blast wave curving around the rim of the helmet shell.

Another reason to hold off on conclusions about the performance characteristics of the prototype liner compared to the standard ACH helmet is the difference between the tube support and an actual head. The "head surrogate" used here was a tube constructed of PMMA and generally filled with air. A human head, by contrast, is composed of skin, fat, bone, and brain matter. The dynamics of shock propagation and reflection are different for the structure used here compared to a human head. Not only will fluid-structure interactions differ between the blast wave in air and head or head surrogate, but also stress wave propagation and reflection will differ at interfaces of the helmet liner and head or head surrogate.

While the overarching goal of the blast project is to design an improved helmet liner using the filler material idea, the main thrust of the work described in this report was to develop and validate a model describing the dynamic response of a (modified) helmet coupled with a head surrogate to an impinging air blast wave. To this end it seems reasonable to deem the project a great success. Several assumptions and simplifications were required throughout the modeling process. However, the fair agreement between experimentally and numerically obtained results serves as strong evidence of the validity of these assumptions. Notable features of the model are listed as a point of summary.

- The ACH helmet shell, helmet liner, and any fillers are all modeled as a single part, having different section definitions to delineate regions of different material properties. This greatly reduces the complexity of the model by eliminating otherwise required contact definitions and nodal tie constraints. Furthermore, initialization of air in the Eulerian domain is achieved by only running the Volume Fraction Tool (VFT) twice, saving some model setup time.
- The head surrogate was modeled numerically simply as a cylinder and connected hemisphere filled with air. Holes for wires and pressure transducers were not included, nor were the transducers or wires. Consistency between numerical and experimental results, particularly at gauge location 5, support this simplification.
- The total modeling and solution process consists of two simulation steps. The first step, a nonlinear static analysis in ABAQUS®/Standard, initializes contact between the helmet liner and head surrogate. Because ABAQUS®/Standard does not support EOS material models, those materials require some other assumed material model, such as a linear elastic model. The second step, a nonlinear dynamic analysis in ABAQUS®/Explicit, models the blast event and the dynamic response of the structures involved.

- The Eulerian mesh is relatively coarse, having element edge lengths larger than the thickness of the tube support structure. Ideally this mesh would be much finer. However, because the model is in three-dimensions, the total number of elements increases very quickly with decreases in element width size. Because of the relatively coarse mesh, care needed to be taken to evaluate model outputs at nodes not belonging to elements overlapping the entire thickness of the tube.
- Blast loading is achieved by initializing the velocity, pressure, and temperature field within the air domain using the analytical solution for open air blasts with spherical symmetry presented by Bach and Lee (28)(34). The pressure field obtained with this method was shown to be very similar to that given by the ConWep module. The validity of the shock magnitude and propagation velocity is supported by the matching of peak pressures and pressure peak spacing in numerical and experimental results. The main discrepancies seen between numerical and experiment results are the positive time durations, being much smaller in the numerical results than in the experimental results. It is not unexpected to see some differences, for the analytical solution to the blast waves assumes a spherical blast in open air, while actual loading came from an explosive drive shock tube.
- Out of the three considered simulation outputs chosen to compare with the pressure measurements obtained experimentally (contact pressure between the air and tube, pressure within the elements of the tube, and pressure in the Eulerian element immediately above the tube), contact pressure on the tube was found to be the closest to experimentally obtained values. The only downfall to studying only this output is that underpressure regions are not captured quantitatively.

## 7.2 Suggestions for Future Work

A general framework for simulations of air blast loading on an ACH with different helmet liners has been designed and validated. Now, this framework may be used towards achieving the ultimate goal of this project to design a helmet liner for improved blast protection. All indications from initial work on sandwich structures suggest the filler material idea does provide enhanced blast protection (4). Whether these results extend directly to an actual helmet geometry may be assessed with a modified version of this model. The most important modification to make to the model to gain realistic insight is to use a more realistic head surrogate. This could be something as complicated as the human head model used in (19), or something as simple as a conforming geometry with a bony shell and water-filled

inner structure. The main idea of this modification would be to eliminate the gaps between the helmet liner and tube seen in this work allowing the blast wave to contact the head surrogate without having to propagate through the helmet and liner. Such simulations would provide a direct comparison of the performance of the standard ACH to that including a modified liner.

In addition to testing the helmets with a more realistic head model, it is important to test the helmet performance in other realistic blast scenarios. This means a couple of different things. First, both the orientation and distance of the helmet with respect to the blast point should be altered to many different values. Changing the orientation changes the central loading point on the helmet, while changing the distances changes the radius of the shock front encountering the helmet/head surrogate. Second, different blast magnitudes and, therefore, shapes may be tested as well by varying parameters in the Bach and Lee model used to determine the initial conditions. Performing these different tests may require other tweaks to the model as well. For example, moving the detonation point most likely necessitates a change in shape of the Eulerian domain for both accuracy and computational efficiency purposes. Also, if the detonation point is moved off of the symmetry plane, then symmetry may no longer be exploited and the full helmet and head surrogate must be modeled. This effectively doubles the size of the computational domain, but would be necessary to obtain an accurate result.

In such future simulations where shock transmission to the head surrogate is facilitated more by transmission through the liner and helmet, it will probably be necessary to assess the mesh used for the filler materials. Ideally, the fillers would be treated using an Eulerian approach. However, as mentioned before, some unidentified source of instability arises with this particular model using Eulerian material for the fillers. It is most likely the case the Eulerian mesh needs to be much finer to resolve this instability. However, the simulations performed here already pushed the memory limits of the available equipment. Also, if the filler materials are treated with an Eulerian mesh, some sort of boundary condition or end cap must be included to separate the filler material from the air. It may also work to increase the Lagrangian mesh density within the channels and maintain a more manageable mesh size overall.

The most important work this model may be used for is development of an optimally performing liner. Several different modifications to the prototype liner may be tested. A modular design should be tested for more direct comparison with the current ACH pad configuration. Alternate filler material properties, including properties of hypothetical materials, should be tested. Different channel sizes and shapes should be considered as well. Ultimately the goal should be to provide an

acceptable level of blast protection while minimizing the weight added to the current standard ACH helmet. If possible, the thermal properties of this liner compared to the standard ACH liner should be considered as well, for in a desert environment high ambient temperatures necessitate some measure of ventilation should be afforded by a combat helmet.

This model may potentially provide a substantial amount of insight regarding the performance of a helmet with respect to blast loading. It should be a valuable asset in future design and optimization efforts of a liner incorporating the filler material idea, which has shown so much promise in previous work.

## Appendix A - Coefficients in the Perturbation Solution of Bach and Lee

The coefficients presented below are contained in (28) and are used for initialization of the blast field for the simulations in this project.

$$\theta_0 = -(j+1)/2$$
$$y_1 = -E_1/(C_1 + A_1\theta_0)$$
$$\theta_1 = \theta_0^2\left[A_2 + B_1\theta_0 + C_2/\theta_0 + E_2/(y_1\theta_0)\right]/C_1$$
$$y_2 = -y_1\theta_1/\theta_0$$
$$\theta_2 = \theta_0^2\left[A_3 + (B_1-1)\theta_1 + B_2\theta_0 + \left(C_1\theta_1^2/\theta_0^2 - C_2\theta_1/\theta_0 + C_3\right)/\theta_0 + E_3/(y_1\theta_0)\right]/\left[C_1 + E_1/(2y_1)\right]$$
$$y_3 = y_1\left[\theta_1^2/\theta_0^2 - \theta_2/(2\theta_0)\right]$$
$$\theta_3 = \theta_0^2\left[(B_1-2)\theta_2 + B_2\theta_1 + B_3\theta_0 + \left\{C_1\left[2\theta_1\theta_2/\theta_0^2 - \theta_1^3/\theta_0^3\right] + C_2\left(\theta_1^2/\theta_0^2 - \theta_2/\theta_0\right) - C_3\theta_1/\theta_0 + C_4\right\}/\theta_0 + \left\{E_1\theta_1\theta_2/\left(3\theta_0^2\right) - E_2\theta_2/(2\theta_0)\right\}/(y_1\theta_0)\right]/\left\{C_1 + 2E_1/(3y_1)\right\}$$
$$y_4 = y_1\left\{7\theta_1\theta_2/\left(2\theta_0^2\right) - 3\theta_1^3/\theta_0^3 - \theta_3/\theta_0\right\}/3$$

$$A_1 = D_1/[4(\gamma+1)]$$
$$A_2 = -1/2 + [2 + (\gamma-1)(j+1)]/(\gamma+1) + (3D_1+4)/[4(\gamma+1)]$$
$$A_3 = [1 - (\gamma-1)(j+1)]/(\gamma+1)$$
$$B_1 = -1/2$$
$$B_2 = 2[2 + (\gamma-1)(j+1)]/D_1$$
$$B_3 = -8[2 + (\gamma-1)(j+1)]/D_1^2$$
$$C_1 = D_1\left[D_1 + j(\gamma+1)\right]/\left[4(\gamma+1)^2\right]$$
$$C_2 = \left\{-D_1^2 + D_1[6 - (\gamma-1)(2j+1)] + 4j(\gamma-1)\right\}/\left[4(\gamma+1)^2\right]$$
$$C_3 = \left\{D_1[-6 + (\gamma-1)(j+1)] + 4[2 - (\gamma-1)(2j+1)]\right\}/\left[4(\gamma+1)^2\right]$$
$$C_4 = -[2 - (\gamma-1)(j+1)]/(\gamma+1)^2$$
$$E_1 = -(\gamma-1)(j+1)D_1^2/[8(\gamma+1)]$$
$$E_2 = -(\gamma-1)(j+1)D_1/(\gamma+1)$$
$$E_3 = -2(\gamma-1)(j+1)/(\gamma+1)$$
$$D_1 = \gamma(j+3) + j - 1$$

# References


1. **Defense and Veterans Brain Injury Center.** DVBIC. [Online] http://www.dvbic.org.

2. *Traumatic Brain Injury Hospitalizations of U.S. Army Soldiers Deployed to Afghanistan and Iraq.* **Wojcik, Barbara E., et al.** 1S, s.l. : Elsevier Inc., 2010, American Journal of Preventive Medicine, Vol. 38, pp. S108-S116.

3. *Military TBI During the Iraq and Afghanistan Wars.* **Warden, Deborah.** 5, s.l. : Lippincott Williams & Wilkins, Inc., 2006, Journal of Head Trauma Rehabilitation, Vol. 21, pp. 398-402.

4. **Goel, Rahul.** *Study of an Advanced Helmet Liner Concept to Reduce TBI: Experiments & Simulation using Sandwich Structures.* Aeronautics and Astronautics, Massachusetts Institute of Technology. Cambridge, MA : s.n., 2011. Masters Thesis.

5. *The Effects of High Explosives Upon the Central Nervous System Lecture I.* **Mott, Fred W.** 4824, February 12, 1916, The Lancet, Vol. 187, pp. 331-338.

6. *The Effects of High Explosives Upon the Central Nervous System Lecture II.* **Mott, Fred W.** 4826, February 26, 1916, The Lancet, Vol. 187, pp. 441-449.

7. *The Effects of High Explosives Upon the Central Nervous System Lecture III.* **Mott, Fred W.** 4828, March 11, 1916, The Lancet, Vol. 187, pp. 545-553.

8. *Shell shock, Gordon Holmes and the Great War.* **Macleod, A. D.** February 2004, Journal of the Royal Society of Medicine, Vol. 97, pp. 86-89.

9. *Blast-Related Traumatic Brain Injury: What Is Known?* **Taber, Katherine H., Warden, Deborah L. and Hurley, Robin A.** 2, s.l. : American Psychiatric Publishing, Inc., Spring 2006, Journal of Neuropsychiatry Clinical Neuroscience, Vol. 18.

10. **Bowen, I. G., Fletcher, E. R. and Richmond, D. R.** *Estimate of Man's Tolerance To The Direct Effects of Air Blast.* Albuquerque, NM : Lovelace Foundation for Medical Education and Research, 1968.

11. *A Thoracic Mechanism of Mild Traumatic Brain Injury Due to Blast Pressure Waves.* **Courtney, Amy C. and W., Courtney Michael.** 1, January 2009, Medical Hypotheses, Vol. 72, pp. 76-83.

12. *Blast (explosion)-Induced Neurotrauma: A Myth Becomes Reality.* **Cernak, I.** 2005, Restorative Neurology and Neuroscience, Vol. 23, pp. 139-140.

13. *Biomechanics of traumatic brain injury.* **El Sayed, Tamer, et al.** s.l. : Elsevier B. V., 2008, Computational Methods in Applied Mechancs and Engineering, Vol. 197, pp. 4692-4701.

14. *Biomechanical Assessment of Brain Dynamic Responses Due to Blast Pressure Waves.* **Chafi, M. S., Karami, G. and Ziejewski, M.** 2, s.l. : Biomedical Engineering Society, February 2010, Annals of Biomedical Engineering, Vol. 38, pp. 490-504.

15. **Kleiven, S.** *Finite Element Modeling of the Human Head.* Royal Institute of Technology. Stockholm, Sweden : s.n., 2002. Ph.D. Thesis.

16. *A Virtual Test Facility for the Simulation of Dynamic Response in Materials.* **Cummings, Julian, et al.** s.l. : Kluwer Academic Publishers, 2002, The Journal of Supercomputing, Vol. 23, pp. 39-50.

17. *A Virtual Test Facility for the Efficient Simulation of Solid Material Response Under Strong Shock and Detonation Wave Loading.* **Deiterding, Ralf, et al.** s.l. : Springer-Verlag London Limited, October 18, 2006, Engineering with Computers, Vol. 22, pp. 325-247.

18. *Computational biology - Modeling of primary blast effects on the central nervous system.* **Moore, David F., et al.** s.l. : Elsevier Inc., 2009, NeuroImage, Vol. 47, pp. T10-T20.

19. *In Silico Investigation fo Intracranail Blast Mitigation with Relevance to Military Traumatic Brain Injury.* **Nyein, Michelle K., et al.** 48, November 30, 2010, Proceedings of the National Academy of Sciences of the United States of America, Vol. 107, pp. 20703-20708.

20. *Skull Flexure from Blast Waves: A Mechanism for Brain Injury with Implications for Helmet Design.* **Moss, William C., King, Michael J. and Blackman, Eric G.** s.l. : The American Physical Society, 2009, Physical Review Letters, Vol. 103, pp. 108702-1 - 108702-4.

21. *Simulation of Blast-Induced Early-Time Intracranial Wave Physics leading to Traumatic Brain Injury.* **Taylor, Paul A. and Ford, Corey C.** s.l. : ASME, June 2009, Journal of Biomechanical Engineering, Vol. 131, pp. 061007-1 - 061007-11.

22. *Explosive Blast Neurotrauma.* **Ling, Geoffrey, et al.** s.l. : Mary An Liebert, Inc., June 2009, Journal of Neurotrauma, Vol. 26, pp. 815-825.

23. **Smith, P. D. and Hetherington, J. G.** *Blast and Ballistic Loading of Structures.* Oxford : Butterworth-Heinemann Ltd, 1994.

24. **Zukas, Jonas A. and Walters, William.** *Explosive Effects and Applications.* s.l. : Springer-Verlag, 1998.

25. **Baker, W. E.** *Explosions in Air.* s.l. : University of Texas Press, 1973.

26. **Drumheller, D. S.** *Introduction to Wave Propagation in Nonlinear Fluids and Solids.* Cambridge : Cambridge University Press, 1998.

27. **Kambouchev, Nayden.** *Analysis of Blast Mitigation Strategies Exploiting Fluid-Structure Interaction.* Aeronautics and Astronautics, Massachusetts Institute of Technology. Cambridge, MA : s.n., 2007. Ph.D. Thesis.

28. *An Analytical Solution for Blast Waves.* **Bach, G. G. and Lee, H. S.** 2, February 1970, AIAA Journal, Vol. 8, pp. 271-275.

29. **Sedov, L. I.** *Similarity and Dimensional Methods in Mechanics.* New York : Academic Press, 1959.

30. **von Neumann, J.** The Point Source Solution. *Collected Works of J. von Neumann.* Oxford : Pergamon Press, 1963, Vol. VI, p. 176.

31. *The Formation of a Blast Wave by Very Intense Explosion, I, Theoretical Discussion.* **Taylor, G. I.** 1950. Proceedings of the Royal Society (London), Series A. Vol. 201, pp. 159-174.

32. *Numerical simulation of the fluid-structure interaction between air blast waves and free-standing plates.* **Kambouchev, Nayden, Noels, Ludovic and Radovitzky, Raul.** s.l. : Elsevier Ltd., 2007, Computers and Structures, Vol. 85, pp. 923-931.

33. **Sakurai, A.** Blast Wave Theory. [ed.] M. Holt. *Modern Developments in Fluid Dynamics.* New York : Academic Press, 1965, pp. 309-375.

34. *Higher-Order Perturbation Solutions for Blast Waves.* **Bach, G. G. and Lee, J. H.** 4, 1968, AIAA Journal, Vol. 7, pp. 742-744.

35. **Taylor, G.** The Pressure and Impulse of Submarine Explosion Waves on Plates. [ed.] G. Batchelor. *The Scientific Papers of Sir Geoffrey Ingram Taylor. Aerodynamics and the Mechanics of Projectiles and Explosions.* s.l. : Cambridge University Press, 1963, Vol. III, pp. 287-303.

36. *Nonlinear Compressibility Effects in Fluid-Structure Interaction and Their Implications on the Air-Blast Loading of Structures.* **Kambouchev, N., Neols, L. and Radovitzky, R.** s.l. : The American Institute of Physics, 2006, Journal of Applied Physics, Vol. 100, pp. 063519-1 - 063519-11.

37. *Fluid-Structure Interaction Effects in the Dynamic Response of Free-Standing Plates to Uniform Shock Loading.* **Kambouchev, Nayden, Radovitzky, Raul and Noels, Ludovic.** s.l. : ASME, September 2007, Journal of Applied Mechanics, Vol. 74, pp. 1042-1045.

38. *A Method for the Numerical Computation of Hydrodynamic Shocks.* **von Neumann, J. and Richtmyer, R.** 1950, Journal of Applied Physics, Vol. 21, pp. 232-237.

39. **Gibson, Lorna J. and Ashby, Michael F.** *Cellular Solids - Structure and Properties.* Second Edition. Cambridge : Cambridge Univeristy Press, 1999.

40. *Shock Wave Interaction with Cellular Materials Part I: Analytical Investigation and Governing Equations.* **Mazor, G., Ben-Dor, G. and Sorek, S.** s.l. : Springer-Verlag, 1994, Shock Waves, Vol. 3, pp. 159-165.

41. *Gas Dynamic and Physical Behavior of Compressible Porous Foams Struck By Wak Shock Waves.* **Skews, B. W., Atkins, M. D. and Seitz, M. W.** [ed.] K. Takayama. New York : Springer-Verlag, 1992. Proceedings of the 18th International Symposium on Shock Waves. pp. 511-516.

42. *Gvozdeva, L. G.; Faresov, Yu. M.; Fokeev, V. P.* **Materials, Interaction of Air Shock Waves with Porous Compressible.** 3, s.l. : Springer-Verlag, 1985, Journal of Applied Mechanics and Technical Physics, Vol. 26, pp. 401-405.

43. *Shock Wave Interaction With Cellular Materials Part II: Open Cell Foams; Experimental and Numerical Results.* **Ben-Dor, G., et al.** s.l. : Springer-Verlag, 1994, Shock Waves, Vol. 3, pp. 167-179.

44. *Attenuation of Enhancement - A One-Dimensional Analysis on Shock Transmission in the Solid Phase of a Cellular Material.* **Li, Q. M. and Meng, H.** s.l. : Elsevier Science Ltd., 2002, International Journal of Impact Engineering, Vol. 27, pp. 1049-1065.

45. *Close-Range Blast Loading of Aluminum Foam Panels.* **Hanssen, A. G., L., Enstock and Langseth, M.** s.l. : Elsevier Science Ltd;, 2002, International Journal of Impact Engineering, Vol. 27, pp. 593-618.

46. *Numerical Investigation of the Propagation of Shock Waves in Rigid Proous Materials: Development of the Computer Code and Comparison With Experimental Results.* **Levy, A., Ben-Dor, G. and Sorek, S.** s.l. : Cambridge University Press, 1996, Journal of Fluid Mechanics, Vol. 324, pp. 163-179.

47. *Preliminary Assessment of Sandwich Plates Subject to Blast Loads.* **Xue, Zhenyu and Hutchinson, John W.** s.l. : Elsevier Ltd., 2003, International Journal of Mechanical Sciences, Vol. 45, pp. 687-705.

48. *Dynamic Response of a Clamped Circular Sandwich Plate Subject to Shock Loading.* **Qiu, X., Deshpande, V. S. and Fleck, N. A.** s.l. : ASME, September 2004, Journal of Applied Mechanics, Vol. 71, pp. 637-645.

49. *An Experimental Investigation of Shock Wave Propagation in Periodically Layered Composites.* **Zhuang, Shiming, Ravichandran, Guruswami and Grady, Dennis E.** s.l. : Elsevier Science Ltd., 2003, Journal of the Mechanics and Physics of Solids, Vol. 51, pp. 245-265.

50. *Numerical Simulation of Nonlinear Elastic Wave Propagation in Piecewise Homogeneous Media.* **Berezovski, Arkadi, Berezovski, Mihhail and Engelbrecht, Juri.** s.l. : Elsevier Science Ltd., 2006, Materials Science and Engineering A, Vol. 418, pp. 364-369.

51. *Uniaxial Crushing of Sandwich Plates Under Air Blast: Influence of Mass Distribution.* **Main, Joseph A. and Gazonas, George A.** s.l. : Elsevier Ltd., 2008, International Journal of Solids and Structures, Vol. 45, pp. 2297-2321.

52. *Behaviour of Sandwich Panels Subject to Intense Air Blasts - Part 2: Numerical Simulation.* **Karagiozova, D., Nurick, G. N. and Langdon, G. S.** s.l. : Elsevier Ltd., 2009, Composite Structures, Vol. 91, pp. 442-450.

53. **Chong, W. K., et al.** *Computational Study of Water Mitigation Effects On An Explosion Inside A Vented Tunnel System.* Institute of High Performance Computing, National University of Singapore. Singapore : s.n., 1998.

54. *Reduction of Explosion Damage Using Sand or Water Layer.* **Homae, T., et al.** [ed.] M. Elert, et al. s.l. : American Institute of Physics, 2007, Shock Compression of Condensed Matter, pp. 1289-1292.

55. **Schwer, D. and Kailasanath, K.** *Blast Mitigation by Water Mist (3) Mitigation of Confined and Unconfined Blasts.* Naval Research Laboratory. Washington, D.C. : s.n., 2006. Memorandum Report. NRL/MR/6410--06-8976.

56. *Energy Absorption and Recovery in Tapered Granular Chains: Small Chains and Low Tapering.* **Pfannes, Jan, et al.** s.l. : Materials Research Society, 2003. Materials Research Society Symposium Proceedings. Vol. 759, pp. MM4.5.1 - MM4.5.8.

57. *Shock (Blast) Mitigation by "Soft" Condensed Matter.* **Nesterenko, Vitali F.** Pittsburgh, PA : Materials Research Society, 2003. Materials Research Society Symposium Proceedings. Vol. 759, pp. MM4.3.1 - MM4.3.12.

58. *Experimental and Numerical Study of Free-Field Blast Mitigation.* **Allen, R. M., et al.** [ed.] M. D. Furnish, Y. M. Gupta and J. W. Forbes. s.l. : American Institute of Physics, 2003, Shock Compression of Condensed matter, pp. 823-826.

59. **Morgan, G. E.** *Energy ABsorbing and Sizing Means for Helmets. 3609764* USA, October 1971.

60. **Holt, M. and Tomczak, W. F.** *Protective Gear with Hydraulic Liner. 3849801* USA, November 1974.

61. **Villari, F. K., Steigerwald, C. J. and Rappleyea, F. A.** *Protective Helmet. 3994021* USA, November 1976.

62. **Gooding, E. R.** *Energy-Absorbing Insert for Protective Headgear. 4375108* USA, March 1983.

63. **Hosaka, D. K.** *Helmet and Fluid Reservoir Apparatus. 5148950* USA, September 1992.

64. **Calonge, R.** *Resistant Helmet Assembly. 5815846* USA, October 1998.

65. **Mendoze, I. D.** *Safety Helmet. 6560787 B2* USA, May 2003.

66. *Optimisation of Energy Absorbing Liner for Equestrian Helmets. Part I: Layered Foam Liner.* **Forero Reudo, M. A., Cui, L. and Gilchrist, M. D.** s.l. : Elsevier Ltd., 2009, Materials and Design, Vol. 30, pp. 3405-3413.

67. *Optimisation of Energy Absorbing Liner for Equestrian Helmets. Part II: Functionally Graded Foam Liner.* **Cui, L., Forero Rueda, M. A. and Gilchrist, M. D.** s.l. : Elsevier Ltd., 2009, Materials and Design, Vol. 30, pp. 3414-3419.

68. *Evaluation of Head Response to Ballistic Helmet Impacts Using the Finite Element Method.* **Aare, Magnus and Kleiven, Svein.** s.l. : Elsevier Ltd., 2007, International Journal of Impact Engineering, Vol. 34, pp. 596-608.

69. **Young, Laurence, Chan, Nicholas and Ruchelsman, Jason.** *Fluid Safety Liner. US 2009/0265839 A1* USA, October 29, 2009. Patent Application Publication.

70. **Claire, A. and Vue, B.** *Helmet Liners with Fluid Filled Channels.* Department of Aeronautics and Astronautics, Massachusetts INstitute of Technology. Cambridge, MA : s.n., 2007. MIT Course 16.621 Final Report.

71. **Stewart, Douglas.** *Protective Helmet Liner Incorporating Fluid Channels.* School of Electrical, Electronic, and Mechanical Engineering, University College Dublin. Dublin, Ireland : s.n., 2008. Master Thesis.

72. **Alley, Matthew David.** *Explosive Blast Loading Experiments for TBI Scenarios: Characterization and Mitigation.* Mechanical Engineering, Purdue University. West Lafayette, IN : s.n., 2009. Master Thesis.

73. **Christou, George Alexander.** *Development of a Helmet Liner for Protection Against Blast Induced Trauma.* Aeronautics and Astronautics, Massachusetts Instittute of Technology. Cambridge, MA : s.n., 2010. Master Thesis.

74. ABAQUS v6.10 Documentation.

75. **Johnson, T. P. M.** *High Strain Rate Mechanical Characterization of Trabecular Bone Utilizing the Split-Hopkinson Pressure Bar Technique.* Department of Mechical Engineering, Massachusetts Institute of Technology. Cambridge, MA : s.n., 2005. Master's Thesis.

76. **Media Blast & Abrasive, Inc.** Glass Bead Conversion Table. [Online] 2011. [Cited: Jan 17, 2011.] http://www.mediablast.com/glass-bead-conversions.php.

77. *Compression Model for Cohesionless Soils.* **Pestana, J. M. and Whittle, A. J.** 4, 1995, Geotechnique, Vol. 45, pp. 611-631.

78. **Humrickhouse, Paul W.** *Hyperelastic Models for Granular Materials.* Fusion Technology Institute, University of Wisconsin - Madison. Madison, WI : s.n., 2009. Ph. D. Thesis.

79. **Lambe, T. William and Whitman, Robert V.** *Soil Mechanics, SI Version.* s.l. : John WIley & Sons, Inc., 1979. ISBN 0-471-02491-0.

80. Cohesionless Soil. [Online] [Cited: Jan 18, 2011.] http://bsi-web.ce.ufl.edu/downloads/files/MultiPier_Soil_Table.pdf.

81. *The Performance of Pressure Vessel Using Concentric Double Cylindrical High Explosive.* **Hamada, Toru, Nakamura, Yuichi and Itoh, Shigeru.** s.l. : American Society of Mechanical Engineers, November 2004, Journal of Pressure Vessel Technology, Vol. 126, pp. 409-413.

82. Comparing Two Materials. *MakeItFrom.com.* [Online] http://www.makeitfrom.com/compare/?left=Acrylic&right=Soda_Lime_Glass.